UNIVERSITY OF TRENTO - Italy
Department of Civil, Environmental and Mechanical Engineering

Doctoral School in Materials Science and Engineering – XXVII cycle

Advanced Characterization of Nanocrystalline Materials by Synchrotron Radiation X-ray Diffraction

Luca Rebuffi

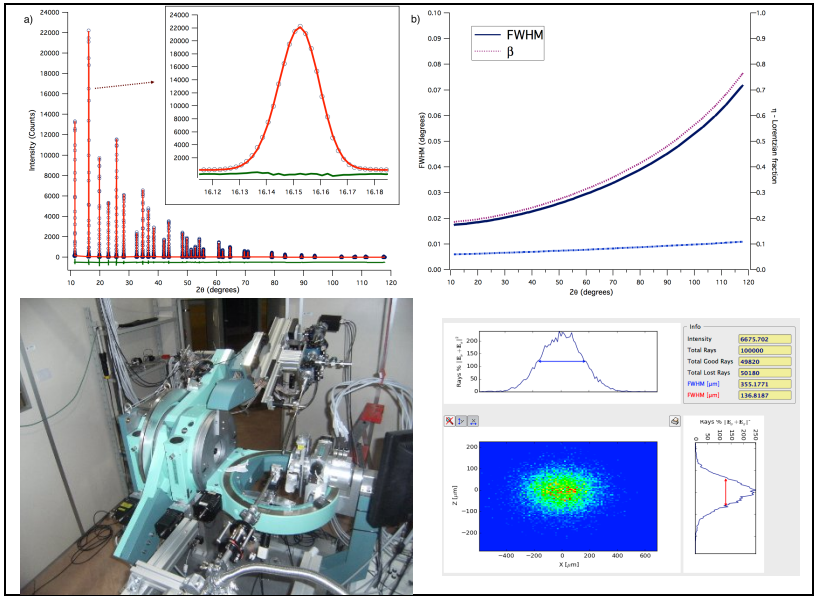

April 2015

Advanced Characterization of Nanocrystalline Materials By Synchrotron Radiation X-ray Diffraction

Luca Rebuffi

Approved by:

Prof. Paolo Scardi, Advisor
Department of Civil, Environmental and Mechanical Engineering
University of Trento, Italy

Dr. Edoardo Busetto
Mechanical, Vacuum and Optical Engineering group
Elettra-Sincrotrone Trieste, Italy

Ph.D. Commission:

Prof. Alberto Molinari
Department of Industrial Engineering
University of Trento, Italy

Prof. José Manuel Torralba Castelló
IMDEA Materials Institute
Universidad Carlos III de Madrid, Spain

Dr. Yves Leterrier
Laboratoire de Technologie des Composites et Polymères
Ecole Polytechnique Fédérale de Lausanne, Switzerland

Dr. Antonietta Guagliardi
Institute of Crystallography
National Research Council, IC-CNR and To.Sca.Lab, Italy

University of Trento, Faculty of Engineering

Department of Civil, Environmental and Mechanical Engineering

April 2015

University of Trento - Department of
Civil, Environmental and Mechanical Engineering

Doctoral Thesis

Luca Rebuffi - 2015
Published in Trento (Italy) – by University of Trento

“Γνώθι σ’ αυτόν.

“Know yourself.

Σ’ αυτόν ίσθι.

Be yourself.

Σοφοίς χρω.

Consult the wise.

Ακούσας νόει.

Understand what you have heard.

Γνώθι μαθών.

Know what you have learned.

Φθόνει μηδενί.

Be jealous of no one.

Νεώτερον δίδασκε.”

Teach a youngster.”

Ancient Delphic maxims.

Abstract

Synchrotron Radiation (SR) is one of the most powerful and versatile tools in the study nanomaterials, supporting a variety of analytical techniques. Among the possible spectroscopies, X-ray Diffraction (XRD) is especially suited to investigate materials at the nanoscale. However, to benefit of the full potential of SR XRD, a complete control of the diffracted signal is necessary, including the optics and general set-up of the beamline, which contribute to the Instrumental Profile Function (IPF).

Exploring and characterizing the optical components for powder diffraction beamlines is the bottom line of the present Thesis, with the purpose of properly calibrating and adjusting all components in order to deliver the beam under the best possible conditions. Main benefits of this novel approach appear in the study of relatively large crystalline domains, toward the upper limit of the nanoscale (≈ hundreds of nm), a critical range between nano- and micro-crystalline, where the IPF is the main feature appearing in the experimental data.

Thanks to this investigation it was possible to develop solutions and tools to improve knowledge and enhance the capability of handling the IPF along the life-cycle of a powder diffraction experiment. This result was achieved by studying and characterizing a new possible reference material for Line Profile Analysis (of size and strain effects), and by developing an original simulation/modelling software, based on ray-tracing algorithms, capable to predict and analyse the instrumental behaviour of a beamline.

As such the results of this work, and in a more general sense the emerging paradigm, will be of interest to many other beamlines currently employed for X-ray spectroscopies.

Table of contents

Chapter 1

Introduction

X-ray Diffraction (XRD) Line Profile Analysis (LPA) is a well-known technique for the study of materials microstructure [1][2]. Peak profiles in the diffraction pattern are modified in shape, intensity and position by microstructural effects, like the shape and size distribution of the crystalline domains (aka crystallites), and/or lattice distortions present in the system (microstrain), and, in general, disorder present in the system. Together with these physical sources, the observed profile contains the instrumental contribution, which is a combined effect of photon source energy, spatial and angular divergence distributions of the photon beam, optical setup and quality of its elements.

The diffraction line profile observed experimentally (h) can be conceived as a convolution of the individual profiles of the different sources of instrumental broadening (g) and structural line broadening (f), such as crystallite size and microstrain [3][4]:

$$h(\varepsilon) = \int_{-\infty}^{+\infty} g(\eta) f(\varepsilon - \eta) d\eta \tag{1}$$

When dealing with nanostructured material, crystalline domain size produces the dominant effect on profiles. This can be treated according to the Scherrer's formula [5][6], correlating the measured integral breath $\beta(2\theta)$ with the volume-weighted mean crystallite size $\langle D \rangle_V$ and the incoming photon beam wavelength λ:

$$\beta(2\theta) = \frac{K_\beta \lambda}{\langle D \rangle_V \cos\theta} \tag{2}$$

Just considering the inverse proportionality occurring between the observed quantity and the average crystallite size, it comes clear how the error on the crystalline domain size diverges for small values of integral breadth, i.e. when instrumental effects are the main feature. Therefore, the LPA capability of determining the characteristics of nanostructured materials, mostly with "large" (several hundreds of nanometres) crystalline domains, is strongly affected by the shape and by the stability of the Instrumental Profile Function (IPF).

While Chapter 2 contains a full instrumental characterization of a synchrotron radiation beamline, MCX at the Italian synchrotron Elettra-Sincrotrone Trieste, examples of a nanostructured material with large crystalline domains are described in Chapter 3, in studies on the microstructure of Cu_2ZnSnS_4 (CZTS aka Kesterite), a solar absorbing semiconducting material and of EVAVIRENZ, an anti-HIV drug, both made at the MCX beamline. Samples with $\langle D \rangle_V \approx 250$ nm showed detectable effects on the shape of the peaks and allowed the calculation of the crystalline domain size distribution function, by carefully measuring and keeping under control the IPF of the beamline.

Synchrotron Radiation (SR) seems the most appropriate choice to collect high quality diffraction data, thanks to the high beam brilliance, energy selectivity, and focusing conditions. But even a simple powder geometry can be affected by considerable aberrations [7][8], and the IPF needs to be "well-behaving", i.e., easily represented in convenient form for data analysis.

This is particularly significant when dealing with the Debye scattering equation (DSE), that makes no assumptions on crystalline structure and lattice defects, as it is based only on correlations between all possible pairs of atoms [9][10]. The DSE result is quite rigorous and comparison with experimental data asks for diffraction patterns with small instrumental effects, in particular in terms of relative intensities and

position of the peaks, i.e. small and well-parameterized optical aberrations and negligible absorption effects.

Several mathematical description of instrumental effects are available in literature, in particular describing the optical origin of the diffracted beam divergence [11][12], and the optical aberrations effects [13][14][15][16], used by methods for data analysis like Whole Powder Pattern Modelling (WPPM) [17] to build a mathematical parametric representation of the IPF, available for calibration and fitting procedures.

In any case, the optical nature of the instrumental contribution to the diffraction pattern suggests a ray-tracing simulation approach for its description, prediction and analysis [18][19].

In Chapter 5 it is shown in detail how SHADOW [20][21][22][23], a well-known and widely used software for the simulation of realistic effects on the beam transport through optical elements, is used as the basis for a ray-tracing simulation of a powder diffraction capillary sample (Debye-Scherrer geometry).

As detailed in Chapter 2, the real calculation of the IPF is obtained by analysing the diffraction pattern of a Standard Reference Material (SRM) like LaB_6 (NIST SRM 660 [24][25]), therefore the simulated instrumental profile is obtained by ray-tracing the interaction of the photons with a capillary filled by such a SRM, generating a diffracted photon beam and prosecuting the ray-tracing onto the optical elements lying on the path from sample to detector. Thanks to this approach and to the capabilities of SHADOW, it was possible to analyse selectively the instrumental profile, contribution by contribution (like photon beam, or optical elements properties), and identify the most critical features.

Another important methodological remark is that, despite the considerable interest in LPA, there are no established procedures and no reference materials to compare results, validate methods and

experimental protocols. Nowadays SRMs give no support to the study of line broadening effects caused by the microstructure of materials.

Chapter 4 contains the study of a proposed new reference material, an Iron-Molybdenum alloy, extensively deformed by high energy milling, so to refine the bcc iron domain size to nanometer scale (≈10 nm) and introduce a strong inhomogeneous strain, with the two effects producing a comparable amount of line broadening.

Chapter 2

Optical Characterization of a Powder Diffraction Beamline

Part of this chapter has been published in:

Luca Rebuffi, Jasper R. Plaisier, Mahmoud Abdellatief, Andrea Lausi, Paolo Scardi,

"**MCX: a synchrotron radiation beamline for X-ray diffraction Line Profile Analysis**",
Z. Anorg. Allg. Chem., 640 (2014), 3100-3106, doi: 10.1002/zaac.201400163.

Abstract

The potential of modern methods for X-ray diffraction Line Profile Analysis can be fully exploited with data collected at synchrotron radiation beamlines, provided that optics and experimental set-up are suitably designed and characterized. The Material Characterization by X-ray Diffraction beamline, MCX, at Elettra-Sincrotrone Trieste, may operate with a set-up optimally arranged to study nanostructured materials, investigating details of crystalline domain size and shape, lattice defects and local atomic displacement of static and dynamic nature.

2.1 Introduction

Modern methods for XRD LPA [1][2] require quality data to obtain detailed and reliable information. Therefore, SR, with the high beam brilliance, energy selectivity and focusing conditions, now routinely available at most facilities, seems the most appropriate choice to collect high quality powder diffraction data. However, for this to be true, optics and experimental set-up should be suitably designed and used. MCX, the Material Characterization by X-ray Diffraction beamline at Elettra-Sincrotrone Trieste [26], currently operates in the energy range from 4 to 21 keV, and hosts optics and instrumentation specific for LPA of nanostructured materials. It allows investigating details of crystalline domain size and shape, lattice defects and local atomic displacement of static and dynamic nature.

Like most modern SR powder diffraction beamlines, MCX adopts the Debye-Scherrer geometry, with a standard glass capillary sample holder. MCX design, however, is sufficiently flexible to host a flat-plate geometry too, which may be a convenient choice for the absence of signal of the capillary and, in general, to analyse bulk samples, thin films, coatings and surfaces.

As with any experimental set-up, even a simple powder geometry can be affected by considerable aberrations [7][8], which can be a serious limitation to a correct assessment of the instrument contribution to the observed line profiles. In particular, the IPF needs to be "well-behaving", i.e., easily represented in convenient form for data analysis.

The present work shows how to get the most out of a powder diffraction beamline to fully exploit LPA, pushing resolution to the limits. Main features of MCX are briefly discussed with reference to LPA applications: specific attention is paid to the IPF, which is carefully optimized and determined in a convenient parametric form.

2.2 The MCX Beamline

The Material Characterization by X-ray Diffraction beamline at Elettra-Sincrotrone Trieste, supports a wide range of diffraction experiments from powders, bulk polycrystalline, thin films and coating materials. Open to users since 2009, over the past years MCX hosted a variety of experiments in different fields, as diverse as structure refinement [27], residual stress analysis [28], pair distribution functions (PDF) of glasses and amorphous compounds [29] and temperature dependent studies [30][31].

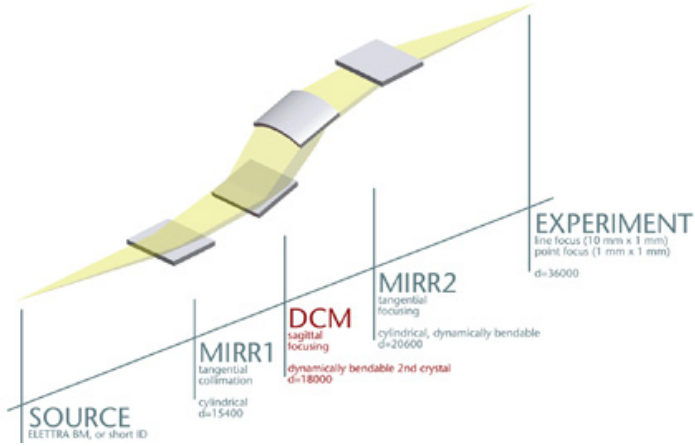

Figure 1: Optical layout of the MCX beamline

Flexibility, which is a keyword of MCX, is provided by the optics of the line, consisting of two mirrors and a monochromator (see Figure 1): a first Pt-coated cylindrical mirror collimates the beam on the horizontally focusing Si(111) double crystal monochromator with the second crystal mounted on a European Synchrotron Radiation Facility (ESRF) model sagittal bender [32]. The second – vertical focusing – Pt-coated mirror is flat and bendable, with a radius adjustable from 6 km to flat. The overall optical layout works in a strictly 1:1 configuration, with the

monochromator at 18 m from the source and the focus, and the mirrors positioned symmetrically around it.

The fixed exit – double crystal monochromator (DCM) consists of two Si crystals cut along the [111] direction, which can be precisely positioned and oriented in the X-ray beam. Two successive Bragg reflections with a theoretical inherent energy resolution of 0.014% (given by the Darwin angular width of the Si (111) perfect crystal reflection) direct photons of the desired energy parallel to the incoming beam direction, but offset upward (out of the direct Bremsstrahlung beam). The crystals are placed on two independent rotation stages, and the second crystal can be translated along the beam direction in order to keep the exit height fixed. The optics of the beamline produce X-rays with an energy between 4 and 21 keV. The beam spot at the experiment can be varied from point focus (0.3x0.3 mm^2), to line focus (5x1 mm^2).

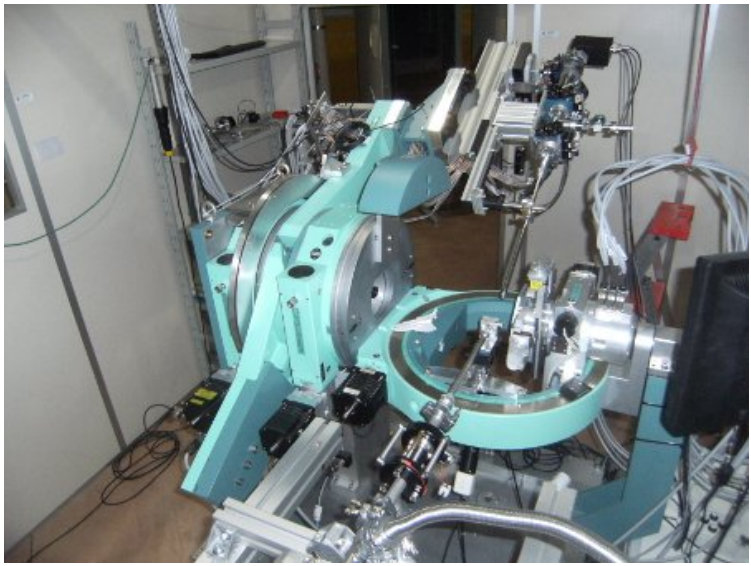

Figure 2: 4-circle Huber diffractometer at MCX

Two alternative setups are used to conduct the diffraction experiments. First one is based on a 4-circle Huber diffractometer (see Figure 2), equipped with a high-count rate fast scintillator detector. Either a set of slits or an analyser crystal (Si(111)) is positioned before the detector to achieve a high angular resolution. Both Bragg-Brentano (flat plate) and Debye-Scherrer (capillary) geometry may be employed in the experiments. The sample area is large, thus allowing space for hosting different environmental chambers. As part of the standard equipment, capillaries can be cooled or heated in the 100 – 1300K range.

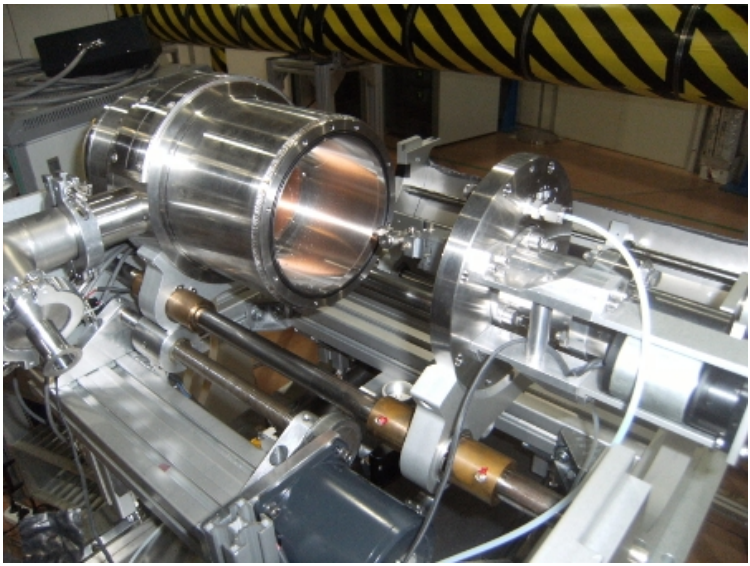

Figure 3: Furnace at MCX

An alternative experimental setup based on a furnace has been developed [33] to provide an atmosphere and temperature controlled environment for powders in capillaries and a temperature controlled environment for thin-film samples (see Figure 3). The whole powder pattern is recorded by a translating image plate, as a fast data collection

system to follow phase transformations and chemical reactions. The furnace in its current setup allows heating up to 1300K.

2.3 DCM: Thermo-Mechanical characterization

In order to understand the relevance of the DCM in shaping the instrumental profile, it is important to focalize the attention on possible aberration sources.

2.3.1 DCM: first crystal

The first crystal is a ultra-high quality flat single-crystal, with a measured Darwin width (full width at half-maximum of the total reflective profile, or diffraction profile, of the monochromator crystal [34][35]) close to the ideal one.

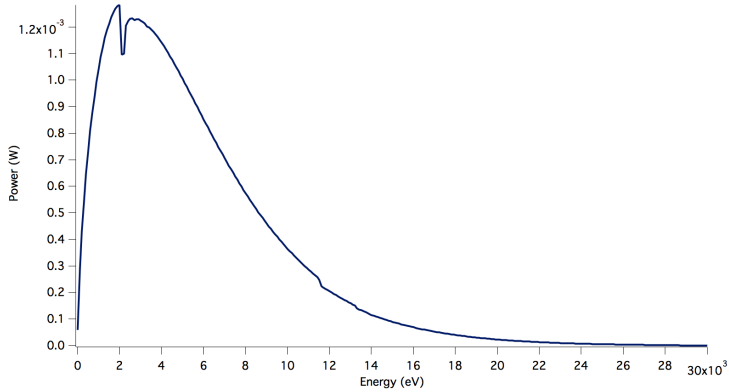

Figure 4: Incident power distribution on the MCX DCM first crystal. The calculation takes into account the angular acceptance of the beam shaping slits and the reflectivity profile of the first collimating mirror. The integral of this distribution represent the estimated total power hitting the crystal.

This crystal is hit by the "white" beam, collimated by the first mirror, and thermal energy absorption could be a possible source of deformation of

the crystal planes (heat bump), leading to unwanted effects of angular spreading of the beam, bigger bandwidth and flux reduction [36][37].
By the way, the case of MCX is not to be considered critical, because the total power incident on the crystal, calculated with the SPECTRA source simulation tool [38][39], is around 10 W in the worst situation (2 GeV storage ring energy and 310 mA of electron current), easily dissipated by the cooling system (see Figure 4).

2.3.2 DCM: second crystal

The second crystal is mounted (soldered) on the ESRF model sagittal bender [32][40], a widely used flexural hinge bender made of stainless steel, shown in Figure 5, providing a near-cylindrical surface shape. Two motors acting in opposite direction with identical force, pushing on the crystal holders make the bending mechanism.

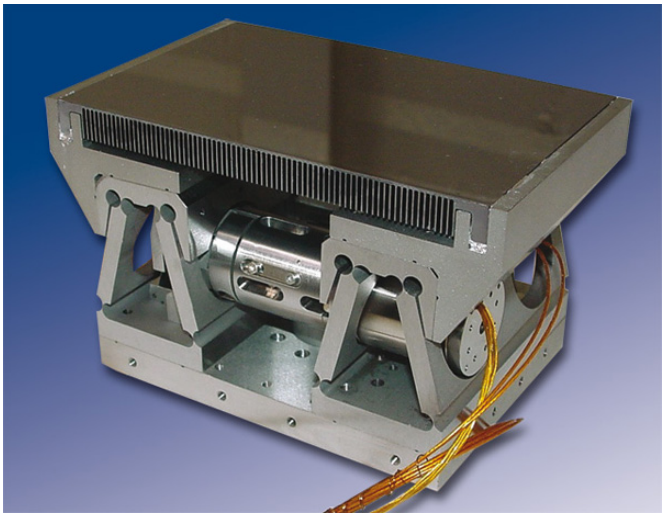

Figure 5: Flexural hinge bender, with a bendable silicon crystal mounted and soldered. Anticlastic curvature ribs are visible on the back of the crystal. The soldering material appears as a white layer between silicon and the stainless steel holders.

The most important aberration taken into account even in the design phase of such an optical element is the drastic correction of the anticlastic curvature (see Figure 6). This is made by cutting ribs in the direction transverse to the principal radius [40], as shown in Figure 5. This aberration is important because it acts in the vertical plane, i.e. the plane where the further diffraction profile is collected, modifying the divergence profile of an ideally collimated beam and/or "turning off" parts of the beam, where the Bragg planes are too misaligned (deformed) respect to the ideal orientation.

Together with this mechanical effect, a possible twist effect comes from the soldering process between the silicon crystal and the stainless steel holders and from the bending mechanism itself (as visible in Figure 5, there are 2 independent motors pushing each holder separately). This effect is kept under control by a careful soldering procedure [41].

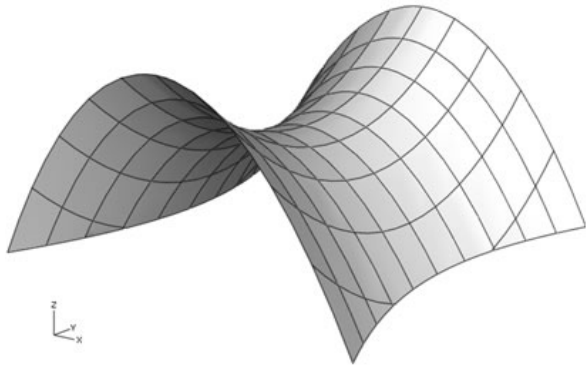

Figure 6: Anticlastic Curvature

The global effect of these aberration sources can be visible by a direct measurement of the rocking curve of the crystal, in sagittally focusing condition (on the detector). This measurement is obtained by a stepped scan of the diffracted signal rotating the crystal around its θ axis, to

which the Bragg angle is referred. This operation gives the convolution of the diffraction profiles of the two crystal [35].

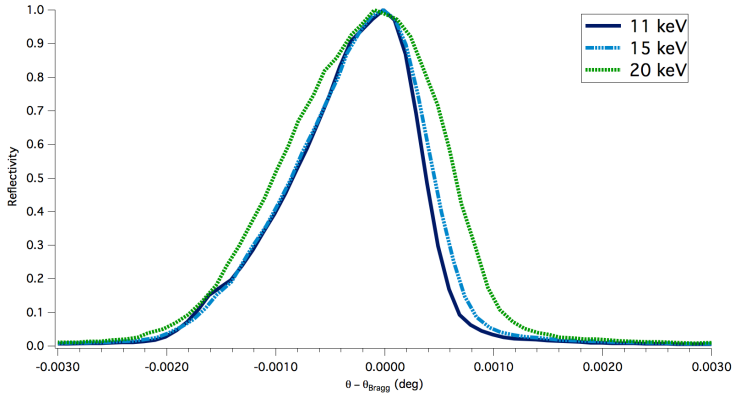

Figure 7: Comparison between the experimental diffraction profile of the second crystal, in focusing condition, at three different photon beam energies (selected by the first crystal): 11, 15, 20 keV

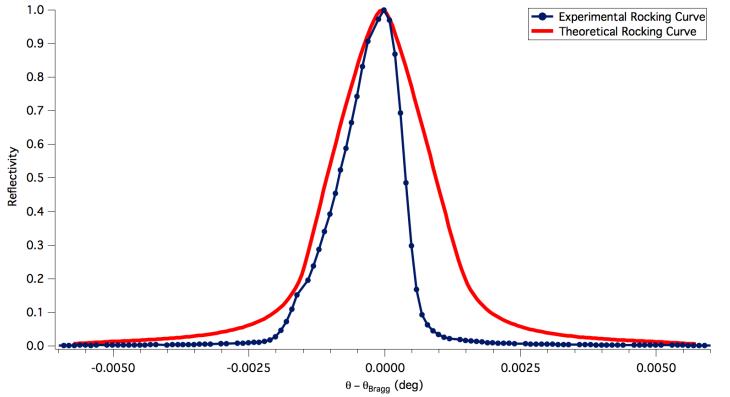

Figure 8: Comparison between the experimental rocking curve of the second crystal, in focusing condition, and a theoretical one at 11 keV.

Figure 7 shows the asymmetry of the rocking curve of the second crystal progressively decreasing with diminishing of the curvature radius (inversely proportional to the photon energy), suggesting that

apparently the increasing bending strain gives stability in shape of the crystal.

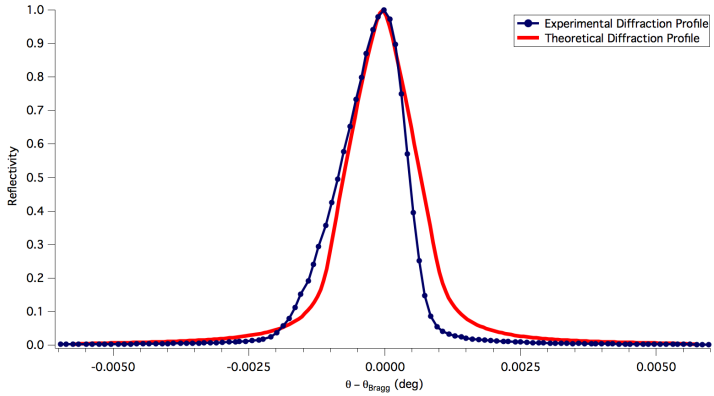

Figure 9: Comparison between the experimental rocking curve of the second crystal, in focusing condition, and a theoretical one at 15 keV.

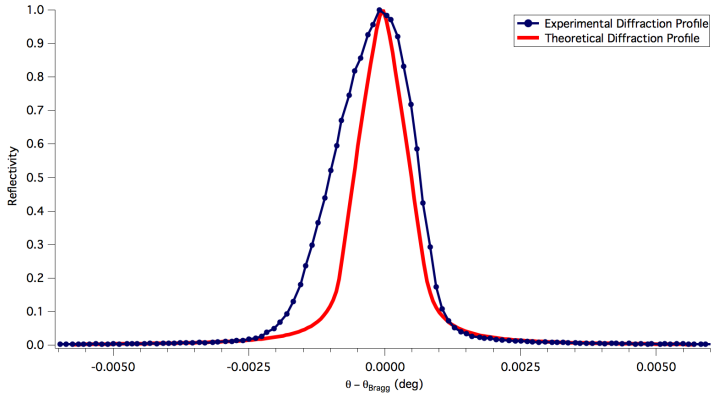

Figure 10: Comparison between the experimental rocking curve of the second crystal, in focusing condition, and a theoretical one at 20 keV.

In Figure 8 the comparison between the experimental rocking curve at 11 keV and the theoretical one is shown, while in Figure 9 and in Figure 10 the same comparison is done at 15 keV and 20 keV, respectively.

The theoretical curve is obtained with the XCRYSTAL simulation tool of the diffraction profile (reflectivity) of perfect crystals, contained in the XOP kit [42], and calculating its autoconvolution, i.e. considering the second crystal as a flat and perfect element.

In particular, as visible in Figure 11 and Figure 12, by assuming the first DCM crystal as perfect (a reasonable approximation, as discussed in paragraph 2.3.1) we can reconstruct a possible diffraction profile of the second crystal, until a rocking curve similar to the experimental one is obtained by convolution with the first crystal diffraction profile. The result is a diffraction profile not only asymmetric but with a smaller width than the theoretical one, with a direct consequence that the beam energy bandwidth at the sample will be smaller than the predicted one.

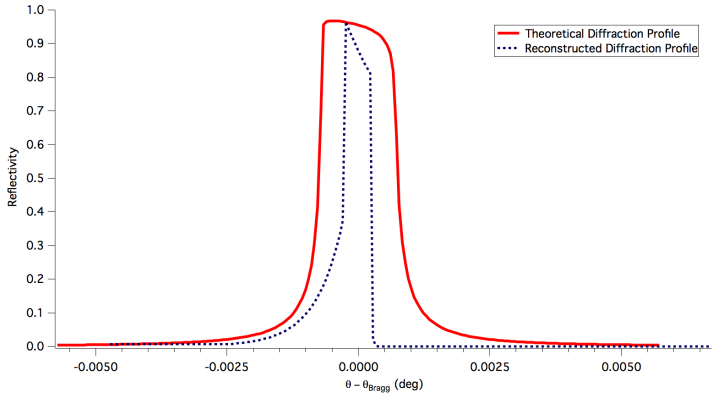

Figure 11: Comparison between theoretical diffraction profile of the second crystal and a reconstructed one for the bended crystal in focusing condition, at 11 keV.

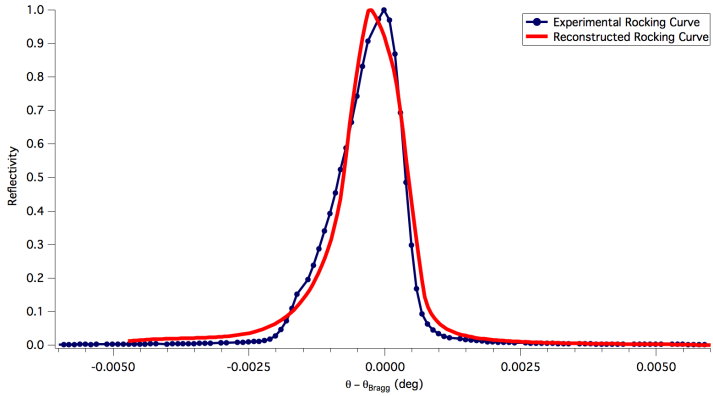

Figure 12: Comparison between the experimental rocking curve of the second crystal, in focusing condition, and the reconstructed one at 11 keV.

As visible in Figure 13 and Figure 14, at 15 keV this effect is smaller, giving a reconstructed bandwidth closer to the theoretical one, but again with an asymmetric diffraction profile, while at 20 keV the reconstructed diffraction profile is broader, but shows a less asymmetric shape, as visible in Figure 15 and in Figure 16.

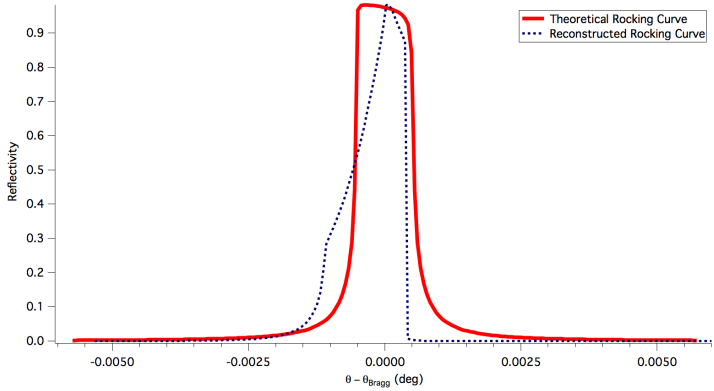

Figure 13: Comparison between theoretical diffraction profile of the second crystal and a reconstructed one for the bended crystal in focusing condition, at 15 keV.

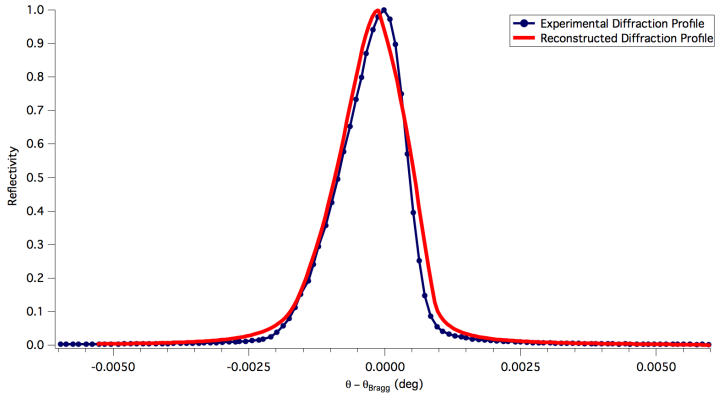

Figure 14: Comparison between the experimental rocking curve of the second crystal, in focusing condition, and the reconstructed one at 15 keV.

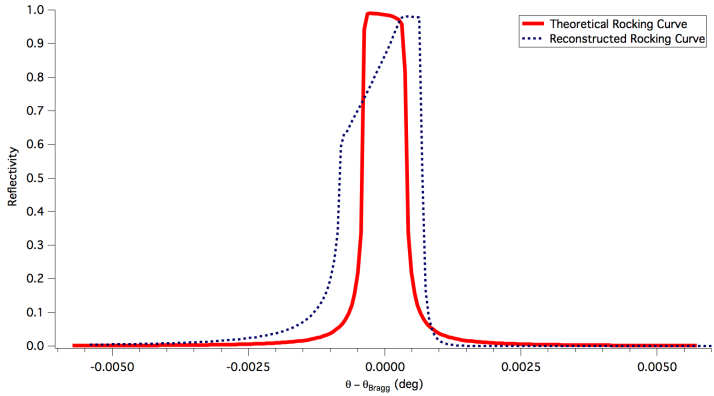

Figure 15: Comparison between theoretical diffraction profile of the second crystal and a reconstructed one for the bended crystal in focusing condition, at 20 keV.

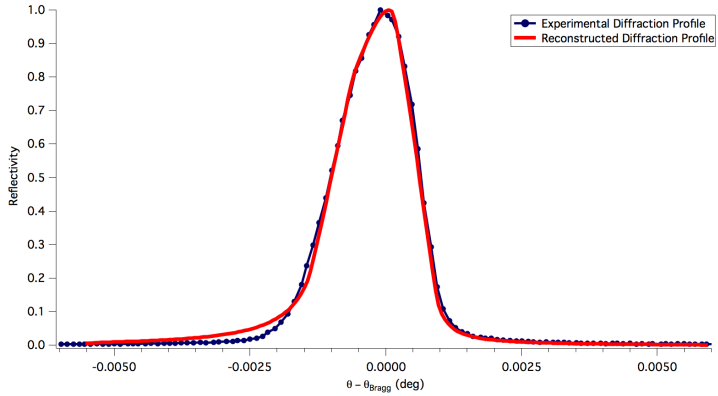

Figure 16: Comparison between the experimental rocking curve of the second crystal, in focusing condition, and the reconstructed one at 20 keV.

An important remark is that no significant effects on the diffraction profile are expected on a perfectly spherical sagittal bending, as visible from the computation made with the XOP XCRYSTAL tool for bent crystal [42][43], using a multilamellar model of the sagittally bent crystal (see Figure 17).

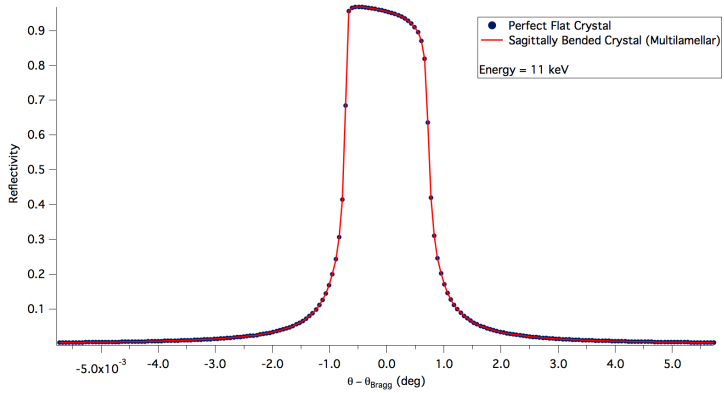

Figure 17: Comparison of the calculated diffraction profiles by the XCRYSTAL tool in XOP. Perfect flat crystal (circles), multilamellar sagittally bent crystal (straight line).

The main idea behind this method is to decompose the crystal (in the direction of beam penetration) in several layers of a suitable thickness. Each layer behaves as a perfect crystal, thus the diffracted and transmitted beams are calculated using the dynamical theory for plane crystals. The different layers are misaligned one with respect to the others in order to follow the cylindrical surface of the crystal plate (see Figure 18).

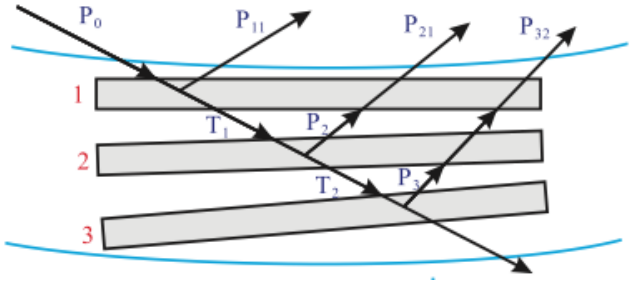

Figure 18: Crystal division in the Multilamellar model for a Bragg crystal with the respective transmitted and diffracted beams (courtesy of Dr. Manuel Sánchez del Río), in case of tangential bending.

This model works well, even if it does not take into account a possible deformation of the surface (and of the Bragg planes) coming from the bending mechanism.

For this reason every possible alteration on the angular divergence and energy distributions come out from the residual mechanical effects.

2.4 MCX Instrumental Profile Function

The Instrumental Profile Function of MCX was experimentally determined analysing the NIST SRM 660a LaB_6 line profile standard [24][25], using borosilicate glass capillaries (0.1 mm diameter) in the traditional Debye-Scherrer geometry.

Instrumental peak profiles were described by pseudo-Voigt curves, adopting a standard parameterization for the dependence of peak width and shape on the diffraction angle: Caglioti's equation is used for the FWHM, whereas a parabolic function describes peak shape, in this case the Lorentz profile fraction η (aka pseudo-Voigt mixing parameter) [11][44][45]:

$$FWHM(\theta) = \sqrt{W + V\tan\theta + U\tan^2\theta} \tag{3}$$

$$\eta(\theta) = a + b\theta + c\theta^2 \tag{4}$$

The apparent shift of the peak centroid, caused by aberrations along the beam path, were also parameterized using a $\tan\theta$ polynomial which closely follows Wilson's formulas [46]:

$$\Delta 2\theta(\theta) = ax\tan^{-1}\theta + bx + cx\tan\theta + dx\tan^2\theta + ex\tan^3\theta \tag{5}$$

Parameters *W, V, U, a, b, c, ax, bx, cx,* dx, ex were adjusted to best fit experimental data collected for a sufficiently large number of LaB6 peaks across the whole accessible 2θ range. Additional aberrations, indirectly affecting the IPF, include a 2θ zero error and capillary alignment errors in horizontal and vertical directions [13][14].
The following paragraphs show the IPF in standard operating conditions, which give the best flux available, a set-up chosen by the vast majority of users.

2.4.1 Standard operating conditions (SOC)

In order to maximize the flux at the detector, MCX operates by focusing the beam both in the vertical and in the horizontal plane at the detector level. Vertical divergence is controlled by acting on the second (bendable) mirror, whereas horizontal divergence is managed by acting

on the second (also bendable) crystal of the monochromator. The diffracted beam is collimated by setting the slits at a maximum aperture of 0.1 mm, to limit the effects of axial divergence.

Figure 19 shows the LaB_6 patterns collected in capillary configuration at 15 keV. Details of two low angle peaks are shown to demonstrate the quality of the IPF, which is very closely reproduced by the simple, symmetrical pseudo-Voigt profile. This provides a reliable parameterization according to equations (3)-(5), which can easily be used in LPA software [17][47], and in general, to represent in a reasonably accurate way the IPF at any desired diffraction angle. It is worth underlining that this favourable condition, unlike beamlines operating at other SR facilities, can easily be obtained across the 4-21 keV energy range and different sample environment conditions available at MCX.

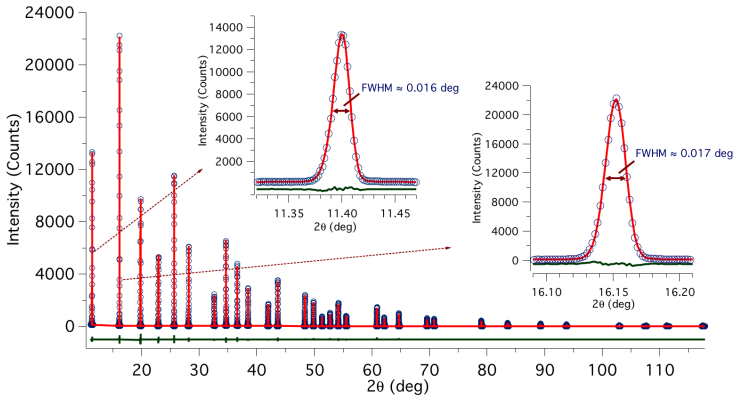

Figure 19: Standard LaB_6 powder pattern at 15 keV: experimental data (circle) and fit (line), with their difference (residual, line below). GoF is 0.647. Insets show details of low angle peak profiles.

Figure 20 shows a comparison of instrumental broadening at different energies. As photon energy is inversely proportional to the wavelength, Bragg's law provides for a decrease in FWHM with higher energies.

However, this condition is only verified at relatively low 2θ angles, whereas other factors in the powder geometry (e.g., absorption) and beamline set-up make the general dependence of FWHM on energy more complicated, which clearly requires an experimental determination like that shown in the present work.

By the way, it is possible to note that the bandwidth effects observed in paragraph 2.3.2, are also visible in the observed instrumental broadening energy dependence: at high angle, where the energy bandwidth effects are dominant [11][12], the profile of the FWHM at 11 keV is very close to that at 15 keV, because the DCM has a smaller energy bandwidth than the theoretical one at 11 keV, giving a smaller than expected broadening at high angle. Similarly, the larger bandwidth with respect to the theoretical one at 20 keV reduces the effects of narrowing the profile. These effects will be analysed in details in Chapter 5, through realistic ray-tracing simulations.

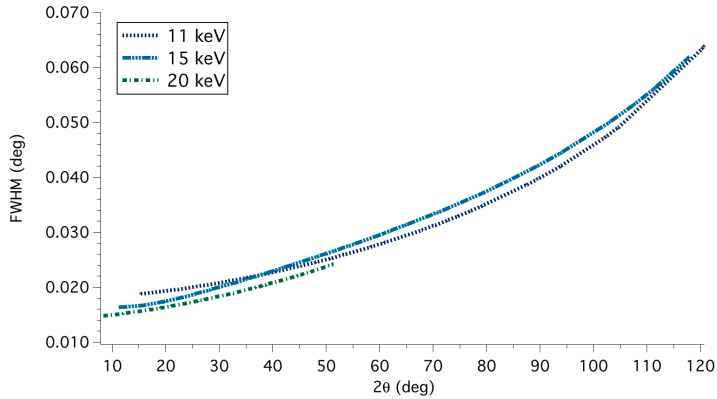

Figure 20: Instrumental broadening (represented as Full Width at Half Maximum – FWHM) at different beam energy: 11, 15 and 20 keV.

2.4.2 Optical characterization of the instrumental profile:

A more detailed study was made on the IPF at 11 keV beam energy, with the Si(111) analyser crystal installed on the detector arm. In particular, by acting on the monochromator and on the second mirror it is possible to reduce, respectively, horizontal and vertical divergence of the beam. As visible in Figure 21, relevant effects can be obtained working at the vertical divergence of the beam, i.e. in the plane of the diffraction signal, whereas reducing the horizontal divergence has little effect on the peak profile. In Figure 22 it is possible to see the effect on peak width and shape of defocusing the second mirror, so to narrow the instrumental peak profile down to 0.012°. While this improvement would of course be always desirable, the price to pay to achieve the narrowest instrumental profile is a 70% loss of the SOC flux.

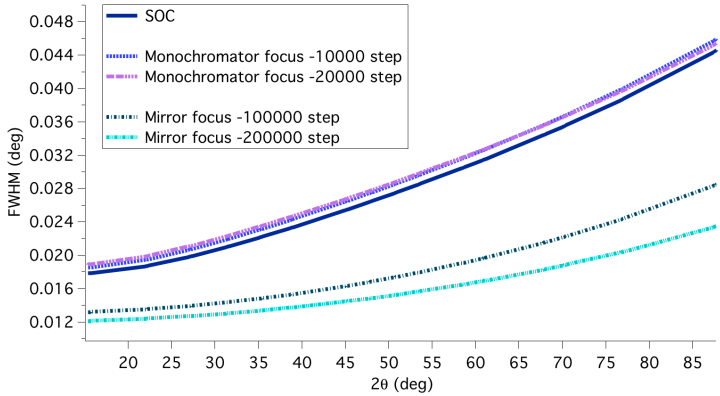

Figure 21: Instrumental FWHM vs. 2θ in capillary configuration. Defocusing is given in motor step units from the detector level (motors step 0).

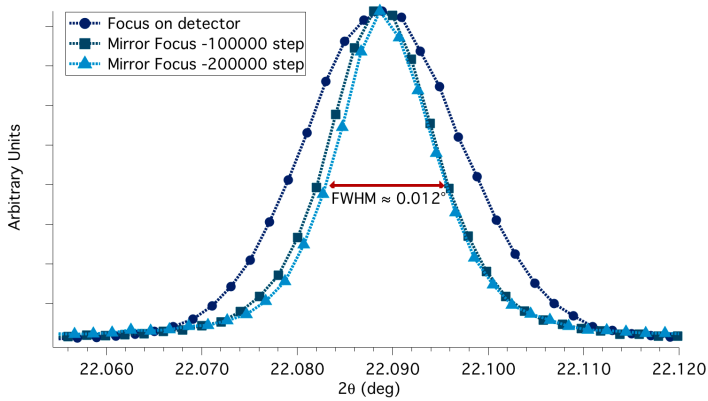

Figure 22: Effect of defocusing of the second mirror on the peak shape and width, LaB_6 (110) reflection at 15 keV.

As visible in Figure 23, in flat plate configuration concurrent effects of reducing the vertical divergence and increasing the beam spot lead to a less important effect on the FWHM.

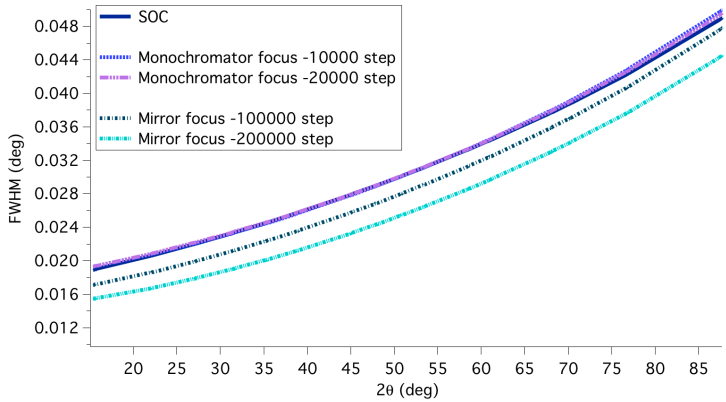

Figure 23: Instrumental FWHM vs. 2θ angle in flat-plate configuration. Defocusing is given in motor step units from the detector level (motors step 0).

It is worth noting that every modification of the optical layout leading to a widening of the beam footprint on the sample is detrimental with this

geometry, as it creates additional peak broadening. This is of course a major limitation in practical operation.

These results confirm, as expected, that the best resolution and IPF is obtained in the capillary mode, much more effective in limiting aberrations and instrumental broadening than the flat-plate configuration. The latter, however, has a practical value for specimens that cannot be used in capillary geometry, and is an added value and an asset of MCX in many materials science and technology studies.

2.5 Conclusions

Synchrotron radiation XRD can offer considerable advantages to a Line Profile Analysis, in terms of

(i) high statistical data quality,
(ii) narrow instrumental profile component,
(iii) possibility to enlarge the Ewald sphere (i.e., to measure more diffraction profiles) by using suitably high energy X-rays.

Advantages can also be exploited in non-ambient conditions, but for all of this to be true the beamline must be properly designed and operated, in particular to obtain a regular and controlled Instrumental Profile Function across a broad range of diffraction angles.

Results of this work, show that such a profitable condition is available at MCX, the Material Characterization by X-ray Diffraction beamline at Elettra Sincrotrone Trieste. An important challenge for the future is to further improve the operating conditions to allow reliable measurements of large crystalline domains, a subject with many possible applications, so to extend the current limits of Line Profile Analysis to the technologically relevant sub-micron region.

Chapter 3

Studies of nanostructured materials with large crystalline domains

Part of this chapter has been published in:

Claudia Malerba, Cristy Leonor Azanza Ricardo, Matteo Valentini, Francesco Biccari, Melanie Müller, Luca Rebuffi, Emilia Esposito, Pietro Mangiapane, Paolo Scardi, Alberto Mittiga

"Stoichiometry effect on Cu_2ZnSnS_4 thin films morphological and optical properties",
J. Renew. Sustain. Energy 6 (2014), 011404, doi: 10.1063/1.4866258

Cinira Fandaruff, Marcos Antônio Segatto Silva, Danilo Cesar Galindo Bedor, Davi Pereira de Santana, Helvécio Vinícius Antunes Rocha, Luca Rebuffi, Cristy Leonor Azanza Ricardo, Paolo Scardi, Silvia Lucia Cuffini

"**Correlation between microstructure and bioequivalence in Anti-HIV Drug Efavirenz**",
Eur. J. Pharm. Biopharm. 91 (2015), 52–5, doi: 10.1016/j.ejpb.2015.01.020

Abstract

LPA of two nanostructured materials with relatively large crystalline domains is described: Cu_2ZnSnS_4 (CZTS aka Kesterite), a solar absorbing semiconducting material and EVAVIRENZ, an anti-HIV drug. Both materials show an important dependence of their leading characteristics on the microstructural properties. In particular, the energy gap for CZTS and the Dissolution Efficiency for the EFAVIRENZ depend on the respective crystalline domain size distributions. Powder diffraction measurements of the required quality were made at the MCX beamline

of Elettra-Sincrotrone Trieste, with two different setups: Bragg-Brentano (flat-plate sample holder) for the Kesterite, and Debye-Scherrer for the EFAVIRENZ (capillary sample holder). In both studies the IPF appeared as a crucial feature, being the dominant part of the experimental signal.

3.1 Microstructural Properties of CZTS thin films

It was recently shown that the bandgap of CZTS, a p-type semiconductor with Kesterite structure showing promising behaviour as absorber in thin film solar cells, depends on stoichiometry and microstructure [48][49]. This correlation was studied in thin films prepared by sulfurization of multi-layered precursors of ZnS, Cu, and Sn, changing the relative amounts to obtain CZTS layers with different compositions. Crystalline domain size and presence of lattice defects was studied by LPA: as the available samples were thin films on glass substrates, the flat-plate geometry at MCX came in particularly handy (see Chapter 2).

A preliminary screening of the powder pattern showed the polycrystalline nature of the CZTS layer, with lack of significant crystallographic orientations, so that data could be analysed by WPPM [17] as for any polycrystalline material: layer thickness was sufficient to produce good quality patterns, with a broad halo from the amorphous glass substrate (modelled as part of the background function). Lattice defects seem not relevant in this case, so the refined microstructural parameters only refer to the crystalline domains [49].

The research investigates the correlation between Sn site occupancy and microstructure of the thin films. The study is made on a set of samples with different %Sn in the Kesterite film, obtained by varying the composition of the precursor, as reported in the following table:

Sample Name	Precursors [Cu]:[Zn]:[Sn]	E_{gap} (eV)
K265a2	2 : 1.48 : 1.06	1.48
K269a2	2 : 1.48 : 1.06	1.47
K264a2	2 : 1.48 : 1.06	1.48
K255a2	2 : 1.48 : 1.18	1.60
K256a2	2 : 1.48 : 1.18	1.63
K254a	2 : 1.48 : 1.18	1.63
K275a2	2 : 1.48 : 1.31	1.62

Optical measurements showed a variation of the energy gap of about 150 meV, from 1.47 to 1.63 eV, and the increase of the energy gap was correlated with the corresponding increase in the [Sn]/[Cu] ratio, which can be considered as a critical parameter, strongly influencing the optical properties of CZTS thin films. Moreover, the analysis showed a correlation between the Sn content in the CZTS films and the Sn-site occupancy, as visible in Figure 24.

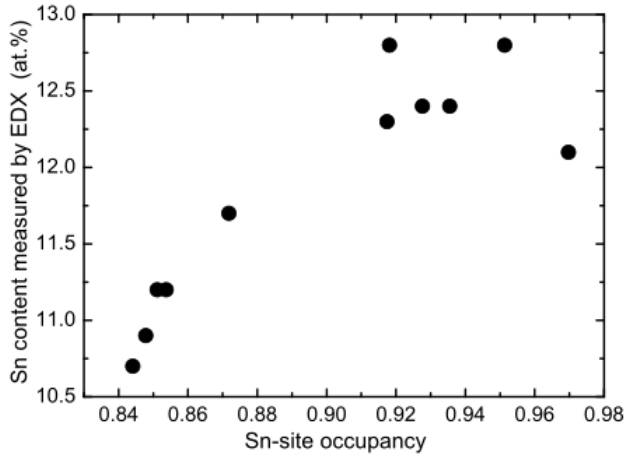

Figure 24: Correlation between the Sn content measured by EDX and the Sn-site occupancy obtained by quantitative analysis of XRD spectra.

Quantitative Phase Analysis (QPA) and refinement of the Sn site occupancy were made with the software TOPAS© [50][51] on diffraction patterns collected at different energies, so to highlight differences between chemical elements. The software PM2K [52] was instead used for the WPPM, to refine domain size and unit cell parameters.

A clear correlation between the Sn site occupancy and microstructural properties, in terms of crystalline domain size and cell parameters, emerged, as shown in Figure 25.

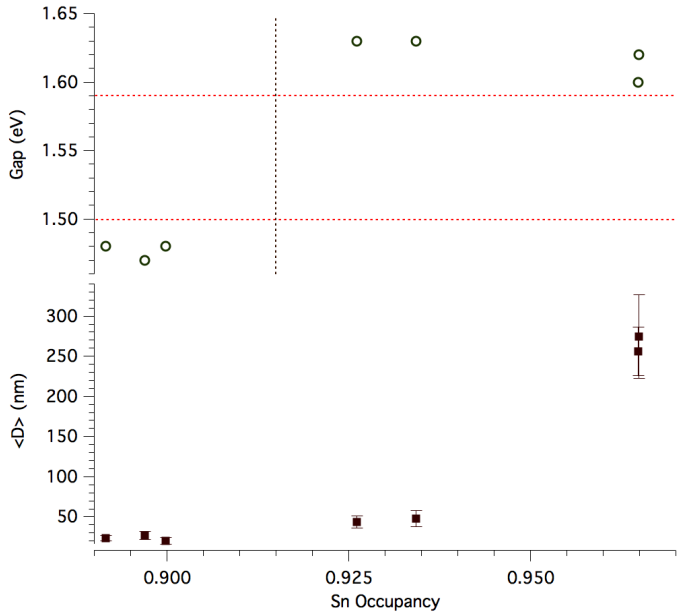

Figure 25: CZTS stoichiometry, expressed as Sn occupancy, correlates with the band gap energy (Gap, in eV) and with the crystalline domain size, here represented by the mean of a size distribution (<D> in nm) refined by the diffraction line profile analysis with the PM2K software.

As the tin content increases, three groups of size distributions (labeled with A, B, and C) are found (see Figure 26), with the following properties:

(i) small average crystalline domain size <*D*> with a narrow distribution (i.e., a small standard deviation),
(ii) small <*D*> values but with larger standard deviation,
(iii) uniformly large crystalline domains.

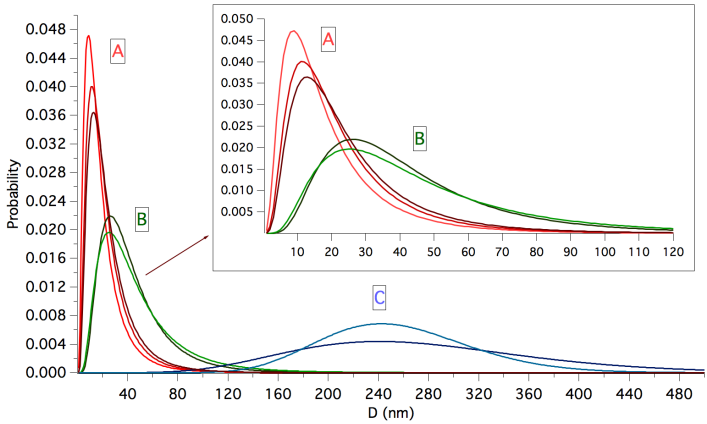

Figure 26: Domain size distribution for different CZTS thin films with different Sn content (increasing from A to C). The inset shows the first two distributions on a different scale.

Sphere-like crystalline domains are assumed and the analysis of the set of samples having small <*D*> (A and B) was performed with a lognormal distribution, while a gamma distribution was used for the last one (C).
A detailed account on this study can be found in [48][49], but it is worth considering herein the result shown in Figure 27, that belongs to a sample, having a low tin content and high bandgap (1.62 eV).
The inverse proportionality between domain size and peak width sets a limit to the largest domain sizes that LPA can actually measure, such that the usually accepted limit is 200 nm or less. The inset of Figure 27 shows

details of the most intense peak profile and a comparison with the instrumental profile that clearly demonstrate the refined size (mean value 275(52) nm) is above the conventional upper limit of LPA, but well within the sensitivity limits for the instrumental setup available at MCX.

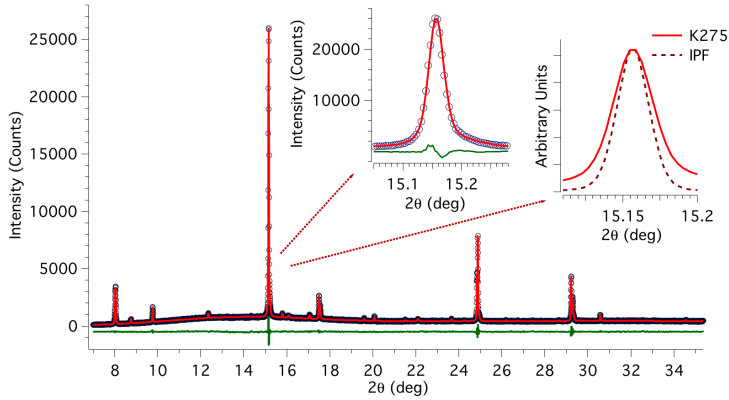

Figure 27: WPPM results for a CZTS thin film (sample K275a2, <D> = 275(52) nm): experimental data (circle), model (line), and their difference (residual, line below). Insets show details of the most intense line profile (solid line), with a comparison with the instrumental peak profile (IPF, dotted line).

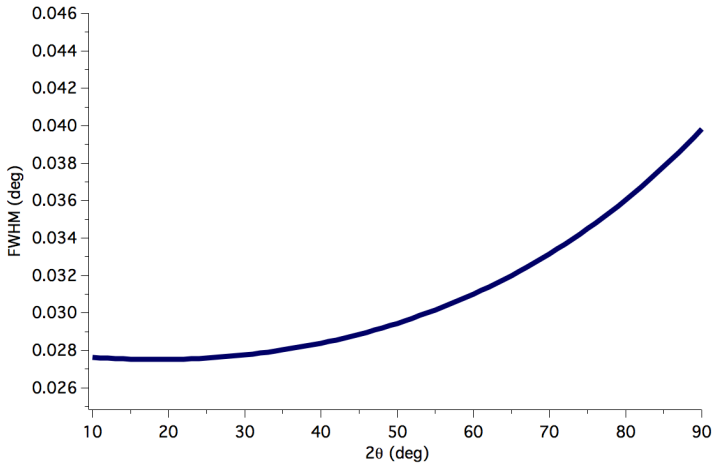

Figure 28: Calculated instrumental broadening for the CZTS thin films experimental setup

Calculation of the IPF has been made using the NIST SRM 660a LaB_6 [25] with a flat-plate sample holder. In Figure 28 it is possible to see the calculated instrumental broadening, obtained for the same experimental setup as the CZTS XRPD experimental patterns.

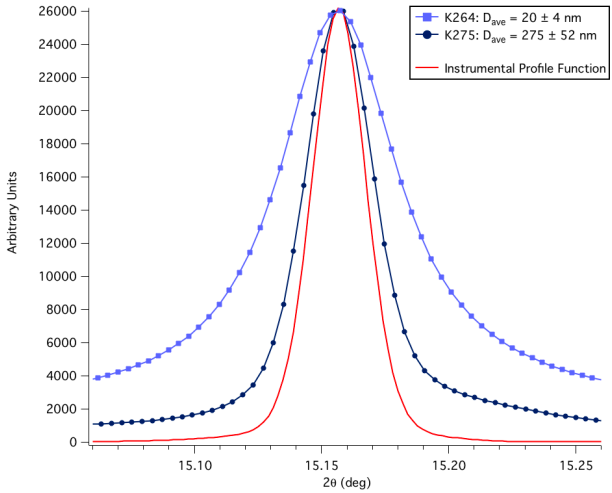

Figure 29: Kesterite XRD pattern at 15 KeV, comparison between the experimental data (line and circles) and calculated IPF (line)

Figure 29 shows the comparison between the IPF contribution and the experimental data of the samples with the smallest and the largest average crystalline domains size. It is worth underlying the importance of neatly describing the IPF: even if it is the dominant contribution to the line profile, the IPF at MCX is sufficiently narrow to provide reliable values of domain size up to several hundreds of nanometres.

3.2 Microstructural Properties of EFAVIRENZ

EFAVIRENZ (EFV) was approved for the treatment of human immunodeficiency virus type 1 infection (HIV-1) in 1998. Currently, it is considered the best choice in the treatment of adults and children with

the High Activity Antiretroviral Therapy (HAART) [53]. The generic version of EFV is a viable solution to offer quality medications to a much larger number of AIDS/HIV patients, provided that drug approval and registration are made according to existing national and international regulations covering the innovator's version. In this context, bioequivalence assessment is the most important quality control tool in the process of a generic product development and registration, in order to ensure its therapeutic efficacy [54][55].

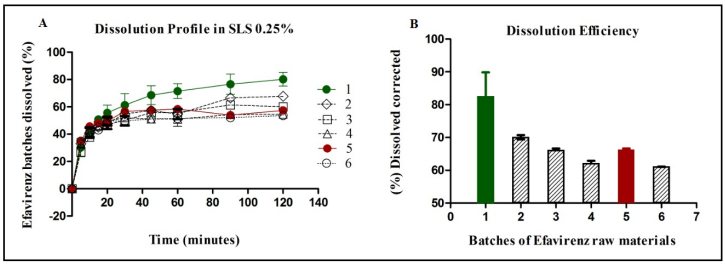

Figure 30: A) Powder dissolution profile in sodium lauryl sulphate 0.25% versus time. B) Dissolution Efficiency of six EFV batches of raw materials. Batch 1 passed the bioequivalence test, whereas batch 5 did not.

The bioequivalence in vivo studies were conducted on healthy volunteers whose age ranged between 18 and 45 years, and results are correlated to in vitro dissolution tests. The powder dissolution profiles of the six EFV batches in sodium lauryl sulphate are shown in Figure 30A, with the corresponding Dissolution Efficiency (DE) plotted in Figure 30B. Details on materials and methods are available in [56].

Batch 1, a positive result in the *in vivo* bioequivalence test, showed the best dissolution behavior with the highest DE (~82%); in contrast, batch 5, which did not pass the bioequivalence test, was around 66%.

As detailed in [56], the origin of the DE behavior here observed is also commonly explained by other factors, such as morphology, particle size distribution and/or impurities, but all of these factors were excluded as

possible causes during this study, in particular, in Figure 31A and Figure 31B is possible to observe how particle size distribution parameters after micronization routine process, like volume-weighted average size or surface-weighted average size (here called d[4,3], d[3,2], respectively), show no significant correlation with DE.

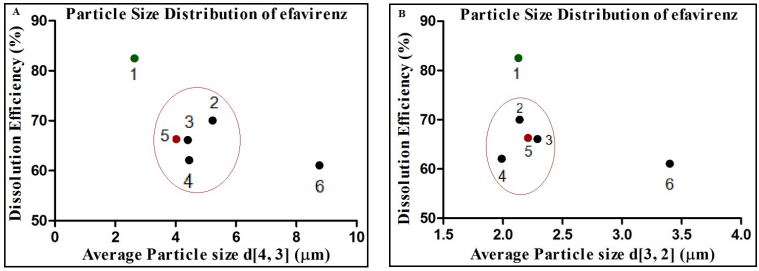

Figure 31: A) E versus Average Particle size, and DE versus Average crystalline domain size, for six batches of EFV raw materials. Batch 1 passed the bioequivalence test, whereas batch 5 did not. A) DE versus Average Particle size d[4, 3]. B) DE versus Average Particle size d[3, 2].

Dissolution and bioavailability of pharmaceutical raw materials and products do not have been traditionally correlated to crystalline domain size, that so far has not been an issue for pharmaceutical analysts and formulators. As a consequence, microstructure properties to the level of crystallite size have never been correlated with biopharmaceutical characteristics or process considerations.

Structural and microstructural analysis was based on SR XRPD measurements made at the MCX beamline using the Debye-Scherrer (capillary) geometry (see Chapter 2).

Structural information was obtained by modelling the data with the software TOPAS© [50][51]: all samples were identified as EFV polymorph 1, with space group $P2_12_12$ and cell parameters a = 16.781 Å, b = 27.258 Å, c = 9.698 Å (data collected at 250K [57]).

Microstructural information was provided by the analysis of the diffraction line profiles, using the software PM2K [52], representing the

EFV crystallites as equiaxed crystalline domains, the latter modelled as spheres with a lognormal distribution of diameters D.

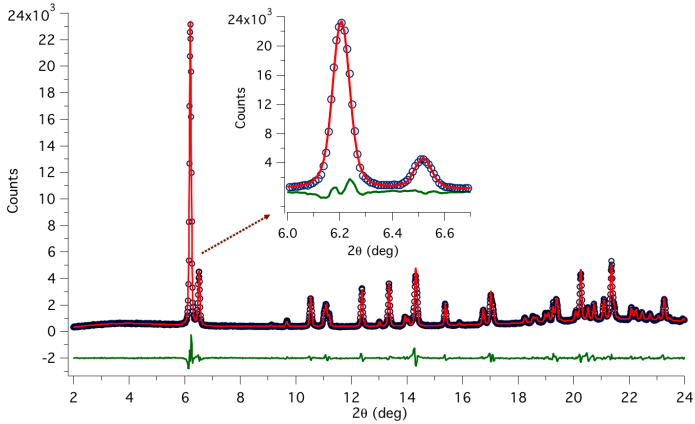

Figure 32: EFAVIRENZ XRD pattern at 8 KeV, comparison between the experimental data (line and circles) and calculated IPF (line)

We also considered the possible presence of a strain broadening contribution, based on a rather general strain model constrained by the symmetry of the elastic tensor for the specific Laue group of EFV [17][58][59]. However, no significant improvement to the modelling was observed by adding this component, which can therefore be considered as negligible in the present case.

Figure 32 shows the result of the PM2K software for the diffraction pattern of one of the samples (batch 5). The result is acceptable, although some non-random discrepancy is observed between data and model, as a possible result of more complex dispersion of the domain size, or of non-spherical domain shapes.

Calculation of the IPF has been made with and NIST SRM 640a Si [60] diluted with an amorphous material (starch) in order to reproduce the same low absorption condition of an organic material as EFAVIRENZ.

Figure 33 shows the calculated instrumental broadening, obtained in the same experimental setup as the CZTS XRPD patterns measurement.

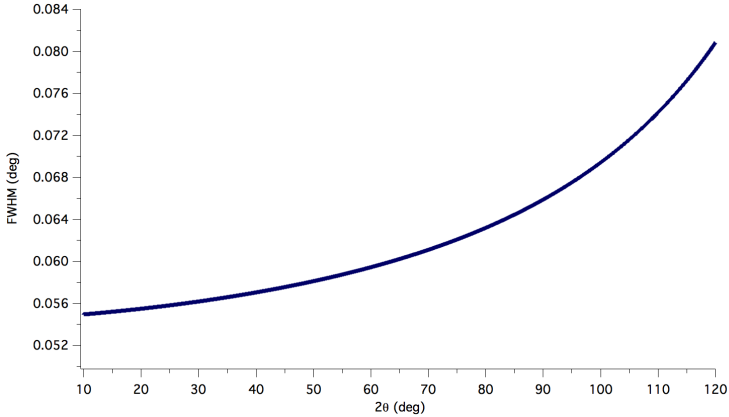

Figure 33: Calculated instrumental broadening for the EFAVIRENZ experimental setup.

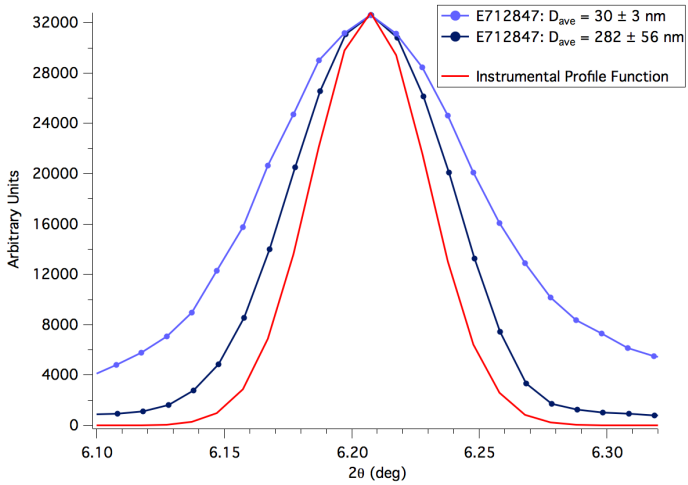

Figure 34: EFAVIRENZ XRD pattern at 8.048 KeV, comparison between the experimental data (line and circles) and calculated Instrumental Profile Function (line)

Figure 34 shows the comparison between the IPF contribution and the experimental data of the samples with the smallest and the largest average crystalline domains size, remarking the dominant contribution of the instrumental profile also in this study.

Using this methodology, besides mean size values, the distribution can be determined, and beyond fine differences and possible discrepancies between data and models, the crystalline domain size was found to span quite different values, from a few tens to hundreds of nanometers. Figure 35 shows the crystalline domain size distributions for all the measured specimens of this study.

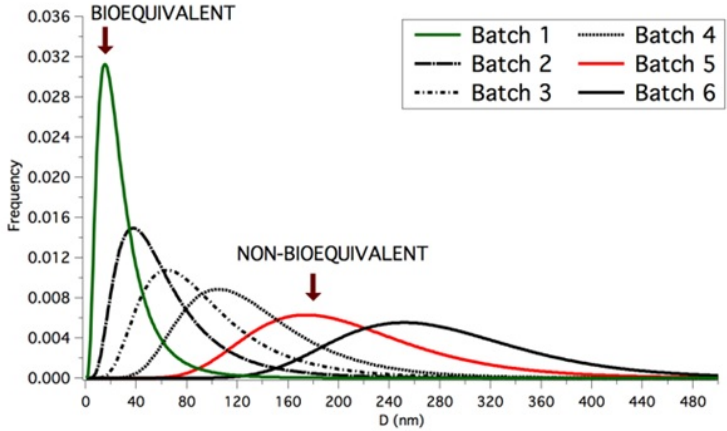

Figure 35: Crystalline domain size distributions for the six EFV batches of this study.

In order to determine the effect of microstructure in the dissolution assays and bioequivalence studies, DE was compared with the average crystalline domain size. Figure 36 clearly shows the correlation: larger crystalline domain sizes (above ~100 nm) correspond to the lower DE values, as opposed to results in Figure 31A and Figure 31B, showing no

clear correlation between DE and average particle sizes, d[4,3] and d[3,2], mainly for batches with comparable particle sizes.

Most importantly, the significant difference in bioequivalence essays or *in vivo* studies presented by batches 1 and 5 can be explained by this evidence. Batch 1, with the approved bioequivalence essay, shows the smallest crystalline domain size (D = 30(3) nm) whereas batch 5, with a not approved bioequivalence assay, has crystalline domains more than 6 times larger (D = 208(42) nm).

Finally, an important remark: the present results suggest that there could be a critical crystalline domain size and particle size distributions to ensure the bioequivalence.

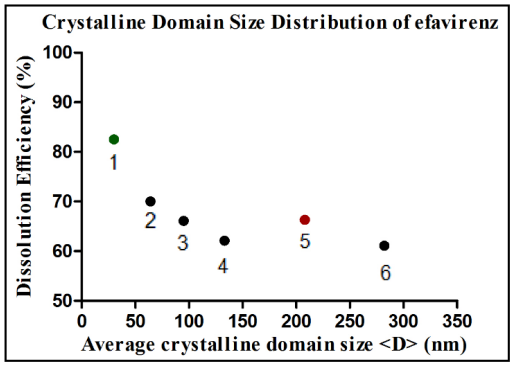

Figure 36: DE *versus* Average crystalline domain size <D> (nm).

3.3 Conclusions

The possibility of characterizing microstructural properties of nanostructured materials in a wide range of values could be a crucial added value to the investigation on those parameters that are mainly connected to their principal and qualifying properties. This chapter discussed two different studies with nanostructured materials where the crystalline domains size distribution ranged from few tens of

nanometres to much larger values, very close to the upper limit of applicability of LPA methods.

What emerged from the results of this studies and the data analysis itself is that the capability of modelling and keeping under control the instrumental profile function of a SR beamline is a vital condition to explore microstructure of this sort of materials.

Appendix A: WPPM principles and formulas

This appendix, containing details of the LPA method used in this chapter, is extracted from [17].

Basic Principles

The WPPM procedure is based on the fact that the observed diffraction line profile is a convolution of the line profiles produced by all contributing effects:

$$I(s) = I^{IP}(s) \otimes I^{S}(s) \otimes I^{D}(s) \otimes \ldots \tag{A1}$$

In Eq. (A1), s is the reciprocal space variable (numerically equal to $\frac{2\sin\theta}{\lambda}$, with θ and λ as the diffraction angle and X-ray wavelength, respectively), *IP* stands for Instrumental Profile, *S* for coherent scattering domain size/shape, *D* for lattice distortions (e.g. due to dislocations). The computationally demanding convolution integral of Eq. (A1) can be simplified via the convolution theorem, stating that the Fourier Transform of a convolution is the product of the Fourier Transforms of the terms to be convolved. Eq. (A1) can be therefore rewritten as:

$$\begin{aligned} I_{hkl}(s) &\propto \int_{-\infty}^{+\infty} \prod_{j} A_{hkl}^{j}(L) e^{-2\pi i L \cdot s} dL \\ &= \int_{-\infty}^{+\infty} \left[A_{hkl}^{IP}(L) \cdot A_{hkl}^{S}(L) \cdot A_{hkl}^{D}(L) \cdot \ldots \right] e^{-2\pi i L \cdot s} dL \end{aligned} \tag{A2}$$

where L is the Fourier length and the $A_i(L)$ are the Fourier Transforms of the individual profile functions proposed in Eq. (A1).

Instrumental profile function

A pseudo-Voigt can be written as function of the distance from Bragg position:

$$pV\left(x=2\theta-2\theta_{hkl}\right)=I_0\left[\left(1-\eta\right)e^{-\ln 2\frac{x^2}{\omega^2}}+\eta\left(1+\frac{x^2}{\omega^2}\right)^{-1}\right] \quad \text{(A3)}$$

with three parameters: I_0, a scale parameter, η, the Lorentz fraction, and ω, the half width at half maximum. With these definitions, the Fourier Transform can be written as:

$$A_{pV}^{IP}\left(L\right)=\left(1-k\right)e^{-\frac{\left(\pi\sigma_s L\right)^2}{\ln 2}}+ke^{-2\pi\sigma_s L} \quad \text{(A4)}$$

Where $k=\left[1+\frac{1-\eta}{\eta\sqrt{\pi\ln 2}}\right]^{-1}$ and $\sigma_s=\frac{\omega\cos\theta}{\lambda}$.

Domains size contribution: lognormal and gamma distributions

In many practical cases it is possible to use a lognormal (g_l) or a gamma (g_Γ) distribution of simple shape domains, with just one length parameter D (diameter (sphere) or edge (cube, octahedron, tetrahedron)) [61]:

$$g_l\left(D\right)=\frac{1}{D\sigma\sqrt{2\pi}}e^{-\frac{\left(\ln D-\mu\right)^2}{2\sigma^2}} \quad \text{(A5)}$$

$$g_\Gamma\left(D\right)=\frac{\gamma}{M_{\Gamma,1}\Gamma\left(\gamma\right)}\left(\frac{\gamma D}{M_{\Gamma,1}}\right)^{\gamma-1}e^{-\frac{\gamma D}{M_{\Gamma,1}}} \quad \text{(A6)}$$

where μ and σ are lognormal mean and lognormal variance, respectively, whereas $M_{\Gamma,1}$ is the mean of the gamma distribution (first moment) and γ is the ratio between square of the mean and variance: $\gamma = \frac{M_{\Gamma,1}^2}{\left(M_{\Gamma,2} - M_{\Gamma,1}^2\right)}$. Distribution moments are:

$$M_{l,n} = e^{n\mu + \frac{(n\sigma)^2}{2}} \tag{A7}$$

$$M_{\Gamma,n} = \left(\frac{M_{\Gamma,1}}{\gamma}\right)^n \frac{\Gamma\left(n+\gamma\right)}{\Gamma\left(\gamma\right)} \tag{A8}$$

so that mean and variance are: $\left\langle D \right\rangle_l = M_{l,1} = e^{\mu + \frac{\sigma^2}{2}}$, $\mathrm{var}_l = e^{2\mu+\sigma^2}\left(e^{\sigma^2} - 1\right)$ and $\left\langle D \right\rangle_\Gamma = M_{\Gamma,1}$, $\mathrm{var}_\Gamma = \frac{M_{\Gamma,1}^2}{\gamma}$, respectively for lognormal and gamma distribution.

The FTs for the case of spherical domains are:

$$A_l^S\left(L\right) = \frac{1}{2} Erfc\left[\frac{\ln\left|L\right| - \mu - 3\sigma^2}{\sigma\sqrt{2}}\right] - \frac{3}{4}\left|L\right| Erfc\left[\frac{\ln\left|L\right| - \mu - 2\sigma^2}{\sigma\sqrt{2}}\right] e^{-\mu - \frac{5}{2}\sigma^2} + \\ + \frac{1}{4}\left|L\right|^3 Erfc\left[\frac{\ln\left|L\right| - \mu}{\sigma\sqrt{2}}\right] e^{-3\mu - \frac{9}{2}\sigma^2} \tag{A9}$$

$$A_\Gamma^S\left(L\right) = \frac{\left\{\frac{1}{2}\left(\frac{L\gamma}{\mu}\right)^3 \Gamma\left[\gamma, \frac{L\gamma}{\mu}\right] - \frac{3}{2}\frac{L\gamma}{\mu}\Gamma\left[\gamma+2, \frac{L\gamma}{\mu}\right] + \Gamma\left[\gamma+3, \frac{L\gamma}{\mu}\right]\right\}}{\Gamma\left[y+3\right]} \tag{A10}$$

Chapter 4

A proposed reference material for Line Profile Analysis

Part of this chapter has been published in:

Luca Rebuffi, Andrea Troian, Regina Ciancio, Elvio Carlino, Paolo Scardi

"A proposed reference material for Line Profile Analysis",
submitted to Journal of Applied Crystallography

4.1 Abstract

An iron-molybdenum alloy powder was extensively deformed by high energy milling, so to refine the bcc iron domain size to nanometer scale (≈10 nm) and introduce a strong inhomogeneous strain. Both features contribute to comparable degree to the diffraction peak profiles, so that size and strain broadening can be easily separated by exploiting their different dependence on the diffraction angle. Further properties of this powder sample, easily produced in large batches, make it a good candidate as a reference material for diffraction LPA, in particular for separating size and strain broadening effects. Evidence from other techniques, including scanning and Transmission Electron Microscopy (TEM) and Small Angle X-Ray Scattering (SAXS), confirms the extent of the size broadening effect, and provides insight into the origin of inhomogeneous strain in plastically deformed materials.

4.2 Introduction

LPA is used since the discovery of powder diffraction, nearly a century ago, to determine size and shape of crystalline domains, and to assess presence and content of lattice defects. Even if traditional methods are described in most textbooks on powder diffraction [3][62][63][64], LPA is still a subject of active research [1][4][58][65], with development of new methodologies and increasing applications, ranging across most fields of science and technology. Recent examples include materials growth processes [66][67], and the study of the effects of thermal or mechanical treatments [68][69][70].

As mentioned in Chapter 1, despite the considerable interest in LPA, there are no established procedures and no reference materials to compare results, validate methods and experimental protocols.

SRMs, so far, were only introduced to measure the IPF [24][25][60], which is useful and functional to a proper use of LPA, but gives no support to the study of line broadening effects caused by the microstructure of materials. Recent research effort focused on ZnO powders as possible crystallite size SRMs [71]. The certification work of NIST SRM 1979, still in progress for the complexity of the microstructure (extensive layer faulting in prismatic domains with small aspect ratio), should deliver a standard for size effects in diffraction line broadening.

The present chapter reports the first part of a collaborative project involving several laboratories, aimed at producing and testing a possible reference material for LPA, including both *size* and *strain* effects. Part one is dedicated to material production and characterization, whereas part two will be dedicated to a Round Robin (RR), involving a number of laboratories to test experimental LPA practices and analytical methods. To date, only one similar RR project has been reported [72], but the scope was quite different. The studied sample was a chemically

synthesized nanocrystalline ceria powder, with a mean domain size of less than 20 nm. Presence of a strain broadening component was mentioned as a minor effect, if not as an artefact of some data analysis procedures. Before this work, a similar project based on glass-ceramic specimens had been started and discussed at the first Size-Strain conference ("Size – Strain '95", Liptovski Mikulas, Slovakia, August 21-25, 1995), but results were not conclusive, and no written report was included in the following publication [65].

The material of our study was selected according to several requirements, but also to be representative of a broad class of problems and case studies in chemistry, physics and materials science. The choice of a heavily deformed bcc iron-alloy powder produced by high energy milling was supported by:

(i) presence of a single-phase, with high symmetry crystal structure (bcc), such to produce powder diffraction peaks with as little overlapping as possible,
(ii) line broadening effects due to small domain sizes and inhomogeneous strain, with the latter caused mostly by domain interactions and presence of a dominant lattice defect type, namely dislocations, causing an anisotropic (*hkl*-dependent) line broadening,
(iii) contaminant phases present in a reasonably low and controlled level, not interfering significantly with the LPA,
(iv) good stability in time,
(v) large amount of material available by a simple, inexpensive and straightforward preparation process. It is also important the procedure be fully reproducible.

In this chapter we present the material and provide a detailed characterization – which could be the basis of a certification protocol – using several standard techniques of materials science. Results also shed

light on the mechanism of plastic deformation in metallic materials undergoing extensive grinding.

4.3 Materials and Methods

The Fe-1.5wt%Mo alloy (Astaloy Mo®) supplied by Höganäs (Sweden) [73] is a pre-alloyed powder for large industrial production, mostly used in powder metallurgy processes. Molybdenum, entering the bcc crystal structure of iron in solid solution, is added to increase hardenability and to improve the mechanical properties by a solution-hardening effect. The latter is caused by the lattice strain introduced by alloying Mo, with a smaller atomic radius, to the host matrix of Fe. Molybdenum addition also enhances thermal stability, as it hinders grain growth (and recrystallization) processes, thus stabilizing the work-hardening effects introduced by grinding. At the same time Mo does not increase the tendency of oxidation, which would lead to unwanted secondary oxide phases [74].

The Fe-1.5wt%Mo (hereinafter FeMo) powder was ground in a planetary ball mill (Pulverisette 4, manufactured by Fritsch GmbH, Idar-Oberstein, Germany [75]), using two 250 ml jars of X210Cr12 steel designed and made at the University of Trento [76][77]. Milling agents were 50 tempered steel (100Cr6) spheres, with a diameter of 12 mm and a mass of 7.1 g.

Milling parameters were based on previous studies [78]: main disk speed (Ω) was 300 rpm, whereas the speed ratio (ω/Ω) was -1.8, with ω as the rotational speed of the satellite jars. The ball to powder ratio (BPR) was set to 10:1. Grinding was made in static Ar atmosphere (O_2 < 2%) and Room Temperature (RT) conditions, with a 4wt% ethanol (96%vol purity) added as lubricant, to avoid cold welding and sticking of the powder to the jar walls.

Eight batches were produced and individually characterized [76][77], showing similar microstructural parameters. Batch 4, jar A was selected for the present study as it gives results close to the average values for the whole production.

X-ray Diffraction (XRD) patterns were collected at the MCX beamline of the Italian synchrotron Elettra-Sincrotrone Trieste [79][26], using the standard capillary geometry and a beam energy of 15 keV (λ = 0.0826 nm). Details on the beamline are also described in Chapter 2.

SAXS data were collected at the same synchrotron radiation facility, using the standard set-up described in [80].

Morphological investigation of the selected batch was carried out by a ZEISS Supra 40 field-emission gun (FEG) Scanning Electron Microscope (SEM) equipped with a Gemini column and an in-lens detector yielding increased signal to noise ratio. The microscope is also provided with an EDAX system for energy dispersive X-ray spectroscopy (EDS) studies.

HRTEM analyses were performed by using a JEOL 2010 UHR field emission gun microscope operated at 200 kV with a measured spherical aberration coefficient, Cs, of 0.47(1) mm, which enables a resolution in phase contrast at optimum defocus of 0.19 nm.

4.4 Results and Discussion

High-energy ball milling of a FeMo powder has been described as a three-stage process [78]: last stage, set in after extensive grinding (>32 h), yields a homogeneous microstructure made of roughly equiaxed nanocrystalline domains with a high density of dislocations. However, even under the most effective conditions, ball milling effects tend to saturate as a dynamical equilibrium establishes between plastic deformation and annealing, so that the domain size and lattice defect content do not change any further with additional milling.

With the milling equipment used in this work, 64 hours is the appropriate grinding time for the production of a large amount of powder with a uniform microstructure [76][77][78]. The total time including testing, run in of jars and balls, and production of 4 batches is suitable to guarantee stability of the grinding media, which undergo rather severe in-service degradation, and limit contamination of the powder.

Powder particle morphology is also important. While the extensive grinding decreases the domain size to nanometer scale, as a result of a fragmentation process triggered by localized deformation, there is a strong tendency toward agglomeration. Starting from the ~90 μm grain size of the pristine powder, Figure 37 shows that ball milled particles range from a few to a few tens of micrometers.

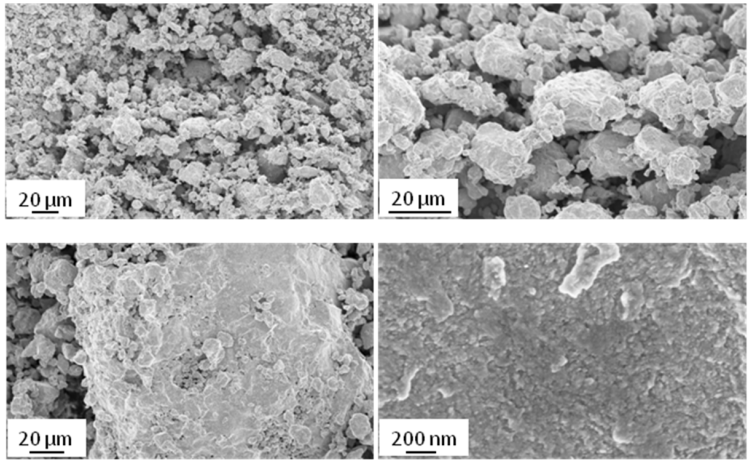

Figure 37: SEM micrographs at different magnification of the FeMo powder ground for 64 hours.

At the highest magnification nanocrystalline domains can be outlined as fine features in much larger particles. A tentative analysis indicated a

mean size of ~15 nm, with a standard deviation (s.d.) of ~4 nm (see Figure 38).

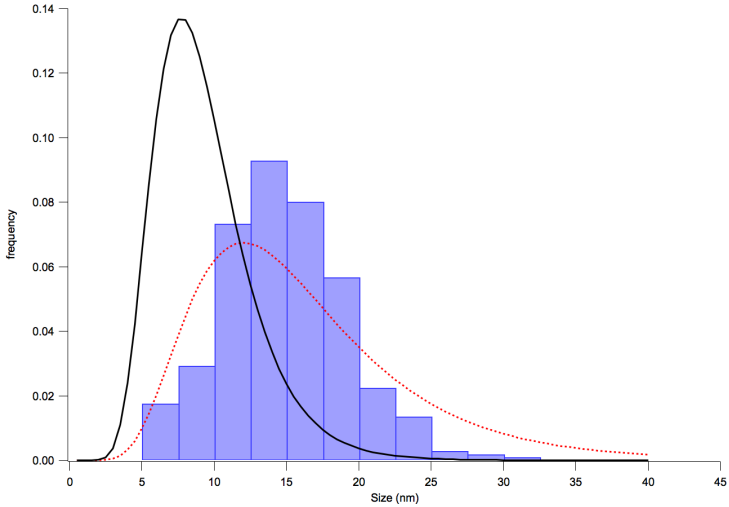

Figure 38: Histogram of particle size from SEM micrographs (400 particles, min. size limit 5 nm, mean 14.5 nm, s.d. 4.2 nm); lognormal size distribution of diameters from SAXS (red dot: mean 16.2 nm, s.d. 7.6 nm) and Whole Powder Pattern Modelling (WPPM) of XRD data (black line: mean 9.3(8) nm, s.d. 5.9(9) nm). See text for details.

It is clearly understood this is not the crystalline domain size, but it can be considered as an upper limit for the true value. Likewise, a SAXS measurement of a specimen of ball milled FeMo powder dispersed in water gave a mean size of ~16 nm and standard deviation of 8 nm (courtesy of Dr. Heinz Amenitsch, Graz University of Technology). As SAXS is mostly sensitive to the particle size/shape, the agreement between this size value and that obtained from the SEM pictures confirms that 15-16 nm can be safely considered as an upper bound to the true crystallite size.

Agglomeration has a positive effect on the FeMo powder for the specific purpose of this work, because it limits oxidation. Spontaneous passivation, in fact, only concerns the agglomerate surface, thus limiting

the formation of oxide phases which indeed are not observed in the diffraction pattern, even after long time [76][77]. The SEM analysis was also used, with the support of EDS, to assess the level of contamination from the grinding media. After the preliminary run in and grinding tests, which presented relatively high levels of chromium and nickel contamination from vial and balls, Cr and Ni content in the powder milled for 64 h stabilized to 3wt% and 1wt%, respectively, in good agreement with the overall chemical composition of the milling apparatus. These values, however, are likely to be an upper limit to contamination, as the EDS analysis is mostly sensitive to the surface of the agglomerates, where most impacts with the grinding media take place. The Cr-Ni contamination has therefore the effect of a mechanical alloying, giving the potentially positive effect of protecting the FeMo agglomerate particles from oxidation, granting stability in ordinary use and storage conditions (see below). Under the same conditions, the EDS analysis on the pristine powder gave an average composition of 98.68%wt Fe/1.32wt% Mo, against the nominal 98.5/1.5 ratio.

Before LPA, FeMo XRD data were corrected for absorption effects. The transmitted beam was measured under the same experimental conditions used to collect the powder diffraction data, by moving the capillary through the beam aimed straight at the detector [76][77]. Same procedure was repeated for the studied capillary and an empty one. A transmitted beam percentage of 9.2(1) % was measured, corresponding to a FeMo powder packing factor of 46% and a product of absorption coefficient (μ) and capillary radius μR = 1.19. Standard expressions for capillary geometry [81] were used to correct the powder data for absorption [76][77].

The corrected FeMo data were analysed by WPPM [17][58][82], following a well-assessed procedure [78]. The equiaxed crystalline domains were described as a system of spheres with lognormally distributed diameters, containing straight dislocations of screw and

edge type. Diffraction line profile components related to domain size/shape and to dislocations were convolved with the IPF to model the experimental data by non-linear least squares minimization [58][82].

Free microstructural parameters in the refinement procedure were: lognormal mean (μ) and variance (σ) of the diameter distribution, average dislocation density (ρ) and effective outer cut-off radius (R_e). The anisotropic broadening effect of dislocations, according to the Krivoglaz-Wilkens theory [83][84][85], was described by an average contrast factor calculated for screw and edge dislocations in the primary slip system of bcc iron (1/2<111>{110}) [78]. To account for the dislocation type, an edge/screw fraction parameter (f_E) was also refined. Additional refinement parameters include the unit cell parameter (a_0), coefficients of optical aberration functions (horizontal/vertical position of the capillary) and background. Concerning the latter, the pattern from an empty capillary was modelled by a set of pseudo-Voigt functions, and this model, with all parameters fixed but a single refinable scale factor, was added to a Chebyshev polynomial to fit the background in the analysis of the FeMo data.

Figure 39 shows the WPPM result, with details on the two most intense reflections in the insets. Modelling quality is good, even if some non-random feature is visible in the residual for the most intense (lowest angle) reflection. The corresponding distribution of spherical domain diameters is shown in Figure 38. There it can be seen, as expected, that domain size is markedly smaller than particle size seen by SEM and SAXS. Arithmetic mean size is $\langle D \rangle$ = 9.3(8) nm, with s.d. of 5.9(9) nm. It is also worth considering the volume-weighted and surface-weighted mean sizes, respectively, $\langle D \rangle_V$ = 10.9(9) nm and $\langle D \rangle_S$ = 10.2(9) nm. The former is related to the integral breadth of the diffraction peaks (through a shape factor, aka Scherrer constant, K_β = 4/3 [61][86], whereas the latter is usually evaluated by the Warren-Averbach method [87][88] (with a corresponding shape factor of 3/2 [61][86]). Owing to

the relatively little dispersion – narrow domain size distribution – differences among the three mean values are correspondingly small (< 30%).

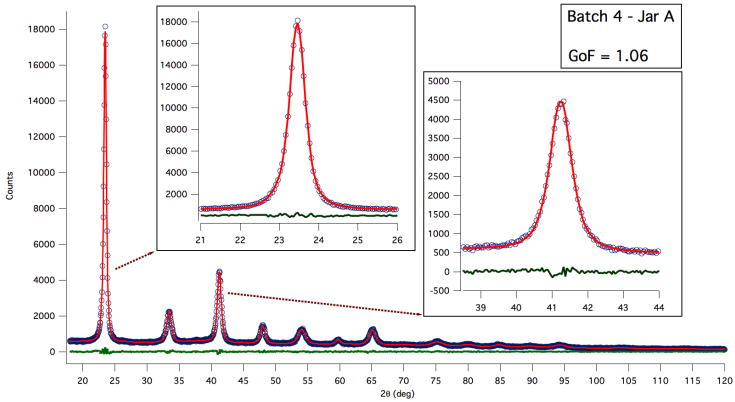

Figure 39: WPPM results: experimental data (circle), model (line) and residual (line below). Insets show details of the modelling of the two most intense reflections.

The WPPM analysis also gives parameters of the strain profile component, which in terms of dislocations effect are: ρ = 4.5(4) 10^{16} m^{-2}, R_e = 4.3(4) nm, f_E = 0.54(3). It is worth noting that the so-called Wilkens parameter ($R_e\sqrt{\rho}$) is about unity, which is just within the validity limits of the theory [84][85], and would suggest a strong dislocation interaction, as in dislocation walls and dipoles [84][85].

Even if the refined values make sense, questions may arise about their actual meaning, in particular regarding ρ. The refined dislocation density is quite high, as it would correspond to about two dislocations per spherical domain (for a mean diameter of 9.3 nm: $< D > / \left(\frac{\pi < D >^3}{6} \right) \approx$ 2.2 10^{-16} m^{-2}).

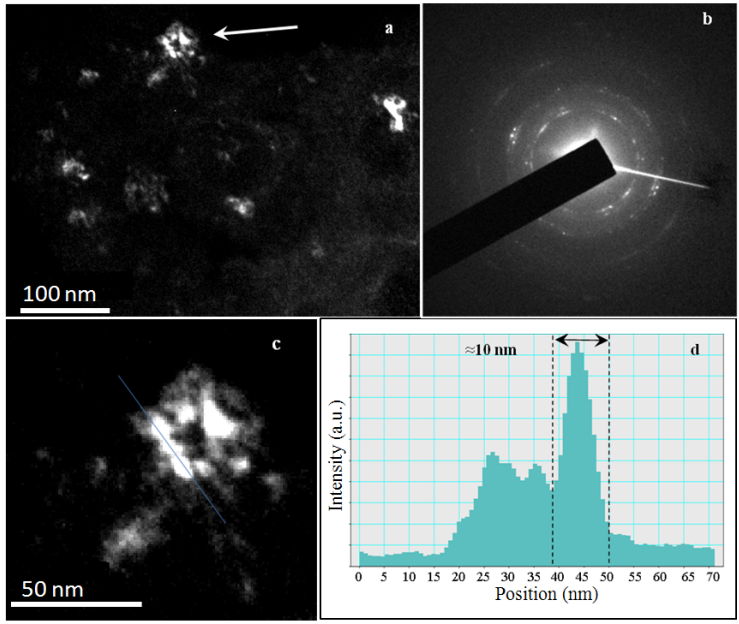

Figure 40: Dark field TEM pictures of a ball milled FeMo powder specimen. Overview of the microstructure (a) and corresponding electron diffraction pattern (b); detail of the region pointed by the arrow (c), with line scans across image intensity maxima (d). See text for further details.

TEM provides an indispensable support to the present study, to shed light on the actual size of the FeMo domains and on the lattice defects. TEM showed the internal fragmentation of the FeMo domains, not accessible to SEM or SAXS due to their intrinsic resolution limits. A representative overview of nanocrystalline FeMo is shown by the dark field image of Figure 40A obtained by selecting a single (0,*k*,*l*) FeMo diffraction spot to form the TEM image. Overall, grains tend to cluster into equiaxed agglomerates with random orientation (cf. the electron diffraction pattern in Figure 40B) ranging from 20 to 50 nm average size, which in turn consist of enclosed bright contrast sub-grain units. The dark field image in Figure 40C depicts, at higher magnification, the

representative case of the cluster pointed in Figure 40A, where the internal fragmentation can be distinctly appreciated.

Line scans across image intensity maxima measured along relevant portions of the imaged cluster confirmed the enclosed presence of domains of about 10 nm, in good agreement with the XRD/WPPM results.

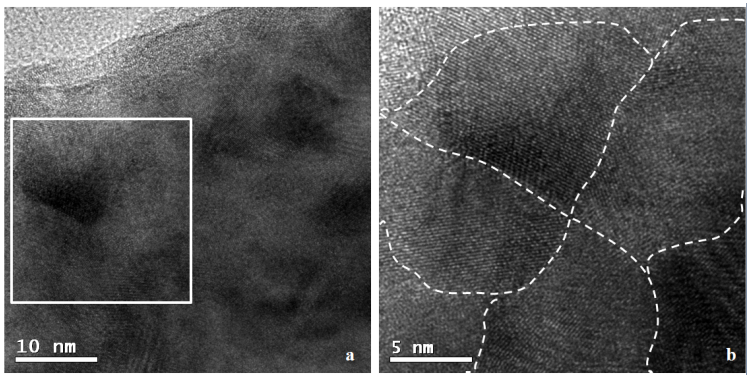

Figure 41: High resolution electron microscopy picture of a ball milled FeMo powder specimen. Region framed by the square in (a) is shown at higher magnification in (b), with indication of the grain boundaries (dash lines).

High Resolution Transmission Electron Microscopy (HRTEM) provides details on the high-angle grain boundary structure surrounding crystalline domains. The micrograph in Figure 41 shows an example: the area framed by the white box in Figure 41A and shown at higher resolution in Figure 41B depicts the case of four grains facing to each other where the boundaries have been marked by dashed lines.

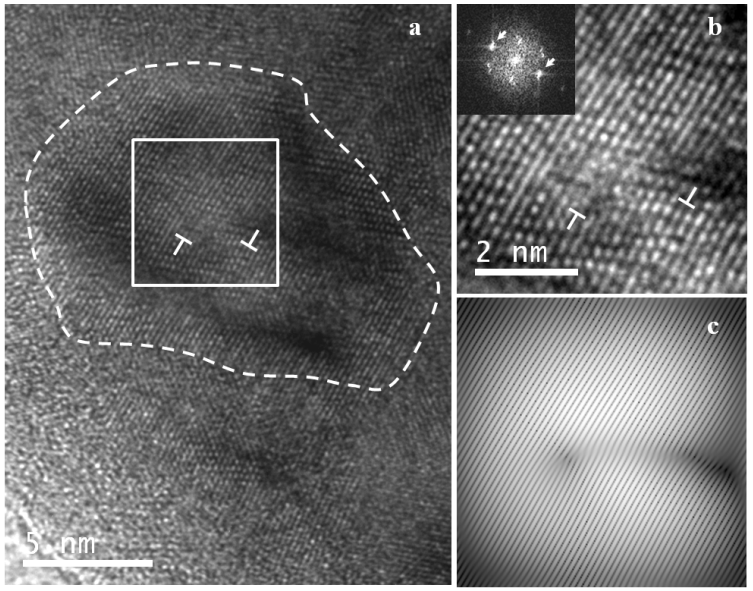

Figure 42: High resolution electron microscopy picture of a ball milled FeMo powder specimen, showing a grain with trapped dislocations (a); a higher magnification picture is shown in (b), with the FFT in the inset; filtered picture, as obtained by inverse FFT to highlight the dislocation, is shown in (c). See text for details.

Again, TEM observations point out the presence of separate domains of about 10 nm size, in agreement with XRD/WPPM. The HRTEM micrograph of Figure 42 focuses on a representative grain, marked by the dashed line, where trapped dislocations are visible (indicated by ⊥). The strong ripple contrast in the image may be taken as an indication that the area was experiencing substantial strain. The dislocation area framed by the white box in Figure 42A is shown at higher magnification in Figure 42B, where the corresponding FFT is included as an inset. The most intense diffraction spots (arrows) indexed in the FFT are compatible with those of the (110) planes of bcc FeMo, whereas weaker spots are compatible with a Fe_3O_4 spinel phase. Such a minority oxide phase (totally absent in the XRD patterns) only appears on the loose

particles of thickness suitable to the electron transmission, mostly present on the surface of the large clusters (see Figure 37) composing the powder. Figure 42C is the corresponding inverse FFT image of the dislocation area, reconstructed using the spatial frequencies of the (110) planes of bcc FeMo. This picture further highlights the trapped dislocations, as well as a distinct dark contrast resulting from the propagation of the strained area during the stress relief. The measured displacement vector at each dislocation site is about $\frac{a}{3}\left[110\right]$, which is compatible with a Burgers vector $b=\frac{a}{2}\left[111\right]$ of a unit edge dislocation in the primary slip system of bcc iron. Dislocations appear in a dipole configuration, with strongly interacting strain fields, probably as a result of tendency to minimize the total energy [89].

The TEM investigation reported so far fully supports the results of the XRD/WPPM analysis. However, owing to the thickness-selectivity of HRTEM experiments, only a few grains can be analysed across the large FeMo clusters (see Figure 37) and additionally, reliable data can only be extracted from grains properly oriented with respect to the electron beam. Therefore, dislocations may be difficult to observe due to unfavourable orientation, and because of screening effects of the metal cluster where domains are embedded in. However, based on the result of extended TEM experiments, presence of dislocations is most likely restricted to a few domains.

This evidence would suggest that strain broadening effects in the XRD line profile could be just partly related to dislocations; additional strain components could arise from the grain boundary, and by interactions among different domains (so-called grain interaction), thus resulting in a mix between type II (intergranular) and type III (intragranular) strains [10][90][91][92][93].

A finer distinction between different strain components is beyond the current capabilities of LPA, so that we can conclude the quoted dislocation density is likely to be just an upper limit to the true value. To the purpose of u sing this material as a reference, and in general, to provide a more reliable result, it is possible to refer to the r.m.s. strain (root mean square strain, or microstrain, $\sqrt{<\varepsilon^2>}$, see Appendix B), the width of the strain distribution in the material [10]. This representation of the strain broadening is more general, and does not commit to a specific source of strain; moreover, the WPPM analysis can easily provide a microstrain trend along any desired crystallographic directions, to highlight the effect of anisotropy.

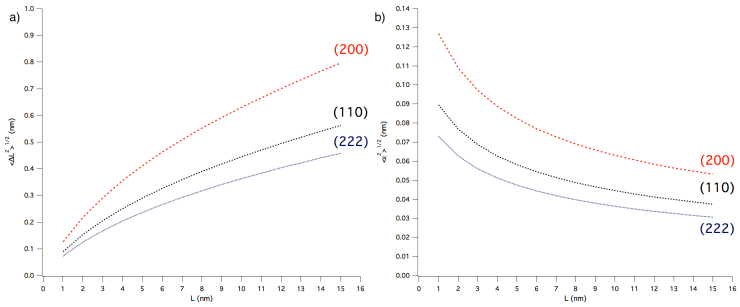

Figure 43: Warren's plot for ball milled FeMo powder. R.m.s. displacement (a) and r.m.s. strain (b) along different crystallographic directions. See text and Appendix B for details.

The microstrain for the ball-milled FeMo powder is shown in Figure 43 along three representative directions; besides microstrain, also the r.m.s. displacement ($\sqrt{<\Delta L^2>}$) is shown, as originally proposed by Warren [87]. As expected, strain is larger along [h00], which is the elastically soft direction of iron. Additional advantages of reporting the strain broadening effect in terms of microstrain include the possibility to directly compare the present results with those provided by other methods (e.g., the Warren-Averbach method [87][88]). Quoting a

microstrain also avoids intrinsic problems with the Krivoglaz-Wilkens theory [83][84][85], as the simultaneous refinement of ρ and R_e is unstable owing to the strong correlation between the two parameters [93].

Even if of no direct or critical importance in the present context (i.e., considering the ball milled FeMo powder as a LPA reference material), the unit cell parameter contributes some useful additional information. Measured value is a_0 = 0.28729(1) nm, well above the unit cell parameter of the pristine material, 0.28703(3) nm [58], which in turn agrees well with the ideal solid solution value for Fe-1.5wt%Mo (0.28706 nm, based on Vegard's law [94][95]).

A larger unit cell parameter is typical of ball-milled metals [58][82], mostly because of the effect of severe plastic deformation, with additional contributions by alloying (solid solution) with materials of the grinding media (Cr and Ni in this case). Very fine crystalline domains increase vacancy and defect solubility [96], leading to volume expansion, which adds to the free volume increase caused by extrinsic dislocations piling up at the grain boundaries [97].

Finally, it is worth nothing that, despite the high level of elastic energy stored in the ball milled material, the FeMo microstructure is quite stable. A recent study demonstrated that the stabilization mechanism is mostly based on the high lattice strain, which locks grain boundaries preventing any evolution of domain size and strain up to ~100 °C [68][98]. Recovery starts above this temperature, supported by a dislocation cross-slip and annealing mechanism, indirectly observed as a steady decrease of the screw dislocations above 100°C. This evidence suggests that an extensively ball milled FeMo powder is stable under common measurement conditions and storage at RT, a rather fundamental feature for a candidate reference material. Stability of the microstructure is paralleled by resistence to oxidation, which besides the action of molybdenum [74] is likely improved by the Cr-Ni

contamination from the grinding vial and balls. Both features were verified in a recent study, where a ball milled FeMo powder has been measured ten years after grinding [78], providing the same size/strain and unit cell parameters within experimental error, and no measurable signals from oxide phases [76][77].

4.5 Conclusions

High energy grinding of an iron-molybdenum alloy powder provides a possible candidate as reference material for diffraction LPA.

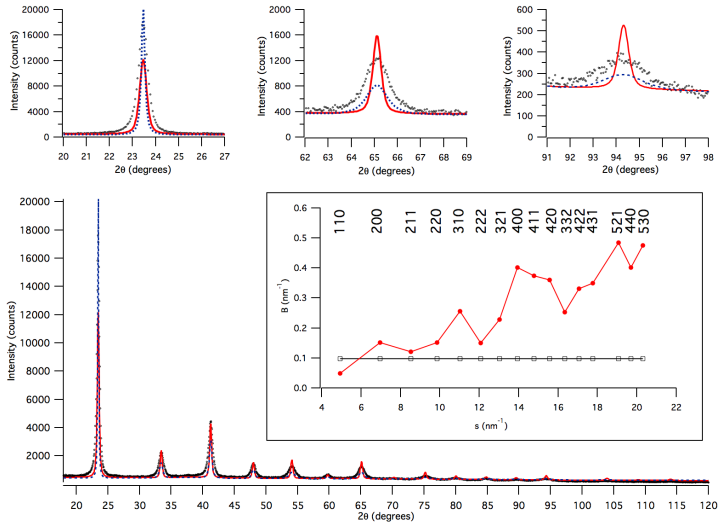

Figure 44: X-ray powder diffraction pattern of the FeMo powder: experimental data (circle), crystalline domain size (red line) and inhomogeneous strain (blue dash) profile components. Pictures above show details from low to high 2θ angle, respectively, (110), (321), and (431) peaks of α-iron. The total model profile is given by the convolution of the two components (see Figure 39). The inset shows the integral breadths for the size (open square) and strain (full circle) components, as a function of s, the scattering vector modulus (aka Williamson-Hall plot).

As shown in Figure 44, *size* and *strain* effects contribute to a comparable extent to the profile broadening, with a characteristic trend showing an

inversion of the contributions: at low 2θ angle (e.g., in the (110) peak profile shown in the inset) the size effect component is broader than the strain component, whereas the opposite is true for growing 2θ (e.g., in the (321) and (431) peaks shown in the insets). This feature combines with other useful properties of the proposed material, including stability in time and low contamination effects, availability by a simple and reproducible process, presence of a single phase, intense diffraction signal with limited peak profile overlapping.

Evidence from other techniques (SEM, TEM, SAXS) confirms the extent of the size broadening effect measured by LPA, arising from a system of equiaxed crystallites (i.e., crystalline domains which can be approximated by a distribution of spherical domains) with little dispersion around a mean size of ≈ 10 nm.

LPA also provides a microstrain value which could be read in terms of strain field from a high density of dislocations (ρ = 4.5 10^{16} m^{-2}) with short effective cut-off radius (R_e = 4.3 nm), equally divided in screw and edge types. Even if the result is within the validity limit of the Krivoglaz-Wilkens theory for the case of strongly interacting dislocations ($R_e\sqrt{\rho}$ ≈ 1), such a high dislocation density would involve the presence of quite many dislocations, about two dislocations per crystalline domain. HRTEM pictures actually show dislocations in the primary slip system of bcc iron, but they are unlikely to be present in each crystalline domains as suggested by LPA. Observed domains, even if frequently appear free of line defects, are surrounded by a complex network of grain boundaries. It is therefore possible that the high inhomogeneous strain stems from more factors, which besides dislocations involve the grain boundary and the grain-grain interaction. This model, frequently envisaged in plastically deformed materials, is referred to as type II (intergranular) plus type III (intragranular) strain. Whatever the strain sources and their relative importance, a description in terms of r.m.s.

strain as a function of L, the Fourier or coherence length seems here the most appropriate one as:

(i) it does not commit to any specific strain model,
(ii) avoids the instability of Wilkens model, caused by the strong correlation between ρ and R_e,
(iii) allows a direct comparison with other Fourier models,
(iv) also representing the strain field anisotropy, as the r.m.s. can be reported along different crystallographic directions.

The present results, therefore, besides supporting the possibility of using this material as a reference for *size* and *strain* broadening using any suitable LPA method, might be the basis of a certification protocol.

Appendix B: Root mean square strain (r.m.s. strain or "microstrain")

The Fourier Transform of the peak profile given by inhomogeneous strain can be written as:

$$A^{D}_{\{hkl\}}\left(L\right)=\exp\left[-2\pi^2 s^2 L^2 <\varepsilon^2_{\{hkl\}}\left(L\right)>\right]=\exp\left[-2\pi^2 s^2 <\Delta L^2_{\{hkl\}}\left(L\right)>\right] \qquad \text{(B1)}$$

where $s=\frac{2\sin\theta}{\lambda}$ is the modulus of the scattering vector *s*, and *L* is the Fourier length, i.e., the distance, projected along *s*, between couples of scatterers in the crystalline domain, and $<\varepsilon^2_{\{hkl\}}\left(L\right)>$ is the variance of the strain distribution [62]. This approach is quite general, even if we limit it here to cubic materials, so to refer to the {*hkl*} family of atomic planes or equivalently to the <*hkl*> family of directions. Eq. (B1) also introduces the mean square displacement, $<\Delta L^2_{\{hkl\}}\left(L\right)>$, used in Warren's plot as $\sqrt{<\Delta L^2_{\{hkl\}}\left(L\right)>}$ vs. *L*. (alternative notations include: $Z^2_L=L^2\varepsilon^2_L=<\Delta L^2\left(L\right)>=\overline{\Delta L^2}$ [87][88][99]).

The general expression Eq. (B1) can be used in the Wilkens-Krivoglaz theory of diffraction line broadening caused by dislocations [84]:

$$<\varepsilon^2_{\{hkl\}}\left(L\right)>=\frac{\rho\bar{C}_{\{hkl\}}b^2}{4\pi}f^*\left(\frac{L}{R_e}\right) \qquad \text{(B2)}$$

with f^*, the so-called Wilkens's function (a slowly varying function of $\frac{L}{R_e}$ [84]), and $\bar{C}_{\{hkl\}}$, the average contrast factor, which for cubic materials can be written as:

$$\bar{C}_{\{hkl\}} = A + B\,H = A + B\,\frac{h^2k^2 + k^2l^2 + l^2h^2}{\left(h^2 + k^2 + l^2\right)^2} \tag{B3}$$

A and *B* can be calculated for different dislocation types, slip systems and elastic media [100]. In a system of edge and screw dislocations it is convenient to introduce the fraction of edge dislocation, f_E, so that *A* and *B* can be written as linear combinations of values for pure edge and screw types:

$$A = A_E f_E + A_S\left(1 - f_E\right) \tag{B4a}$$

$$B = B_E f_E + B_S\left(1 - f_E\right) \tag{B4b}$$

For dislocations in the primary slip system of α-iron, 1/2<111>{110}, A_E = 0.265280; B_E = -0.355950; A_S = 0.307288; B_S = -0.819979 [78]. The Burgers vector modulus, $b = \frac{\sqrt{3}a_0}{2}$, is about 0.2485 nm for α-iron.

Chapter 5

Understanding the Instrumental Profile: a realistic ray-tracing approach

Part of this chapter has been published in:

Luca Rebuffi, Paolo Scardi, Manuel Sánchez del Río

"Design and management of a powder diffraction beamline for Line Profile Analysis: a realistic ray-tracing approach",
accepted for publication by Powder Diffraction (2015)

Luca Rebuffi, Paolo Scardi

"Calculation of the instrumental profile function for a powder diffraction beamline used in nanocrystalline material research",
Proc. SPIE 9209 (2014), Advances in Computational Methods for X-Ray Optics III, 92090J, doi:10.1117/12.2063745

Manuel Sánchez del Río, Luca Rebuffi, Janez Demšar, Niccolò Canestrari, Oleg Chubar

"A proposal for an Open Source graphical environment for simulating X-ray optics",
Proc. SPIE 9209 (2014), Advances in Computational Methods for X-Ray Optics III, 92090X, doi:10.1117/12. 2061834

5.1 Abstract

We combine the SHADOW ray-tracing optical simulation with the calculation of powder diffraction profile from standard materials, into a high-level workflow environment based on the ORANGE software. Algorithms are developed to reproduce optical elements in a realistic form, so to evaluate the effects of aberrations, with the final purpose of reconstructing the IPF of the beamline, with the possibility of investigating the role of each separate element.
The results of this work can be of interest to most beamlines as a powerful tool for the design of setups of existing as well as new beamlines.

5.2 A Modern Ray-Tracing Tool

After choosing SHADOW [20][21][22][23] as the ray-tracing engine (see Chapter 1), the need of a powerful graphic user interface engine raised quite naturally on the perspective to develop new features for simulating the IPF of XRPD beamline.
ORANGE is a comprehensive, component-based framework for both experienced data mining and machine learning users and developers, and for those just entering the field that can interface ORANGE through short Python [101] scripts or visually design data mining applications using ORANGE Canvas and widgets [102].

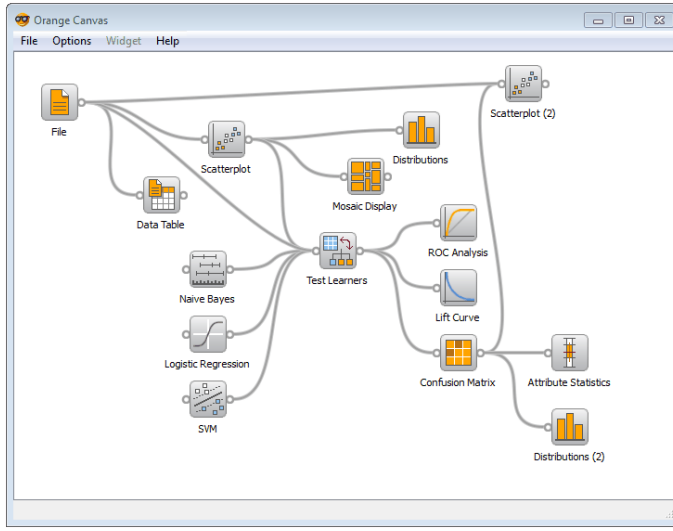

Figure 45: Appearance of an ORANGE schema (courtesy of Prof. Janez Demšar, University of Ljubljana)

Active objects, i.e. containing data and procedures, appear as widgets in a desktop, exchanging a data flux represented by connecting wires between widgets (see Figure 45).

By calling SHADOW via its Python API (see Figure 46), it was possible to create SHADOW objects representing the different optical elements and photon sources as widgets available to the user, exchanging a SHADOW object representing the photon beam as the I/O data passing through the wires.

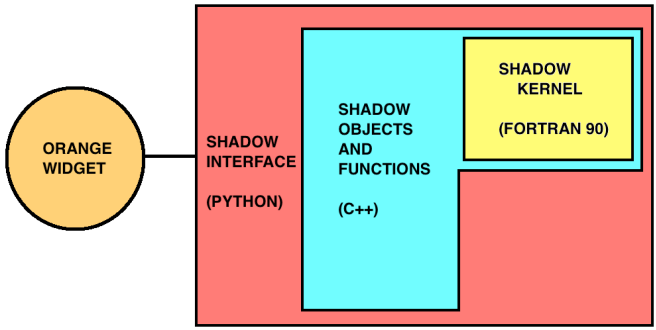

Figure 46: ORANGE-SHADOW integration: architecture schema

The widget-oriented aspect of ORANGE, drive us to fill the widget toolbox with dedicated widgets for every possible optical element, graphical and calculation tool, originally present in SHADOW. By interacting with the toolbox the user can populate the workspace area with optical elements, drawing a beamline layout with a CAD fashioned visual aspect, as visible in Figure 47.

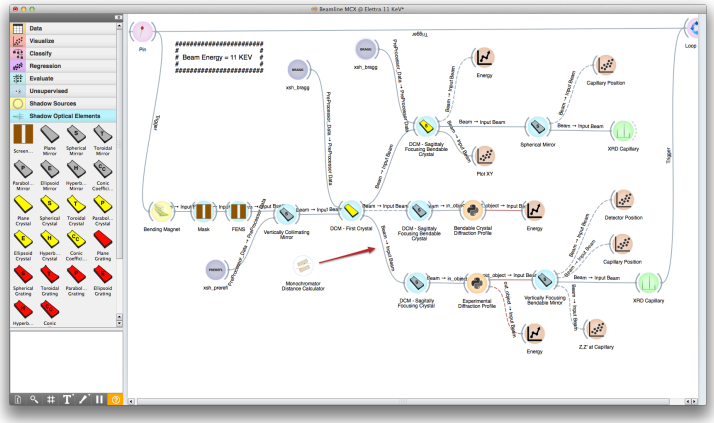

Figure 47: Ray-tracing simulation of a powder diffraction experiment (MCX beamline at Elettra-Sincrotrone Trieste): layout appearance in the user interface

An example of an optical element widget is shown in Figure 48.

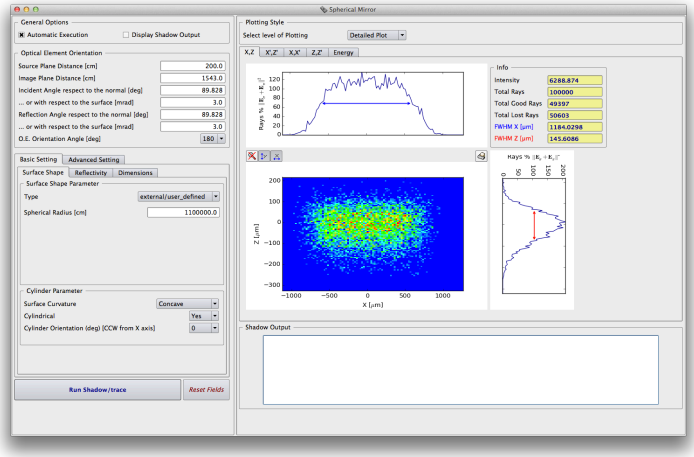

Figure 48: Appearance of the input/output form available for an optical element widget

5.3 A Realistic Ray-Tracing Approach to XRPD

Together with the pristine functionalities of SHADOW, a special widget representing XRPD samples (in capillary holder) simulating the interaction of the photons with matter was developed, with the target of analysing and predicting instrumental effects on experimental profiles.

The incident beam is obtained by a SHADOW ray-tracing simulation of the beamline, together with its capability of adding realistic features to the optical elements, like reflectivity (both for mirrors and crystals) and slope error, by using either simulated profiles or, when available, experimental data.

An example of intensity distribution within the cross section at the sample position is shown in Figure 49, comparing the results of purely ideal elements and with the realistic features added.

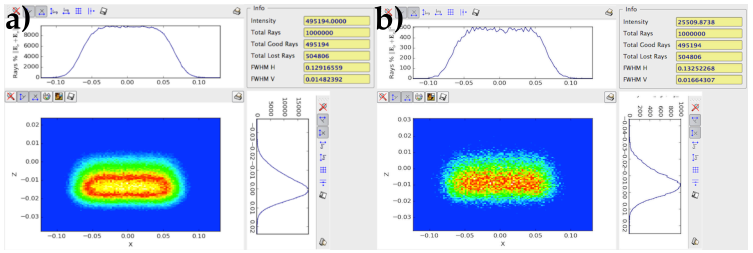

Figure 49: Intensity distribution of the SHADOW incident beam within the cross section at the sample position, with different simulation setups: (a) purely ideal elements, (b) realistic features added

The main effect of the incident beam divergence and energy distributions, coming from the optical elements and source characteristics, on a powder diffraction pattern is a peak broadening, showing a dependence on the 2θ angle, that has been mathematically described in [11][12], and it is usually represented and parameterized by the Caglioti's equation [44][45] for FWHM of the instrumental peak profiles, here represented as pseudo-Voigt curves (eq. (3), see Chapter 2).

The three parameters, *U, V, W*, are obtained by analysing the diffraction pattern from a sample of NIST SRM 660 LaB_6 [24][25], already described in Chapter 2. A similar characterization can also be made with Silicon [60].

The realistic reproduction of the IPF of a XRPD synchrotron beamline through the SHADOW ray-tracing algorithm starts from the simulation of the interaction of the SHADOW photon beam with a capillary filled by such a SRM, generating a diffracted photon beam and prosecuting the ray-tracing onto the optical elements lying on the path from sample to detector.

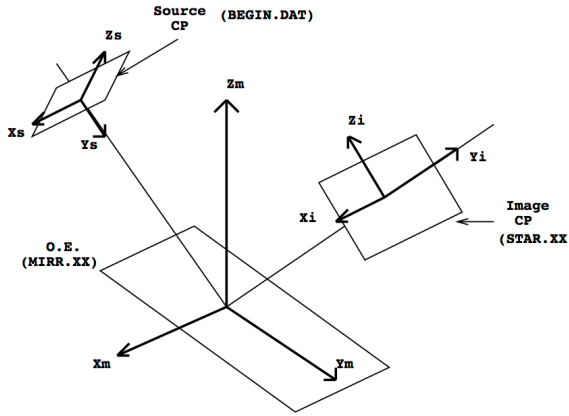

Figure 50: SHADOW axis systems: the ideal optical axes for the capillary system are X_m, Y_m and Z_m. In particular, Y_m represent the ideal direction of propagation of the photon beam.

With reference to Figure 50, for each ray incident on the capillary a random point is generated along the path between the entry and the exit points, then the diffracted beam is generated rotating the ray wave vector by two times the Bragg angle calculated with the ray energy. In order to take into account the ray spatial attributes (i.e. its vertical and horizontal divergence respect to the ideal optical axis, see Figure 50) the rotation axis versor $\vec{X}_{ray}^{rot}$ has been calculated according to the following formulas:

$$\vec{Z}_{ray}^{rot} = \left(\vec{X}_m \times \frac{\vec{k}}{|\vec{k}|} \right) \tag{6}$$

$$\vec{X}_{ray}^{rot} = \frac{\vec{k}}{|\vec{k}|} \times \vec{Z}_{ray}^{rot} \tag{7}$$

Where $\vec{X}_m$ is the versor representing the SHADOW X axis of the capillary system.

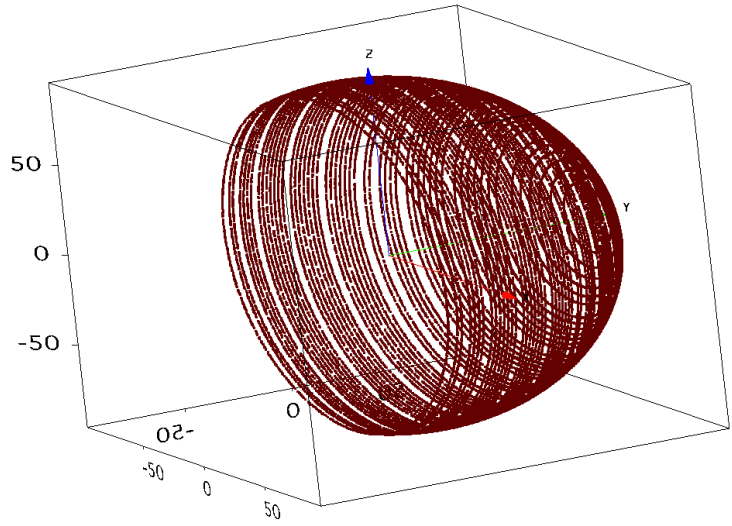

Figure 51: Intersection points of the generated diffracted rays of a LaB_6 sample at 11 keV with a sphere centered on the capillary axis system. Powder diffraction (Debye) rings are clearly visible.

In order to reproduce the diffraction rings of a powder, the diffracted ray is then rotated around the versor of its wave vector $\frac{\vec{k}}{|\vec{k}|}$, by a random angle within a range determined the successive angular acceptance of the optical system driving the signal to the detector, preventing from losing rays. Figure 51 shows the intersection points of the diffracted rays with a sphere centered in the capillary axis system, and calculating the final random rotation around the wave vector of the diffracted rays within 360 degrees.

Every diffraction peak is normalized to the most intense one, calculated from the structure factor square modulus and the multiplicity of the reflection.

The experimental diffraction pattern is collected by a 2θ angle stepped scan of the diffracted signal, which is simulated via a repeated SHADOW

ray-tracing of the detector optical system, rotated step by step around the capillary system X axis.

Three possible optical systems are available: a couple of collimating slits between the sample and the detector, an analyser crystal with an entrance slit, or an area detector.

The final pattern can be normalized with the Lorentz-Polarization and Thermal factors, using the following expressions [103][104][105][106]:

$$LP\left(2\theta\right)=\begin{cases}\dfrac{1}{\sin\theta\sin\theta_{bragg}}\dfrac{\left(1+Q\right)+\left(1-Q\right)\cos^2 2\theta\cos^2 2\theta_{mon}}{1+\cos^2 2\theta_{mon}} & \text{system of slits}\\ \dfrac{1}{\sin\theta\sin\theta_{bragg}}\dfrac{1+\cos^2 2\theta\cos^2 2\theta_{ana}}{2} & \text{analyzer crystal}\end{cases} \tag{8}$$

$$T\left(2\theta\right)=\exp\left[-2B\left(\frac{\sin\theta}{\lambda}\right)^2\right] \tag{9}$$

where θ_{bragg} is the nominal Bragg angle of the reflection, $Q=\dfrac{I_h-I_v}{I_h+I_v}$ is the degree of polarization (around 0.95 for the synchrotron radiation, I_h e I_v are, respectively, the intensity of the horizontally and vertically polarized radiation parts), θ_{mon} is the angle between the incident beam and the first monochromator crystal, B is the Debye-Waller coefficient (in the present work, for simplicity, we consider an average B value).

A complete ray-tracing simulation representing a powder diffraction experiment is shown in Figure 52. The experiment for characterizing the IPF used a 0.8 mm Kapton® capillary filled by NIST 660b LaB_6 [24][25], and a photon beam energy of 30 keV.

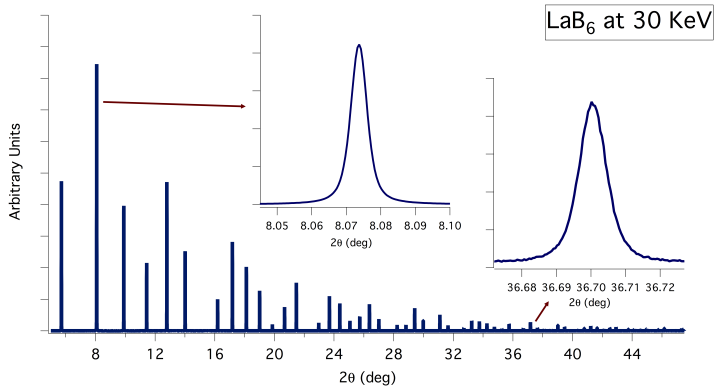

Figure 52: LaB_6 simulated diffraction pattern, from a 0.8 mm capillary at 30 keV photon energy. Insets show details of the simulated peaks: the progressive increment of the instrumental broadening is clearly visible

The simulation takes into account several sources of positional aberrations:

(i) displacement of the capillary with respect to the goniometric centre,
(ii) misalignments of the θ and 2θ goniometers: different position of the goniometric centres and different axis orientation,
(iii) displacement of the slits with respect to the ideal optical path,
(iv) simple model of capillary wobbling, corresponding to a percent increase in diameter.

The software allows a background to be added to the generated diffraction pattern, selecting and/or combining three different functions: constant value, Chebyshev polynomial of the first kind up to 6^{th} degree and exponential decay. A random noise of adjustable intensity is generated around the selected background curve.

5.3.1.1 Absorption Calculation and Effects

Finally, the simulation can take into account the absorption of the material, reducing the initial intensity I_0 of each incoming and diffracted ray according to the Beer-Lambert law:

$$I(\lambda, x) = I_0 \exp\left[-\mu(\lambda)\rho_{eff} x\right] \tag{10}$$

where $\mu(\lambda)$ is the linear absorption coefficient at the photon wavelength λ, calculated with the *xraylib* API [107], providing a total photon-matter interaction cross section with the contribution of Rayleigh elastic scattering, Compton inelastic scattering and photoionization, ρ_{eff} is the material density multiplied by the packing factor of the sample into the capillary (typically around 0.6 for pure materials), and x the path of the ray inside the capillary.

The absorption effect is also considered calculating the source points of the diffracted rays with a random generator based on an exponential probability distribution according to the transmitted intensity law (eq. (10), rather than the more common default flat distribution):

$$P(\lambda, x) = K \exp\left[-\mu(\lambda)\rho_{eff} x\right] \tag{11}$$

where K is a normalization factor.

This choice is necessary because a flat distribution of source points cannot correctly account for absorption in the ray-racing procedure.

A suitable procedure, when generating a diffracted beam, is to introduce a probability of interaction with the material, responsible for the intensity drop along the beam path. An example of the generated source points including X-ray absorption is shown in Figure 53: as clearly visible from the spatial distribution of the source points, the main effect of absorption is an apparent capillary displacement.

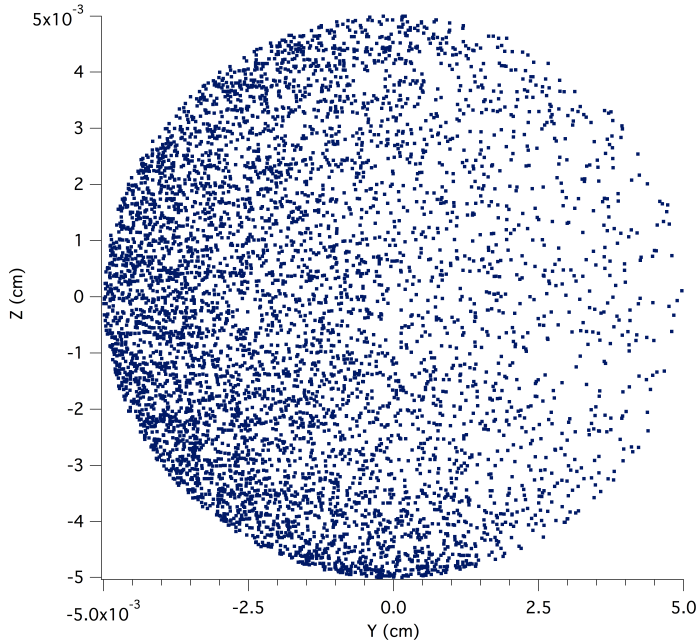

Figure 53: Generated source points of the diffracted beam, on a 0.1 mm diameter capillary, with the absorption calculation activated. The ZY plane section refers to the SHADOW axis system.

Figure 54 shows the result of the absorption calculation in terms of peak intensities of the diffraction profile; the apparently smaller Debye-Waller coefficient is clearly visible and reproduced.

The absorption from the capillary walls has been taken into account and treated as well as the absorption of the sample material, with the possibility of a selection of materials: quartz glass, borosilicate glass, and Kapton®.

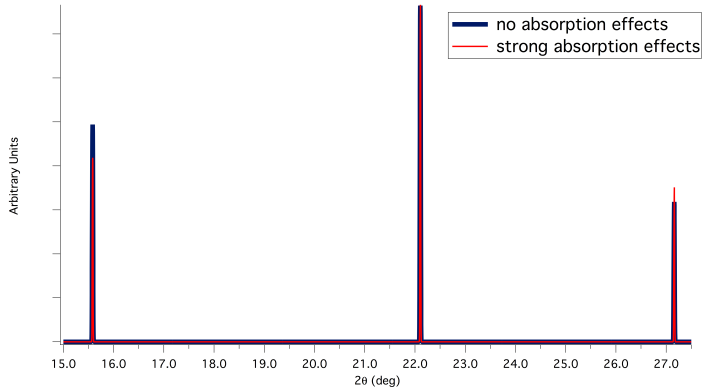

Figure 54: Comparison between simulated diffraction profiles of LaB_6 at 11 keV photon energy, with and without the absorption calculation activated. The patterns are normalized respect to the central peak

An important effect of the absorption can be noticed in the peak shape, as visible in Figure 55: with increasing values of μR [81] (product of the linear absorption coefficient and the capillary Radius), a progressive asymmetric shape appears, reducing the peak broadening, together with a peak shift. Considering that the peak position is crucial in determining the cell parameters of the material and the instrumental broadening and shape affects the calculation of size and strain effects, we can understand how important is to maintain the absorption under control (at least $\mu R < 1$), in order to maximize the precision and affordability of LPA. The higher the absorption is, not only more clearly the well-known effects on relative intensity appear, but also other aberrations critical for LPA become important.

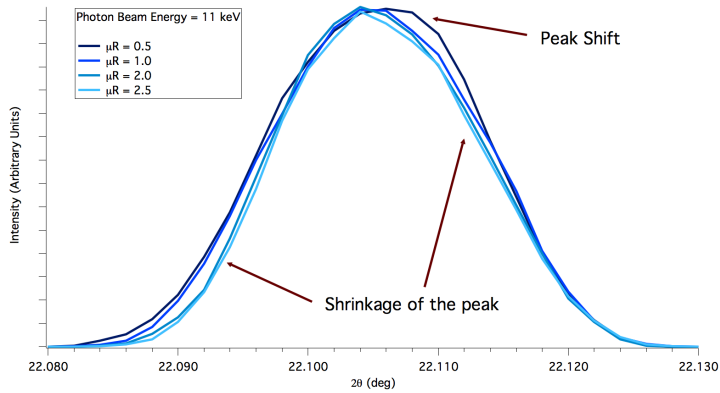

Figure 55: Effect of progressive absorption values on the LaB_6 (1,1,0) peak of at 11 keV: peak shape and position.

5.4 Analysis of single contributions to the instrumental profile via ray-tracing

Comparison between the simulation and experimental LaB_6 XRD profiles from real beamlines are discussed in the following sections, in order to understand the most critical contributions to the instrumental profile and identify the hardware components they belong to.

5.4.1 MCX at Elettra-Sincrotrone Trieste

First indications were obtained from a complete simulation of the MCX beamline, the optical layout of which is described in detail in Chapter 2.
The monochromator shows interesting features regarding the emerging energy bandwidth, which can be investigated thanks to the SHADOW capabilities.
The experiments for characterizing the IPF were made using a 0.1 mm capillary filled with NIST SRM 660a LaB_6 [25] and photon beam energy of 11 keV, 15 keV and 20 keV.

The first step was a careful optimization of the optical setup, in order to let the simulation the most closely reproduce the real conditions of the experiment (see Chapter 2):

(i) mirrors contain a generated slope error, with an average value equal to measured ones: 0.1 μrad for the first vertically collimating mirror and 0.12 μrad for the second vertically focusing mirror (courtesy of Dr. Andrea Lausi, MCX Beamline responsible). The tool, contained in the SHADOW distribution (Waviness) creates a random error surface through a method described in [108],
(ii) both mirrors contain the Platinum reflectivity profile (Reflectivity vs Incidence Angle vs Energy) generated by a tool present in SHADOW (PreRefl),
(iii) the diffraction profiles of DCM crystals were generated as perfect crystal ones, again with a SHADOW tool (Bragg). The DCM second crystal can also use diffraction profiles reconstructed from the experimental rocking curves, as discussed in Chapter 2,
(iv) The second crystal of the DCM is simulated as perfectly cylindrical with spherical curvature in the sagittal plane.
(v) Several sets of slits are present along the beamline to properly shape the beam and limit the angular divergence.

The capillary is filled with a packing factor of 0.55, calculated by a direct measurement of transmittance at the beamline in order to take into account the same value of the absorption, as measured during the measurement of the SRM profile.
In order to be able to fully drive the parameters influencing the beam properties and analyse every degree of freedom separately, the photon source is simulated as purely geometrical, with Gaussian spatial shape, uniform angular divergence and uniform energy emission into a bandwidth. The final realistic simulation is instead obtained by using a Bending Magnet simulator.

5.4.1.1 *Instrumental profile dependence of photon source spatial dimension*

The dependence on the source spatial dimension has been studied with the following setup of the photon source:

(i) purely monochromatic source (1 emission line),
(ii) Gaussian vertical and spatial shape parameterized by their vertical and horizontal σ,
(iii) purely parallel beam (no vertical or horizontal angular divergence),
(iv) DCM Crystals are simulated as perfect crystals,
(v) simulations were carried at 11, 15 and 20 keV.

In Figure 56 it is possible to see an example of such a generated source.

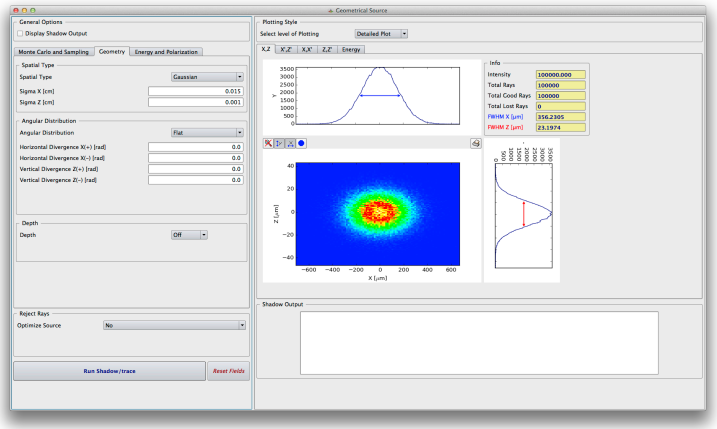

Figure 56: Example of the purely geometrical photon source widget: the Gaussian spatial distribution is visible.

The result visible in Figure 57 is as expected: no dependence of the instrumental broadening on the source dimension, and its width is substantially determined by the diameter of the capillary. The

dimension of the diffracted rays “source” seen by the detector is, in any case, dominated by Y extent of the projection of the beam intersection with the capillary in the XY plane (see Figure 50), which is the same for every vertical (and horizontal) dimension of the source.

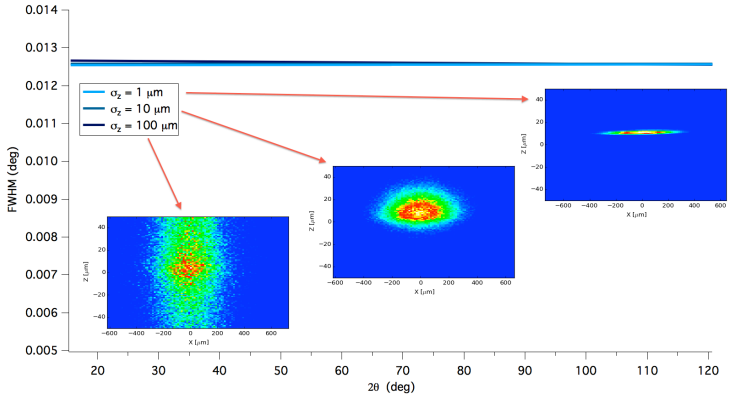

Figure 57: Effect of source vertical dimension on the instrumental broadening, insets represent the XZ projection of the beam (spot) at the quote of origin of the capillary axis system.

Similar results are obtained varying the horizontal dimension of the source, confirming that the main factor to produce a minimum spot size at the detector (i.e. the minimum angular broadening, in absence of any source of aberrations) is the diameter of the capillary.

From a purely geometrical optics point of view, the diffraction from the capillary acts as a mirror at every Bragg angle. Without angular divergence and energy bandwidth no dependence is produced in the instrumental broadening on the detector 2θ angle.

Repetition of the simulations at 15 and 20 keV led to identical conclusions.

5.4.1.2 *Instrumental profile dependence of photon source angular divergence*

The dependence on the source angular divergence has been studied with a setup of the photon source as follow:

(i) Purely monochromatic source (1 emission line),
(ii) pointlike source (no spatial distribution),
(iii) uniform angular divergence distribution parameterized by their vertical and horizontal σ,
(iv) DCM Crystals are simulated as perfect crystals,
(v) simulations were carried at 11, 15 and 20 keV.

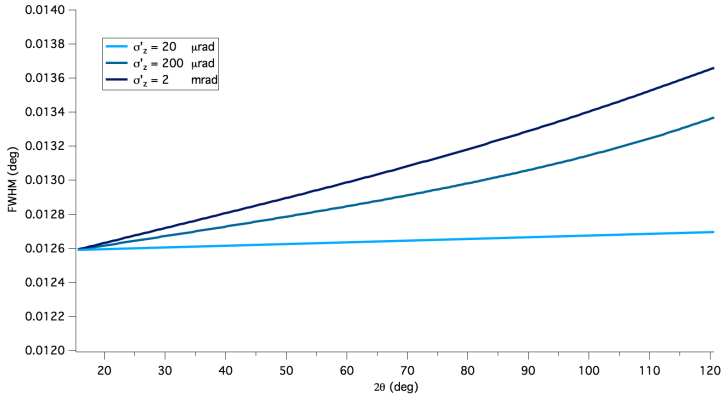

Figure 58: Effect of source vertical angular divergence on the instrumental broadening.

Figure 58 shows the result of simulations carried out with three vertical angular divergence values (20 µrad, 200 µrad and 2 mrad) at 11 keV, keeping the horizontal divergence constant to 2 mrad (a realistic value for a beam coming from the front-end of a beamline with a bending magnet source at Elettra): just a weak dependence is visible.

No significant dependence on the horizontal divergence is instead observed, and similar results were obtained at 15 and 20 keV.

5.4.1.3 *Instrumental profile dependence of beamline energy bandwidth*

The dependence on the energy bandwidth has been studied with a setup of the photon source as follow:

(i) Uniform energy emission into a specified bandwidth,
(ii) purely parallel beam (no vertical or horizontal angular divergence),
(iii) pointlike source (no spatial distribution),
(iv) DCM Crystals are simulated with a very large bandwidth (10 eV) in order let the source drive the bandwidth,
(v) simulations were carried at 11, 15 and 20 keV.

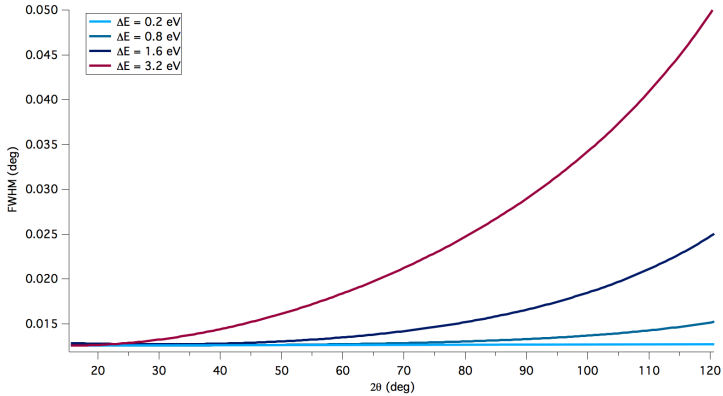

Figure 59: Effect of energy bandwidth on the instrumental broadening at 11 keV.

Figure 59 shows the result of simulations carried out with four energy bandwidth values (0.2 eV, 0.8 eV, 1.6 eV and 3.2 eV) at 11 keV. It can be seen how stronger is the bandwidth dependence on the energy distribution with respect to the spatial distribution. Similar results were obtained at 15 keV and 20 keV.

5.4.1.4 Combined effects: comparison of the simulation with the experimental data

In order to compare the calculated IPF with that given by the experimental LaB_6 diffraction pattern, simulations were performed with the following setup:

(i) Uniform energy emission into a bandwidth source bigger than the theoretical DCM energy resolution,
(ii) Gaussian vertical and spatial shape parameterized by their vertical and horizontal σ,
(iii) uniform angular divergence distribution parameterized by their vertical and horizontal σ,
(iv) DCM Crystals are simulated as perfect crystals,
(v) simulations were carried out at 11, 15 and 20 keV.

The simulation was carried out to reproduce a source similar to the real one, as reported in the Elettra-Sincrotrone Trieste web site [26], and summarized in the following table:

Parameter	Value
σ_x	357 µm
σ_z	114 µm
σ'_x	2.2 mrad
σ'_z	200 µrad
ΔE	10 eV at 11 keV 20 eV at 15 keV 40 eV at 20 keV

In Figure 60 it is possible to see the energy bandwidth emerging from the DCM at 11 keV, equal to 1.4 eV, while Figure 61 and Figure 62 show the spatial distribution and angular divergence of the beam at the quote of the capillary axis system origin, respectively.

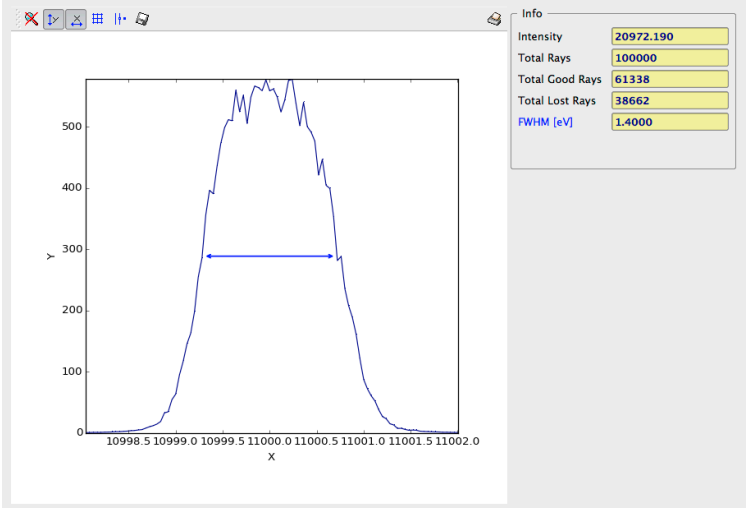

Figure 60: Simulated energy bandwidth emerging from the DCM, at 11 keV.

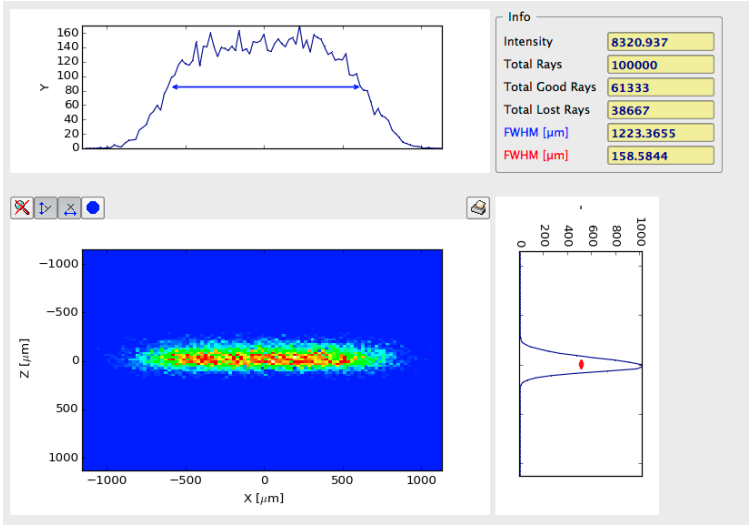

Figure 61: Simulated spatial distribution (spot) of the photon beam at the capillary axis system origin quote, at 11 keV.

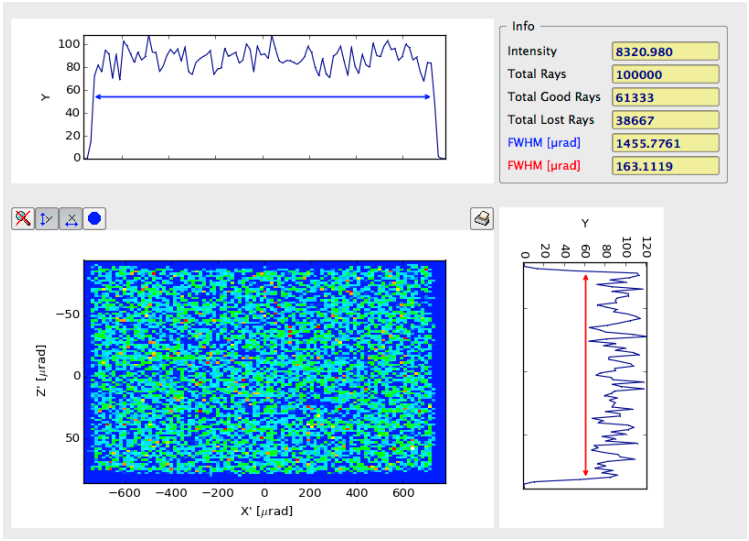

Figure 62: Simulated angular divergence of the photon beam at the capillary axis system origin quote, at 11 keV.

The result at the 3 different energies shows evident discrepancies with respect to the experimental IPF, mostly at high 2θ angle. This result suggests that the actual energy distribution at the sample might be different, especially the bandwidth, being this parameter the most critical one (see paragraph 5.4.1.3).

In Chapter 2 we showed how different were the experimental rocking curves of the second DCM crystal from the theoretical one, and the next step is to introduce into the simulation both a bending magnet source, in order to simulate the source with a synchrotron radiation physical model, and the reconstructed second crystal diffraction profiles.

An important remark is that the simulated patterns follow the observed experimental behaviour of the DCM, showing the effects of a bigger bandwidth for 11 and 15 keV, with a stronger discrepancy for 11 keV, while a significantly smaller bandwidth effect appears at 20 keV.

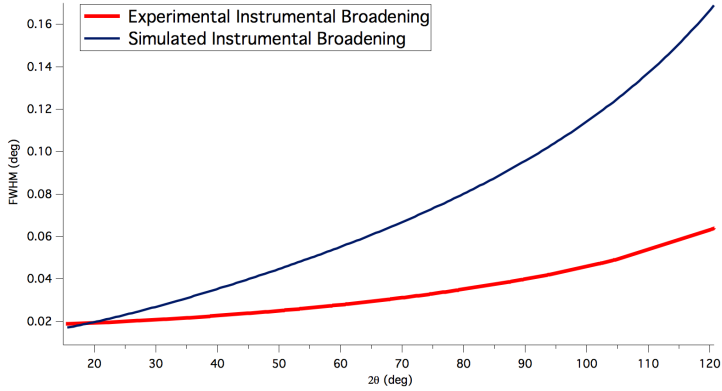

Figure 63: Comparison between experimental instrumental peak broadening at 11 KeV photon energy and the simulated one, with theoretical diffraction profiles for the DCM crystals.

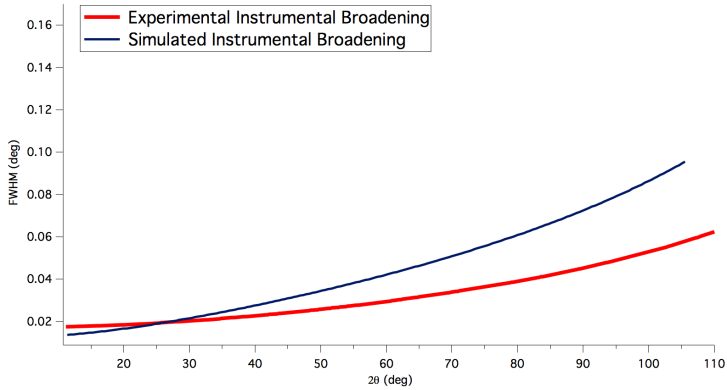

Figure 64: Comparison between experimental instrumental peak broadening at 15 KeV photon energy and the simulated one, with theoretical diffraction profiles for the DCM crystals.

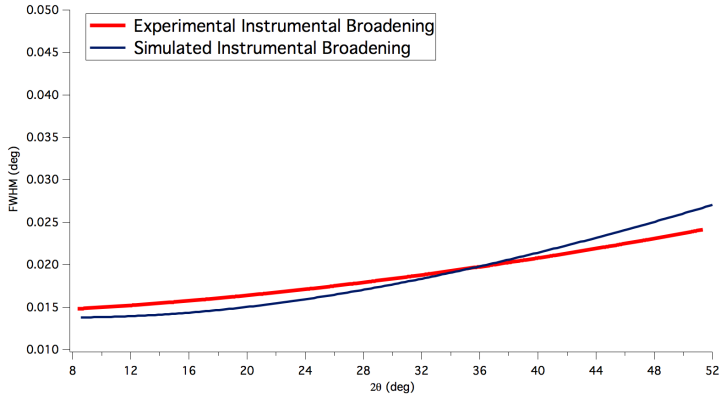

Figure 65: Comparison between experimental instrumental peak broadening at 20 KeV photon energy and the simulated one, with theoretical diffraction profiles for the DCM crystals.

5.4.1.5 Realistic simulation: Bending magnet source and experimental DCM 2nd crystal diffraction profile

The final step of this study was to perform the most realistic simulation possible within the capabilities of the new SHADOW/ORANGE based tool.

The first realistic feature is to replace the geometric source with a simulation of a bending magnet source, with the characteristics reported in the Elettra-Sincrotrone Trieste website [26], even if no big effects are expected considering the weak dependence of the instrumental profile on the attributes of the source. Moreover, the simulated geometric source used in the previous study produced a beam with properties similar to that from a bending magnet.

The first DCM crystal, thanks to negligible thermal effects, can be realistically simulated as a perfect crystal within a good approximation.

For the second DCM crystal it was possible to calculate the diffracted energy profile, using the diffraction profiles reconstructed from the experimental rocking curves, calculating the reflectivity for every ray, according to its incidence angle on the optical element surface and its energy (thanks to an ORANGE special widget for post-elaborating the data exchanged between widgets through a python script).

In Figure 66 and Figure 67 it is possible to see the differences in the energy distribution of the photon beam hitting the capillary obtained by a simulation with a theoretical diffraction profiles and with the reconstructed ones, at 11 keV (central energy).

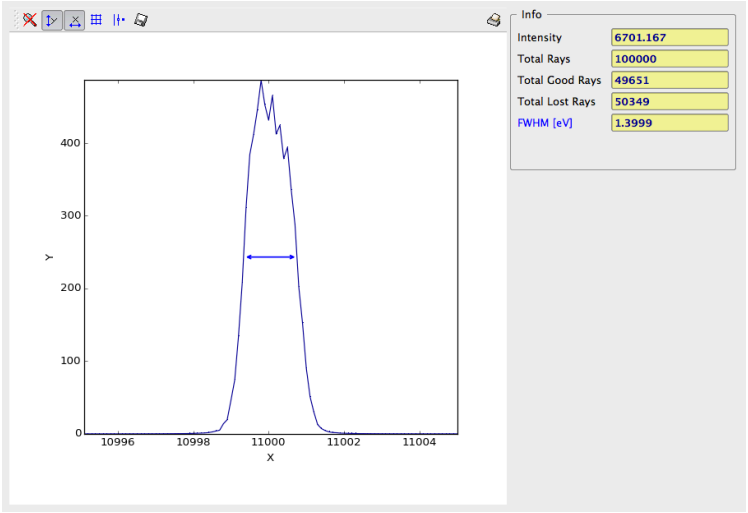

Figure 66: Energy distribution of the simulated photon beam hitting the sample, obtained with theoretical diffraction profiles, at 11 keV (central energy): bandwidth is 1.4 eV.

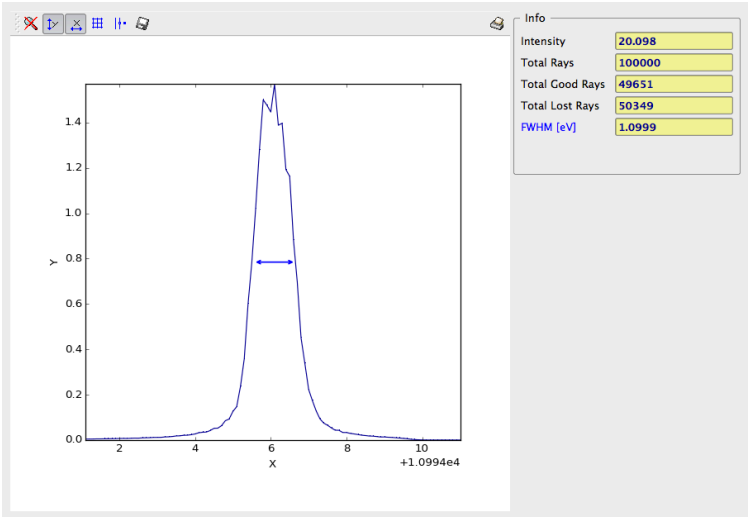

Figure 67: Energy distribution of the simulated photon beam hitting the sample, obtained with reconstructed diffraction profiles, at 11 keV (central energy): bandwidth is 1.1 eV.

The effects of this operation are visible in Figure 68, Figure 69 and Figure 70, where it is possible to see the correction of the simulated experimental broadening obtained at 11, 15, and 20 keV, respectively.

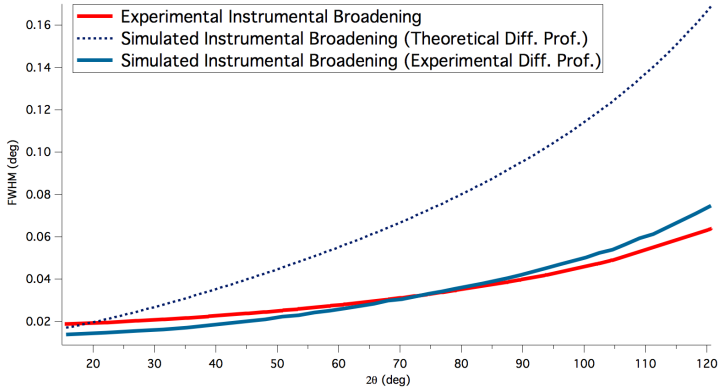

Figure 68: Comparison between experimental instrumental peak broadening at 11 KeV photon energy and the simulated one, with theoretical diffraction profiles for the DCM crystals (dotted blue line) and with reconstructed diffraction profiles (light blue straight line).

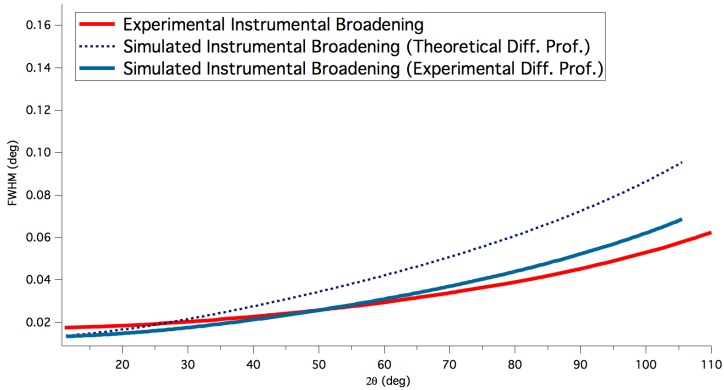

Figure 69: Comparison between experimental instrumental peak broadening at 15 KeV photon energy and the simulated one, with theoretical diffraction profiles for the DCM crystals (dotted blue line) and with reconstructed diffraction profiles (light blue straight line).

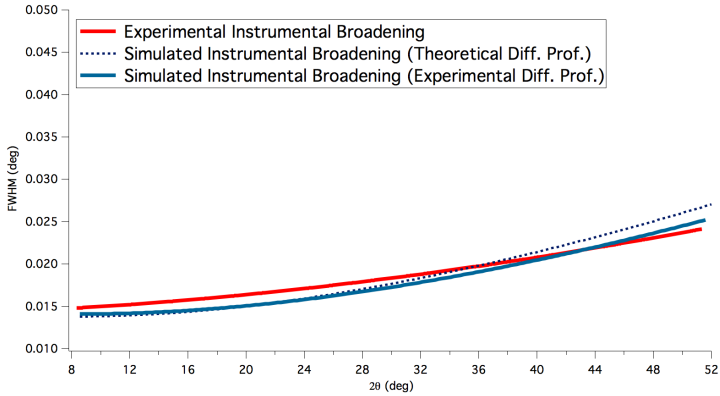

Figure 70: Comparison between experimental instrumental peak broadening at 20 KeV photon energy and the simulated one, with theoretical diffraction profiles for the DCM crystals (dotted blue line) and with reconstructed diffraction profiles (light blue straight line).

Figure 71 shows the comparison between simulated main peak of LaB_6 profile (reflection (110)) and the experimental one at 11 keV: even if the peak width results are slightly underestimated, it is important to observe the correct reproduction of the absorption effects, noting its fingerprint with the same asymmetric shape of both profiles (see paragraph 5.3.1.1). Figure 72 and Figure 73 show the same comparison at 15 keV and 20 keV, respectively, again with a good agreement.

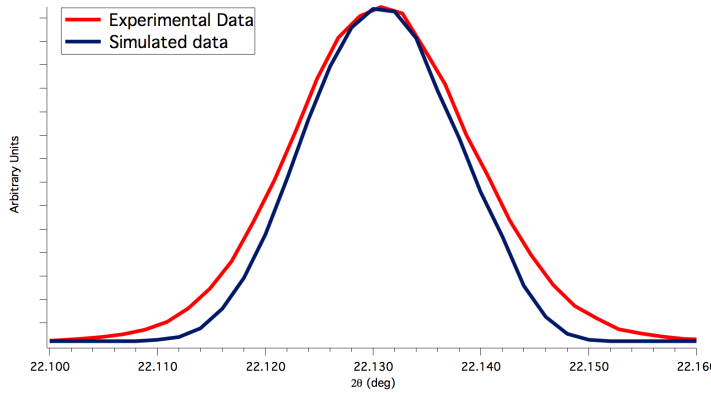

Figure 71: Comparison between experimental LaB_6 (1,1,0) peak at 11 keV photon energy and the simulated one.

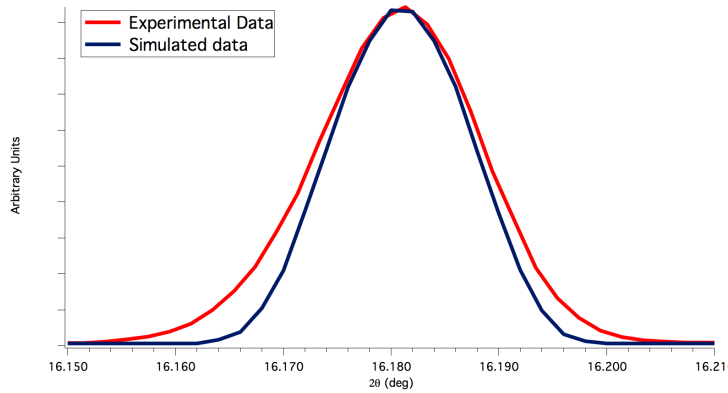

Figure 72: Comparison between experimental LaB_6 (1,1,0) peak at 15 keV photon energy and the simulated one.

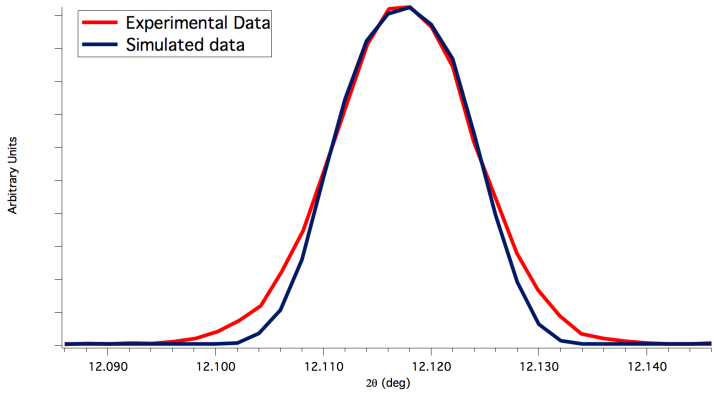

Figure 73: Comparison between experimental LaB_6 (1,1,0) peak at 20 keV photon energy and the simulated one.

A further interesting result is provided by the agreement between the experimental relative intensities and the simulated ones, a clear indication that the level of absorption is correctly simulated, as shown in Figure 74, for the 11 keV simulation.

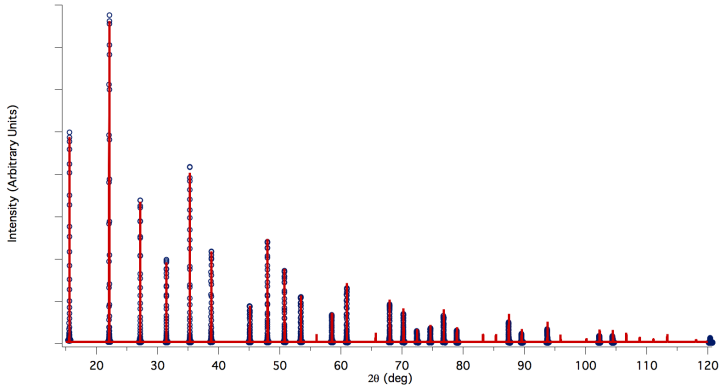

Figure 74: Comparison between experimental diffraction profile at 11 keV photon energy and the simulated one

5.4.1.6 *LPA of FeMo diffraction profiles at 15 keV with simulated IPF*

In order to understand the quality of this simulation with all the realistic features progressively introduced, the LPA made on FeMo samples and discussed in Chapter 4 was repeated with the simulated instrumental broadening. The results of WPPM are summarized in the following table:

	Parameter	WPPM with experimental IPF	WPPM with simulated IPF
Size	$<D>$	9.3(8) nm	9.4(8) nm
	s.d.	5.9(9) nm	5.7(9) nm
	$<D>_S$	10.2(9) nm	10.3(9) nm
	$<D>_V$	10.9(9) nm	11.0(9) nm
Strain	ρ	4.5(4) 10^{16} m^{-2}	4.7(3) 10^{16} m^{-2}
	R_e	4.3(4) nm	4.1(4) nm
	f_E	0.54(3)	0.54(3)

In Figure 75 it is possible to see the WPPM fit with the simulated IPF, observing that even the global accuracy has been correctly reproduced.

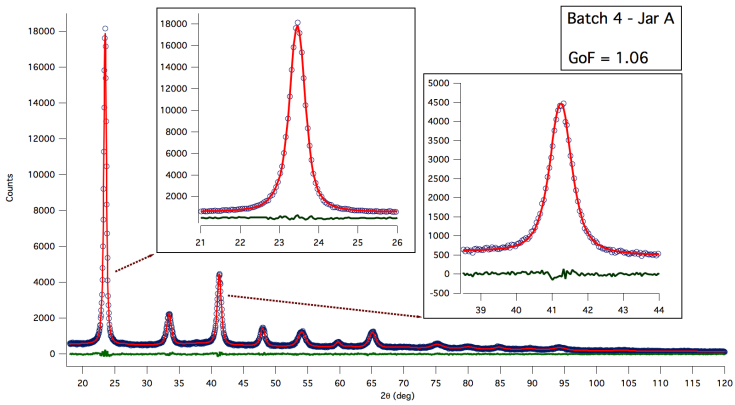

Figure 75: WPPM results with simulated IPF: experimental data (circle), model (line) and residual (line below). Insets show details of the modelling of the two most intense reflections.

It is possible to conclude that the simulation is accurate enough to give fully compatible results with the output of a LPA made with real experimental data.

5.4.1.7 Residual Differences between experimental data and simulation

A concluding remark on the peak shape is that, even within a generally good agreement, the simulation shows some residual discrepancies in the tails of the peak. We put forward that differences might originate from an incomplete reproducibility of the behaviour of the DCM 2nd crystal, regarding the outgoing photon beam angular divergence and spatial distribution, altered by the residual mechanical effects.

Without a direct measurement, it is almost impossible to *a priori* know the nature and the size of them, like a possible residual anticlastic curvature or where a twist line is and their dependence on the crystal curvature radius.

Were the real surface map available, SHADOW would allow overlapping it as a mesh on an optical element, thus producing a completely customized surface. Such a level of detail, considering the satisfactory agreement obtained so far, is currently beyond the scope of the simulation tool and its typical usage, but it is left as a possible future development.

In order to visually quantify the effect on the photon beam characteristics we simulate the second DCM crystal with customized symmetrically twisted surfaces at 15 keV. This surface was obtained by firstly creating a planar surface with the same dimension of the second DCM crystal (upper one), then symmetrically rotating, in opposite directions, the two sides along a central axis, lying on the sagittal plane, by an angle producing a variation of the vertical quote of the vertexes by the same and opposite amount ΔZ.

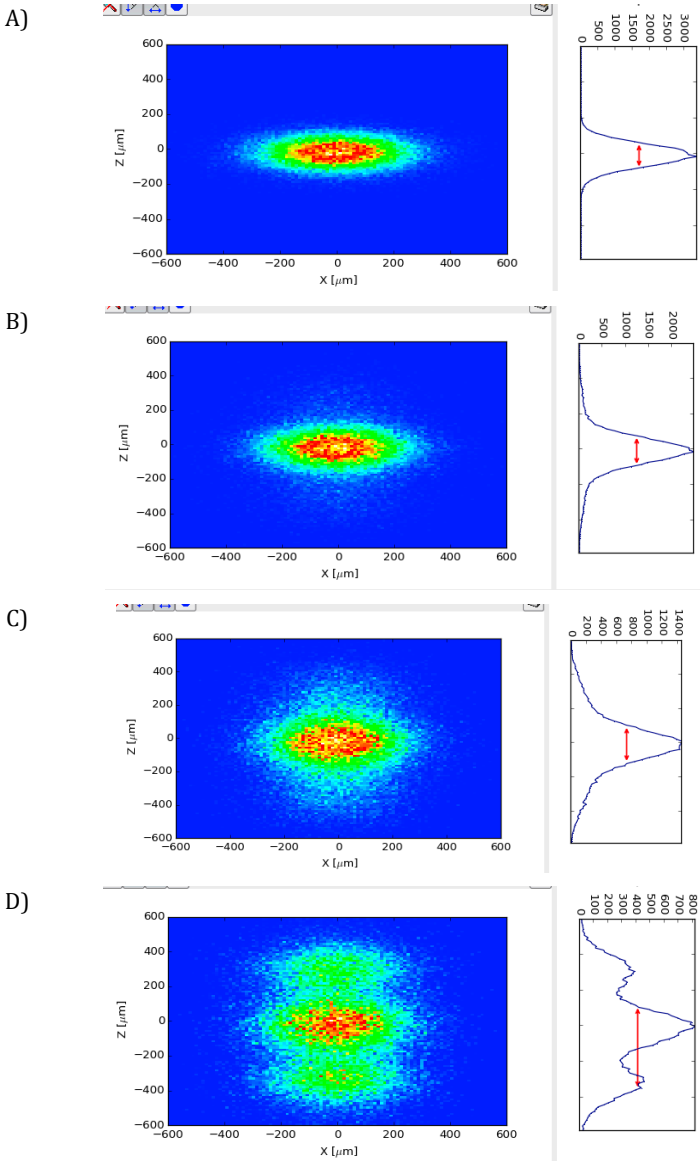

Figure 76: Effect on the beam spot at the detector quote, by twisting the second DCM crystal by an angle of 10 (B), 25 (C) and 50 (D) μrad, compared to the ideal situation (A)

The obtained twisted surface is then sagittally bent to produce the expected cylindrical radius of curvature to obtain the focusing condition. Figure 76 shows the progressive effect on the beam spot at the detector quote, by a twist rotation angle of 10, 25 and 50 μrad, corresponding to a ΔZ of 0.2 μm, 0.5 μm and 1.0 μm. The effect on the beam shape along the vertical direction is quite evident, in particular the progressive formation of tails, and then to a decomposition of the beam in different spots, even with a quite small modification of the surface.

This is not intended to be a realistic example, but can put in evidence how sensible to surface alteration the whole result is. This result also indicates that the mechanical bending action can introduce similar effects on the beam shape.

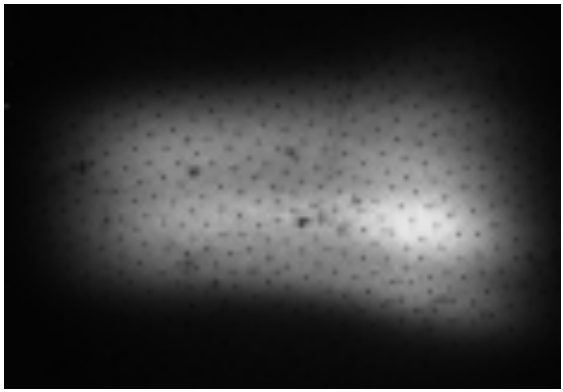

Figure 77: Direct image of the beam spot, acquired with a CCD positioned at 1 meter from the detector quote (focus position)

An image of the direct photon beam, shown in Figure 77, acquired with a CCD positioned (out of focus) at 1 meters from the detector quote (that is the focus position for both the optical planes), showed similar structures on the beam, revealing the presence of such a mechanical aberrations. In the same image it is also visible that the beam centre is slightly misaligned with respect to the crystal centre, being its intensity

concentrated in one side, as better visible in Figure 78, where the image has been rendered as a SHADOW beam.

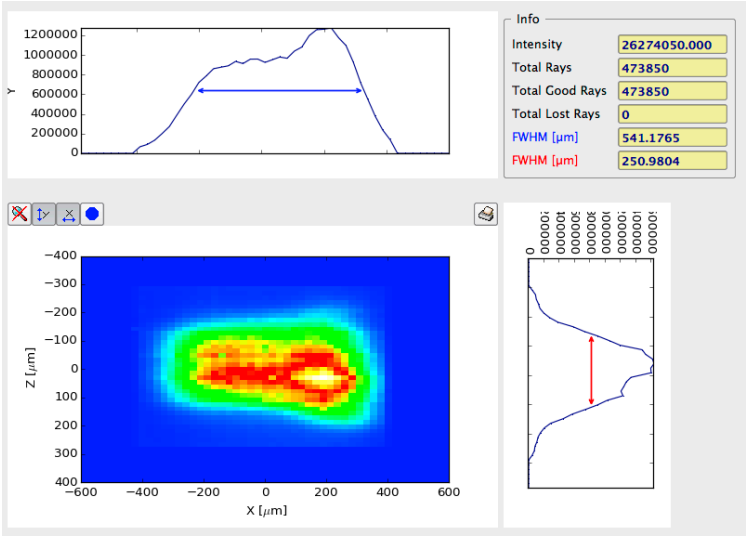

Figure 78: Direct image of the beam spot, rendered as a SHADOW beam, the level of asymmetry in the horizontal direction and the tails shape in the vertical direction are clearly visible.

5.4.2 11-BM at APS (Argonne National Laboratory)

We try now to understand possible limits of the simulation tool, analysing a beamline, similar to MCX, but without any previous knowledge of the experimental diffraction profiles of the crystals, in particular in presence of a sagittally bendable crystal.

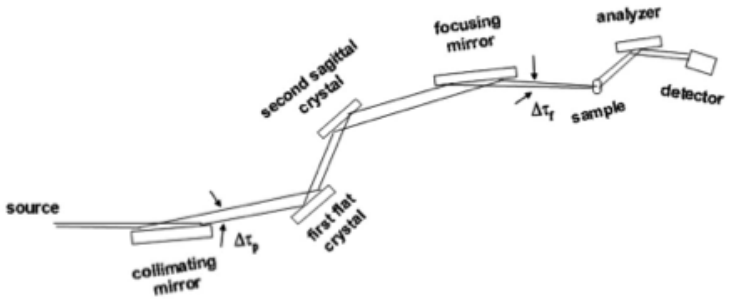

Figure 79: Optical layout of 11-BM beamline at APS (Argonne National Laboratory)

With an electron beam energy of 7 GeV, the source is a bending magnet with critical energy of 19.5 keV. The total length of the beamline is around 54 meter and the optical layout is composed of a first vertically collimating cylindrical bendable Pt-coated mirror, followed by a Si(111) double crystal monochromator, with a sagittally bendable second crystal [32], then by a second vertically focusing cylindrical bendable Pt-coated mirror (the whole layout is nearly identical to that of MCX, as visible in Figure 79).

The optical system, from the sample to the detector, is composed by an analyser crystal at a distance of 1 m, with entry slits of adjustable aperture from 0.2 to 3 mm. The detector is actually made of 12 of these analyser/scintillator optical systems, covering a total angular range of 24 degrees [109][110], as visible in Figure 80. The final signal emitted by the detector is actually a sort of convolution of the 12 separate signals [110].

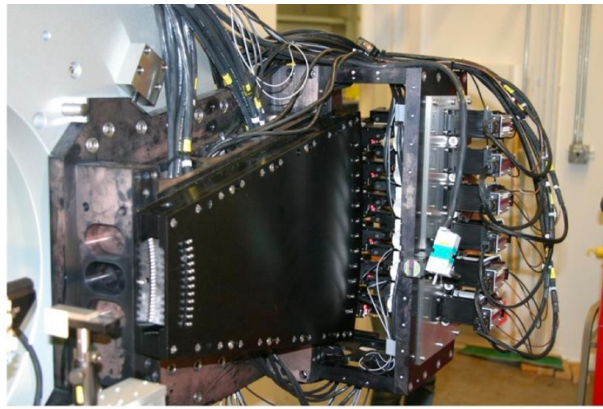

Figure 80: Detection system at 11-BM, made by 12 elements analyser/detector.

The experiment for characterizing the IPF used a 0.8 mm capillary filled with NIST SRM 660b LaB_6 [24][25], and photon beam energy of 29.958 keV.

Figure 81 and Figure 82 show, respectively, a comparison between experimental diffraction peak and simulated one, and between experimental instrumental peak broadening and simulated one.

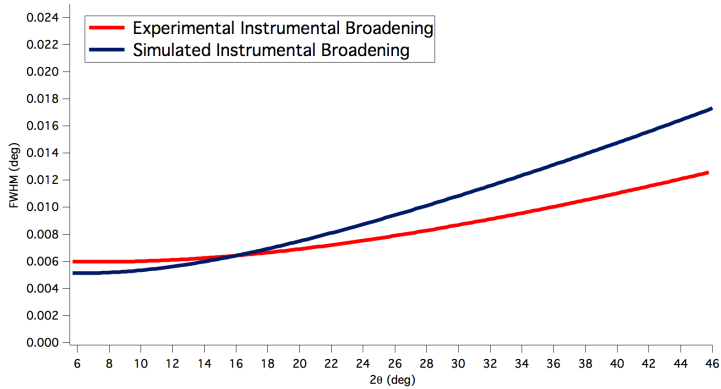

Figure 81: Comparison between experimental instrumental peak broadening at 29.958 keV photon energy and the simulated one.

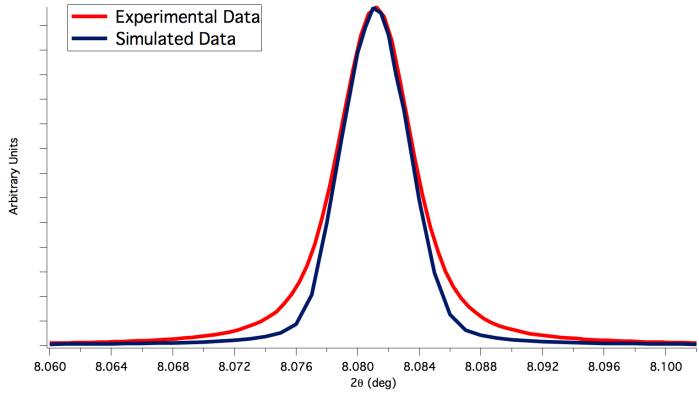

Figure 82: Comparison between experimental LaB_6 (1,1,0) peak at 29.958 keV photon energy and the simulated one.

We can suppose that, by adding to the simulation the missing optical effects, this estimation would raise to more realistic values, as it happened during the study of MCX at Elettra-Sincrotrone Trieste, where considerable improvements were observed after adding to the simulation the diffraction profiles reconstructed from the experimental rocking curves.

5.4.2.1 LPA of FeMo diffraction profiles at 29.958 keV with simulated IPF

We can now test the quality of the simulation in the same way we did for MCX, so to understand the limit of using theoretical diffraction profiles of the DCM crystals, and a weaker general agreement. A sample of the same material discussed in Chapter 4 has been measured at 11-BM, in a 0.3 mm Kapton® capillary.

The results of WPPM are summarized in the following table:

	Parameter	WPPM with experimental IPF	WPPM with simulated IPF
Size	$<D>$	9.2(3) nm	9.3(3) nm
	s.d.	5.7(4) nm	5.6(3) nm
	$<D>_S$	10.1(3) nm	10.2(3) nm
	$<D>_V$	10.8(3) nm	10.8(3) nm
Strain	ρ	6.8(1) 10^{16} m^{-2}	7.4(2) 10^{16} m^{-2}
	R_e	2.0(1) nm	1.8(1) nm
	f_E	0.70(1)	0.71(1)

In Figure 83 and Figure 84 it is possible to see the WPPM fit with the experimental and simulated IPF, respectively, observing that again the global accuracy has been reproduced, the two fits being almost undistinguishable.

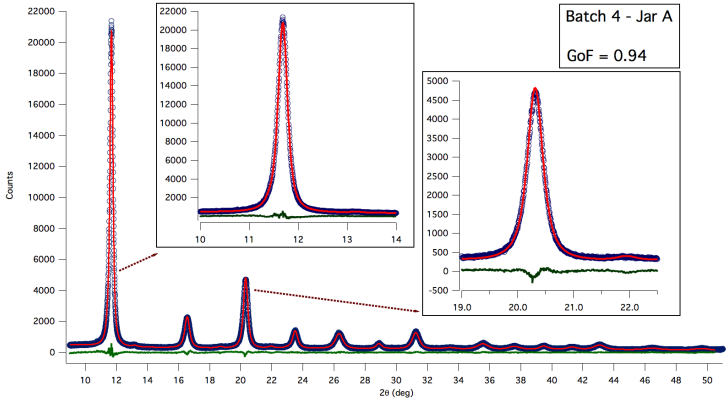

Figure 83: WPPM results with real 11-BM IPF: experimental data (circle), model (line) and residual (line below). Insets show details of the modelling of the two most intense reflections.

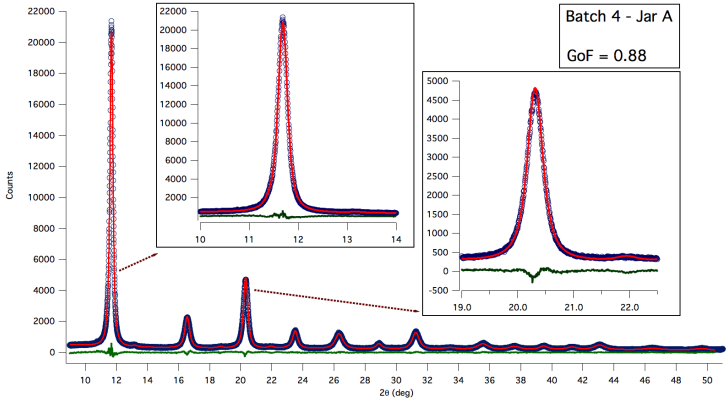

Figure 84: WPPM results with simulated IPF: experimental data (circle), model (line) and residual (line below). Insets show details of the modelling of the two most intense reflections.

We can also notice that while the size parameters are perfectly compatible between the two fits, small differences appear in the strain parameters, and this can be explained by the discrepancy in the simulated instrumental broadening at high angle: as discussed in Chapter 4, Figure 44, while the size effects are constant throughout the reciprocal space and parameters calculation is dominated by the principal peaks (where a better agreement between the experimental and simulated IPFs occurs), the broadening caused by strain increase with the angle, and the parameters calculation is more sensible to the whole IPF.

In any case, a general complete agreement between the WPPM results with experimental and simulated instrumental broadening has been obtained, indicating that the simulator gives reasonable data even if the real energy distribution profile of the photon beam (strongly determined by the real shape of the diffraction profiles of the crystals) is not known.

5.5 Conclusions

A new software for realistic ray-tracing of powder diffraction has been introduced, to become a tool for simulating the instrumental effects in powder diffraction profiles at synchrotron radiation beamlines. As an off-line tool, it can be adopted by beamline users to drive experiment design and sample preparation according to the beamline layout and beam energy, and by beamline scientists to improve the performance of existing beamlines. It can also become a valid tool to improve the quality of design of optical components and beamline layouts, with a realistic-experiment-oriented approach.

A comparison with experimental IPFs of two different beamlines and at different energies has been performed, discovering that the IPF is strongly dominated by the energy distribution profile of the photon beam at the sample, which is, in case of a XRPD beamline with DCM, principally determined by the diffraction profiles of the crystals of the monochromator.

In order to quantitatively check the quality of the simulated IPF, a comparison between LPA with WPPM on ball milled FeMo powder patterns using the experimentally measured instrumental broadening and the simulated one has been performed, obtaining totally compatible results.

Chapter 6

Conclusion and Future Developments

The potential of modern methods for XRD LPA can be fully exploited with data collected at SR beamlines, provided that optics and experimental set-up are suitably designed and characterized. In this Thesis work we showed

(i) a way to characterize optical components for powder diffraction beamlines, to properly calibrate and adjust all components to deliver the beam under the best possible conditions,
(ii) how to experimentally determine the IPF with SRMs.

The study of the Material Characterization by X-ray Diffraction beamline, MCX, at Elettra-Sincrotrone Trieste [26][79], showed how this beamline can operate with a set-up optimally arranged to study nanostructured materials, investigating details of crystalline domain size and shape, lattice defects and local atomic displacement of static and dynamic nature.

In order to remark how LPA capability of determining the characteristics of nanostructured material is strongly affected by the shape and the stability of the IPF, LPA of two nanostructured materials with large crystalline domains (Cu_2ZnSnS_4 [48][49] and EVAVIRENZ [56]), where the IPF is the dominant part of the collected signal, have been described. In these two cases of study, the possibility of characterizing microstructural properties of nanostructured materials in a wide range of values was a crucial added value to the research work. Measurements of diffraction patterns were made at the MCX in two of the available setups: Bragg-Brentano (flat-plate sample holder) and Debye-Scherrer (capillary sample holder).

In order to propose tools that could improve the current capability of performing such a kind of investigations, this Thesis work offered two different tools:

(i) a possible reference material for diffraction LPA, in particular for separating size and strain broadening effects: an iron-molybdenum alloy powder, extensively deformed by high energy milling, so to refine the bcc iron domain size to nanometer scale (≈10 nm) and introduce a strong inhomogeneous strain;

(ii) a ray-tracing based simulation software, designed to reproduce optical elements in a realistic form, so to evaluate the effects of aberrations, with the final purpose of reconstructing the IPF of the beamline. The role of each element can be investigated independently, so to point out the role and effect of each one separately.

Both tools showed promising features and convincing results allowing us to start sharing them with the scientific community and to prosecute the research work on them. The following paragraphs describe future perspectives for the research work discussed in this Thesis.

The FeMo Alloy

FeMo alloy characterization and production is supposed to pass through a successive phase: a RR involving a number of laboratories to test experimental LPA practices and analytical methods. The results already obtained, besides supporting the possibility of using this material as a reference for *size* and *strain* broadening using any suitable LPA method, might be the basis of a certification protocol.

SHADOW-based XRD simulations

Results of the ray-tracing simulations showed how sensible is the IPF to the characteristics of the optical elements, and in particular the energy distribution profile of the photon beam at the sample. A deeper study of the characteristics of DCM monochromators, with different bending mechanisms and different energy ranges of typical usage, could open the door to the possibility of modelling such kind of aberrations, even in an approximate or probabilistic way. This might lead to a different representation of the instrumental profile, described in terms of each contributing optical element. Beamline designers, staff and users might then obtain more realistic and safe predictions of the instrumental features.

Simulation of other XRPD setups is also under development, and, as an example, in Figure 85 it is possible to see a preliminary result of the simulation of the XRD1 beamline at Elettra-Sincrotrone Trieste [111]. The diffraction signal is compared with the output from a Dectris® Pilatus2M [112] area detector.

A) 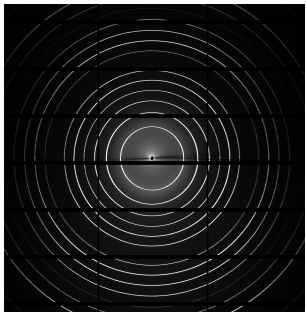 B) 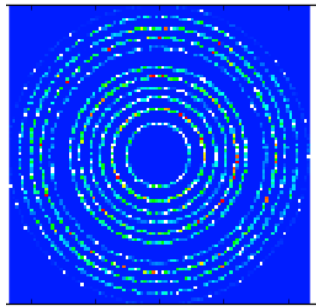

Figure 85: Preliminary results of the simulation of an area detector: comparison between the Pilatus2M signal at XRD1 at Elettra-Sincrotrone Trieste (A) and the simulated signal (B)

The simulated diffracted pattern will be transformed from a SHADOW beam in a Pilatus TIFF image, with the same resolution in pixels and the "black areas" (the detector is made of a matrix of identical moduli, separated by not sensible areas), in order to be processed by the same analysis software (like Fit2D [113][114]) and compared.

The OASYS Project

A challenging and interesting spin-off of the last part of this Thesis work is an evolution of the ORANGE-SHADOW tool, already emerged as its natural extension : the Orange Synchrotron Suite (OASYS) project [115], a common platform to build and/or integrate synchrotron-oriented simulation tools that communicate, and be the upper layer of the application presented to the user

As schematically represented in Figure 86, the main idea is to create a common language and common visual tool (widgets) for describing and designing virtual synchrotron experiments, to which many different optical simulation tools, like SHADOW [20][21][22][23], XOP [42] or SRW [116] (a beamline simulator based on the wavefront propagation), can be plugged in as specialized backends.

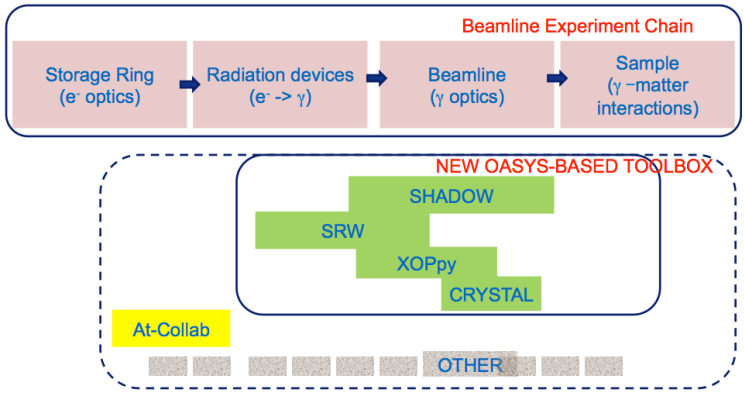

Figure 86: Schematic representation of the chain of simulation engines necessary for an X-ray virtual experiment,

The beamline experiment chain will be described in a very general way by a kind of "glossary" set of widgets, a collection of entities containing the minimum amount of parameters needed to describe the beamline source and components and a common input for every calculation backend.

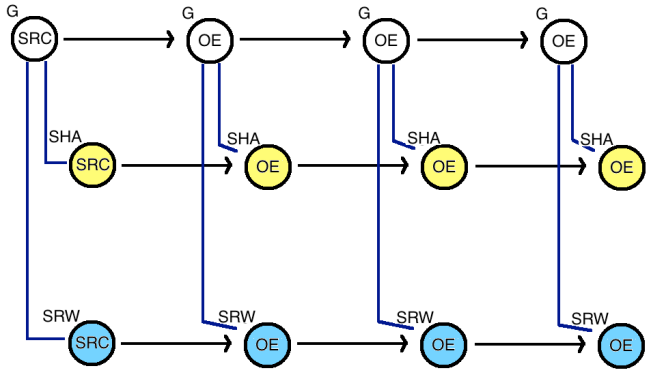

Figure 87: Schematic representation of the glossary widget framework. Simulations of the same beamline with different tools (blue and yellow) kept phased by common glossary widgets (white).

A schematic representation of the glossary widget framework is visible in Figure 87: glossary widgets will represent the beamline at the highest abstraction level and will send glossary objects to populate common information in the specialized widgets. Simulations of the same beamline with different tools are kept phased by common glossary objects will avoid typical redundancy when using different simulation tools.

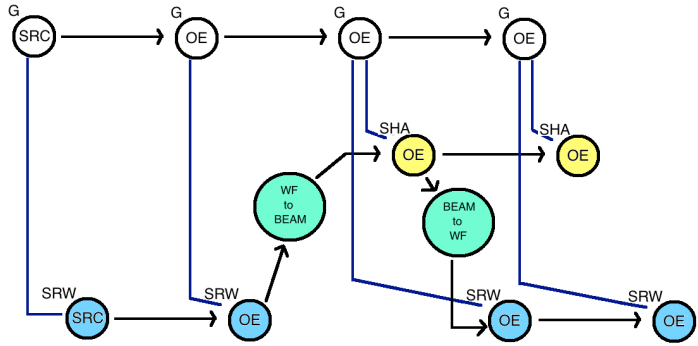

Figure 88: Dedicated widgets letting different tools communicate and share information can be implemented without heavy entanglement

In the Glossary framework, dedicated widgets letting different tools communicate and share information can be implemented without heavy entanglement (see Figure 88), and, as an example, the coupling between SHADOW and SRW, which is under development, will open the door to the simulation of the coherent diffraction from materials.

The research on EFAVIRENZ

Thanks to promising results obtained in the first campaign of measurement on EFAVIRENZ anti-HIV drug [56], a deeper investigation was recently performed, with new XRPD measurements at the MCX beamline with the capillary setup.

Thanks to the achievements of this Thesis work a better experimental setup was used, with Kapton capillaries of 0.3 mm of diameter, in order to reduce spurious signals from the sample holder, and to produce a smaller instrumental signal. The instrumental profile has been calculated with a sample composed of a NIST SRM 660a LaB_6 [25] (instrumental broadening, peak shape and position) and NIST SRM 675 Mica [117] (low 2θ peak position), diluted in Carbon powder to achieve the same level of absorption as the drug sample (see Figure 89).

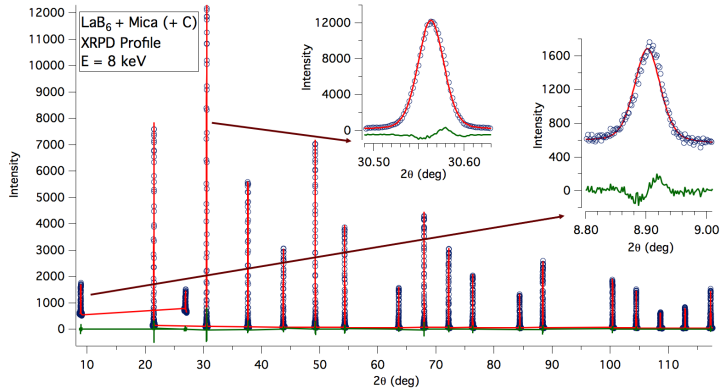

Figure 89: Standard LaB_6 + Mica powder pattern at 8 keV: experimental data (circle) and fit (line), with their difference (residual, line below).. Insets show details of low angle peak profiles. Mica poor signal asked for an acquisition time bigger by a factor 5.

As visible in Figure 90, the instrumental signal is drastically reduced with respect to the previous experiments (see Figure 33), ensuring a better sensibility to microstructural parameters.

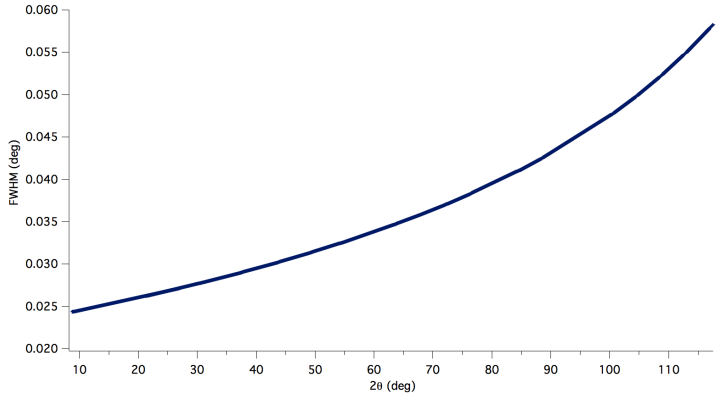

Figure 90: Instrumental broadening (represented as Full Width at Half Maximum – FWHM) at 8 keV beam energy.

A set of 13 powdered EFAVIRENZ samples were investigated, and very preliminary results of 8 samples are available (courtesy of Dr. C.L. Azanza Ricardo, University of Trento), regarding the phase identification: it is known that EFAVIRENZ may exhibit several polymorphs, being the most important in terms of stability and dissolution rate the type I and type II [57][118][119].
Taking into account the phases present in the measured samples, they can be subdivided in four groups:

(i) samples showing only the polymorph I,
(ii) samples having only the polymorph II,
(iii) sample with both phases,
(iv) samples with polymorph I together with an unknown spurious phase.

Examples of samples from every group are shown in Figure 91, Figure 92, Figure 93 and Figure 94.

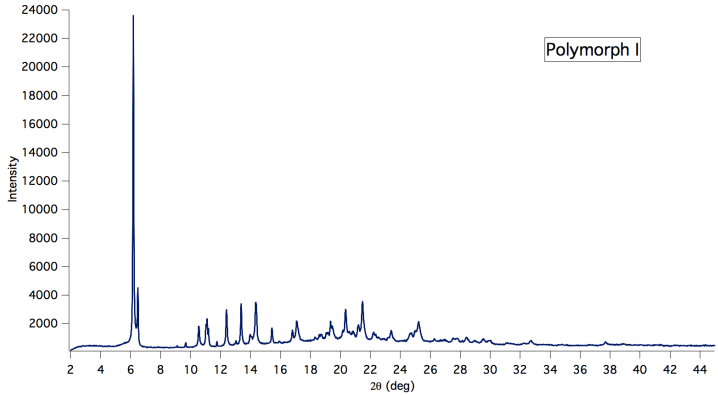

Figure 91: EFAVIRENZ Diffraction Pattern at 8 keV: Polymorph I sample.

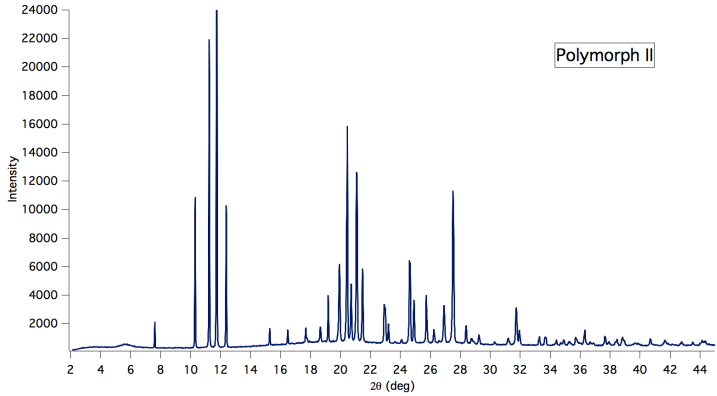

Figure 92: EFAVIRENZ Diffraction Pattern at 8 keV: Polymorph II sample.

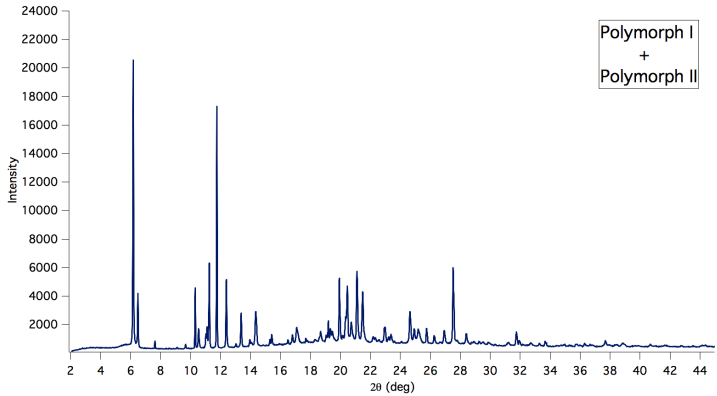

Figure 93: EFAVIRENZ Diffraction Pattern at 8 keV: Polymorphs I + II sample.

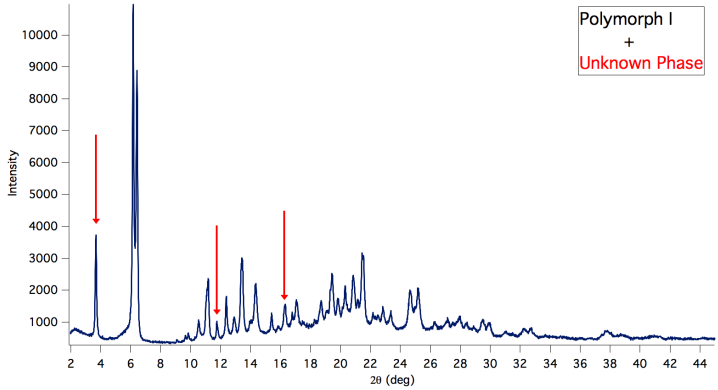

Figure 94: EFAVIRENZ Diffraction Pattern at 8 keV: Polymorph I + Unknown Phase sample.

The unknown phase doesn't correspond to any EFAVIRENZ structure described in the literature. Several hypothesis can be made, but the most credible one is those reflections correspond to a phase resulting from the presence of Hexane during the recrystallization process.

A new proposal for a campaign of measurements at MCX has been submitted to the Elettra-Sincrotrone Trieste scientific committee, with the aim to investigate the influence of the wet mechanical milling on the microstructure: different milling parameters and stabilizing agents will be analysed in order to obtain the best conditions. These are just a few of the many possible measurements that can be performed at MCX and benefit of the results of this Thesis.

List of abbreviation and acronyms

API	Application Programming Interface
BPR	Ball to Powder Ratio
DCM	Double Crystal Monochromator
DE	Dissolution Efficiency
EDAX	Energy Dispersive X-ray Analysis
EDS	Energy Dispersive X-ray Spectroscopy
EFV	EFAVIRENZ
ESRF	European Synchrotron Radiation Facility
FEG	Field Emission Gun
FWHM	Full Width at Half Maximum
GOF	Goodness of Fit
HAART	High Activity Antiretroviral Therapy
HRTEM	High Resolution Transmission Electron Microscope(y)
IPF	Instrumental Profile Function
LPA	Line Profile Analysis
MCX	Material Characterization by X-ray Diffraction beamline
PDF	Pair Distribution Functions
RR	Round Robin
RT	Room Temperature
SAXS	Small Angle X-ray Scattering
SEM	Scanning Electron Microscope(y)
SOC	Standard operating conditions
SR	Synchrotron Radiation
SRM	Standard Reference Material
TEM	Transmission Electron Microscope(y)
WPPM	Whole Powder Pattern Modelling
XRD	X-ray Diffraction
XRPD	X-ray Powder Diffraction

References

Chapter 1

[1] Mittemeijer E. J. and Scardi P. (Eds.), (**2004***). Diffraction Analysis of the Microstructure of Materials* (Springer series in Materials Science).

[2] Scardi P., Leoni M. and Delhez R. (**2004**). "Line broadening analysis using integral breadth methods: a critical review", J. Appl Cryst. **37**, pp. 381-390. doi:10.1107/S0021889804004583

[3] Klug H. P. and Alexander L. E. (**1974**). *X-ray Diffraction Procedures*, 2nd ed. New York: John Wiley.

[4] Mittemeijer E. J. and Welzel U.: in *Modern Diffraction Methods*, Eric J. Mittemeijer and Udo Welzel, eds., Wiley-VCH Verlag: Weiheim, Germany, 2013, pp. 89–126.

[5] Scherrer P. (**1918**). "Bestimmung der Grösse und der Inneren Struktur von Kolloidteilchen Mittels Röntgenstrahlen, Nachrichten von der Gesellschaft der Wissenschaften, Göttingen," Mathematisch-Physikalische Klasse **2**, pp. 98-100.

[6] Patterson A. (**1939**). "The Scherrer Formula for X-Ray Particle Size Determination," Phys. Rev. **56** (10), pp. 978–982. doi:10.1103/PhysRev.56.978

[7] Gozzo F., Cervellino A., Leoni M., Scardi P., Bergamaschi A. and Schmitt B. (**2012**). "Instrumental profile of MYTHEN detector in Debye-Scherrer geometry," Z. Kristallogr. **225**, 616. doi:10.1524/zkri.2010.1345

[8] Hinrichsen B., Dinnebier R.E. and Jansen M. (**2008**). Chapter 14 in *Powder Diffraction: Theory and Practice*, edited by R.E. Dinnebier & S.J.L. Billinge (The Royal Society of Chemistry, Cambridge, United Kingdom), pp. 414-438.

[9] Gelisio L. and Scardi P. (**2012**). "X-Ray Interference by Nanocrystalline domains", J. Nanosci. Nanotechnol. **12**, pp. 8811-8817. doi:10.1166/jnn.2012.6479

[10] Leonardi A., Leoni M. and Scardi P. (**2013**). "Directional pair distribution function for diffraction line profile analysis of atomistic models", J. Appl. Cryst. **46**, pp. 63–75. doi:10.1107/S0021889812050601

[11] Caglioti G., Paoletti A. and Ricci F. P. (**1958**). "Choice of collimators for a crystal spectrofotometer for neutron diffraction," Nuclear Instruments **3**, pp. 223-228. doi:10.1016/0369-643X(58)90029-X

[12] Sabine T. M. (**1987**). "A Powder Diffractometer for a Synchrotron Source," J. Appl Cryst. **20**, pp. 173-178. doi:10.1107/S0021889887086886

[13] Cheary R. W. and Coelho A. A. (**1998**). "Axial Divergence in a Conventional X-ray Powder Diffractometer," J. Appl. Cryst. **31**, pp. 862-868. doi:10.1107/S0021889898006888

[14] Cheary R. W., Coelho A. A. and Cline J. P. (**2004**). "Fundamental Parameters Line Profile Fitting in Laboratory Diffractometers," J. Res. Natl. Inst. Stand. Technol. **109**, pp. 1-25. doi:10.6028/jres.109.002

[15] Zuev A. D. (**2006**). "Calculation of the instrumental function in X-ray powder diffraction," J. Appl Cryst. **39**, pp. 304-314. doi:10.1107/S0021889806005693

[16] Zuev A. D. (**2008**). "Using the general equation of a conic for the calculation of the instrument function of a Bragg–Brentano diffractometer," J. Appl Cryst. **41**, pp. 115-123. doi:10.1107/S002188980704976X

[17] Scardi, P., Ortolani, M. and Leoni, M. (**2010**). "WPPM: microstructural analysis beyond the Rietveld method", Mater. Sci. Forum **651**, pp. 155-171. doi:10.4028/www.scientific.net/MSF.651.155

[18] Leoni M., Welzel U. and Scardi P. (**2004**). "Polycapillary Optics for Materials Science Studies: Instrumental Effects and Their Correction," J. Res. Natl. Inst. Stand. Technol. **109**, pp. 27-48. doi:10.6028/jres.109.003

[19] Lambert S. and Giullet F. (**2008**). "Application of the X-ray tracing method to powder diffraction line profiles," J. Appl Cryst. **41**, pp. 153-160. doi:10.1107/S0021889807055069

[20] Lai B. and Cerrina F. (**1986**). "SHADOW: A synchrotron radiation ray tracing program," Nucl. Instr. Meth. Phys. Res. A **246** (1-3), pp. 347-341. doi:10.1016/0168-9002(86)90101-4

[21] Welnak C., Chen G. J. and Cerrina F. (**1994**). "SHADOW: A synchrotron radiation and X-ray optics simulation tool," Nucl. Instr. Meth. Phys. Res. A **347** (1-3), pp. 344-347. doi:10.1016/0168-9002(94)91906-2

[22] Cerrina F. and Sánchez del Río M. (**2009**). *Handbook of Optics* (volume V, 3rd edition), edited by M. Bass, Mc Graw Hill, New York, ch. 35.

[23] Sánchez del Río M., Canestrari N., Jiang F. and Cerrina F. (**2011**). "SHADOW3: a new version of the synchrotron X-ray optics modelling package," J. Synchrotron Rad. **18**, pp. 708-716. doi:10.1107/S0909049511026306

[24] Black D. R., Windover D., Henins A., Filliben J. and Cline J. P. (**2010**). "Standard Reference Material 660b for X-ray Metrology," Adv. X-ray Anal. **54**, pp. 140-148.

[25] Cline J. P., Deslattes R. D., Staudenmann J.-L., Kessler E. G., Hudson L. T., Henins A. and Cheary R. W. (**2000**). "Certificate SRM 660a", NIST, Gaithersburg, MD, USA.; NIST (**2010**). "Lanthanum Hexaboride Powder Line Position and Line Shape Standard for Powder Diffraction (SRM 660b)", Gaithersburg, MD; National Institute of Standards and Technology; U.S. Department of Commerce.

[26] www.elettra.eu

[27] Artini C., Costa G.A., Pani M., Lausi A., Plaisier J.R. (**2012**). "Structural characterization of the CeO_2/Gd_2O_3 mixed system by synchrotron X-ray diffraction", J. Solid State Chem. **190**, pp. 24-28. doi: 10.1016/j.jssc.2012.01.056

[28] Ivetic G., Meneghin I., Troiani E., Molinari G., Ocaña J., Morales M., Porro J., Lanciotti A., Ristori V., Polese C., Plaisier J.R., Lausi A. (**2012**). "Fatigue in laser shock peened open-hole thin aluminium specimens", Mater. Sci. Eng. A **534**, pp. 573-579. doi: 10.1016/j.msea.2011.12.010

[29] Cobourne G., Mountjoy G., Rodriguez-Blanco J.D., Benning L.G., Hannon A.C. and Plaisier J.R. (**2014**). "Neutron and X-ray diffraction and empirical potential structure refinement modelling of magnesium stabilised amorphous calcium carbonate", J. Non-Cryst. Solids. In press, doi:10.1016/j.jnoncrysol.2013.12.023.

[30] Ventruti G., Scordari F., Ventura G.D., Bellatreccia F., Gualtieri A.F., and Lausi A. (**2013**). "The thermal stability of sideronatrite and its decomposition products in the system Na_2O-Fe_2O_3-SO_2-H_2O", Phys. Chem. Miner. **40**, pp. 659-670. doi: 10.1007/s00269-013-0601-9

[31] Gatta G.D., Merlini M., Lotti P., Lausi A. and Rieder M. (**2012**). "Phase stability and thermo-elastic behavior of $CsAlSiO_4$ (ABW): A potential nuclear waste disposal material", Microporous Mesoporous Mater. **163**, pp. 147-152. doi: 10.1016/j.micromeso.2012.07.010

[32] Zhang L., Hustace R., Hignette O., Ziegler E. and Freund A. (**1998**). "Design optimization of a flexural hinge-based bender for X-ray optics," J. Synchrotron Rad. **5**, pp. 804-807. doi:10.1107/S0909049597015288

[33] Riello P., Lausi A., MacLeod J., Plaisier J.R., Zerauschek G. and Fornasiero P. (**2013**). "In situ reaction furnace for real-time XRD

studies", J. Synchrotron Rad. **20**, pp. 194-196. doi: 10.1107/S0909049512039246

[34] Authier A. (1st edition **2001**/ 2nd edition **2003**). *Dynamical theory of X-ray diffraction*. IUCr monographs on crystallography, no. 11. Oxford University Press. ISBN 0-19-852892-2.

[35] Zachariasen W. H. (**1945**). *Theory of X-ray Diffraction in Crystals*. Edited by J. Whiley and Sons, Inc., New York (USA) and Chapman & Hall, Ltd., London (UK)

[36] Rutishauser S., Rack A., Weitkamp T., Kayser Y., David C. and Macrander A.T. (**2013**). "Heat bump on a monochromator crystal measured with X-ray grating interferometry", J. Synchrotron Rad. **20**, pp. 300-305, doi:10.1107/S0909049513001817

[37] Chumakov A. I., Sergeev I., Celse J.P., Ruffer R., Lesourd M., Zhang L. and Sánchez del Río M. (**2014**). "Performance of a silicon monochromator under high heat load", J. Synchrotron Rad. **21**, pp. 315-324. doi:10.1107/ S1600577513033158

[38] http://radiant.harima.riken.go.jp/spectra/

[39] Tanaka T. (**2014**). "Numerical methods for characterization of synchrotron radiation based on the Wigner function method" Phys. Rev. ST-AB, **17**, 060702. doi:10.1103/PhysRevSTAB.17.060702

[40] Krisch M., Freund A., Marot G. and Zhang L. (**1991**). "Study of dynamically bent crystals for X-ray focusing optics", Nucl. Instrum. Meth. A **305**, pp. 208-213. doi:10.1016/0168-9002(91)90536-Y

[41] Freund A.K., Comin F., Hazemann J.L., Hustache R., Jenninger B., Lieb K. and Pierre M. (**1998**). "Performances of various types of benders for sagittally focusing crystals on ESRF synchrotron beamlines", Proc. SPIE **3448**, Crystal and Multilayer Optics, 144. doi:10.1117/12.332501

[42] Sánchez del Río M. and Dejus R.J. (**2011**). "XOP v2.4: recent developments of the x-ray optics software toolkit", Proc. SPIE **8141**. doi:10.1117/12.893911

[43] Sánchez del Río M., Perez-Bocanegra N., Shi X., Honkimäki V. and Zhang L. (**2015**). "Simulation of X-ray diffraction profiles for bent anisotropic crystals", accepted for publication by J. Appl. Crystallogr., preprint available online: http://arxiv.org/abs/1502.03059.

[44] Scardi P., Lutterotti L. and Maistrelli P. (**1994**). "Experimental Determination of the Instrumental Broadening in the Bragg-Brentano Geometry," Powder Diffr. **9**, pp. 180-186. doi:10.1017/S0885715600019187

[45] Scardi P. and Leoni M. (**1999**). "Fourier modelling of the anisotropic line broadening of X-ray diffraction profiles due to line and plane lattice defects", J. Appl. Crystallogr. **32**, pp. 671-682. doi:10.1107/S002188989900374X

[46] Wilson A.J.C. (**1963**). *Mathematical Theory of X-ray Powder Diffractometry*, Eindhoven, The Netherland: Philips Technical Library.

[47] Dong Y.H. and Scardi P. (**2000**). "MarqX: a new program for whole-powder-pattern fitting", J. Appl. Crystallogr. **33**, pp. 184-189. doi:10.1107/S002188989901434X

Chapter 3

[48] Malerba C., Biccari F., Azanza Ricardo C.L., Valentini M., Chierchia R., Mueller M., Santoni A., Esposito E., Magiapane P., Scardi P. and Mittiga A. (**2014**). "CZTS stoichiometry effects on the band gap energy". J. Alloys Compd. **582**, pp. 528–534. doi:10.1016/j.jallcom.2013.07.199

[49] Malerba C., Azanza Ricardo C.L., Valentini M., Biccari F., Müller M., Rebuffi L., Esposito E., Mangiapane P., Scardi P. and Mittiga A. (**2014**). "Stoichiometry effect on Cu_2ZnSnS_4 thin films morphological and optical properties", J. Renewable Sustainable Energy **6**, 011404. doi:10.1063/1.4866258

[50] Bruker-AXS, TOPAS Version 3, Karsrluhe, Germany, **2000**, http://www.bruker-axs.com/topas.html.

[51] Cheary R.W. and Coelho A. (**1992**). "A fundamental parameters approach to X-ray line-profile fitting", J. Appl. Crystallogr. **25**, pp. 109-121. doi:10.1107/S0021889891010804

[52] Leoni M., Confente T. and Scardi P. (**2006**). "PM2K: a flexible program implementing Whole Powder Pattern Modelling", Z. Kristallogr. Suppl. **23**, pp. 249-254. doi:10.1524/zksu.2006.suppl_23.249

[53] Chiappetta D.A., Alvarez-Lorenzo C., Rey-Rico A., Taboada P., Concheiro A. and Sosnik A. (**2010**). "N-alkylation of poloxamines modulates micellar assembly and encapsulation and release of the antiretroviral efavirenz", Eur. J. Pharm. Biopharm. **76**, pp. 24-37. doi:10.1016/j.ejpb.2010.05.007.

[54] European Medicine Agency (**2010**). Available: <http://www.ema.europa.eu/docs/en_GB/document_library/Scientific_guideline/2010/01/WC500070039.pdf>. Accessed: 19 march 2015.

[55] Brasil. Resolução n° 391, de 9 de agosto de 1999. Available: <http://www.anvisa.gov.br/hotsite/genericos/legis/resolucoes/391_99.htm>. Accessed: 19 march 2015

[56] Fandaruff C., Segatto Silva M.A., Galindo Bedor D.C., Pereira de Santana D., Antunes Rocha H.V., Rebuffi L., Azanza Ricardo C.L., Scardi P. and Cuffini S.L. (**2015**). "Correlation between microstructure and bioequivalence in Anti-HIV Drug Efavirenz",

Eur. J. Pharm. Biopharm. **91**, pp. 52–5. doi: 10.1016/j.ejpb.2015.01.020

[57] Mahapatra S., Thakur T.S., Joseph S., Varughese S. and Desiraju G.R. (**2010**). "New Solid State Forms of the Anti-HIV Drug Efavirenz. Conformational Flexibility and High Z′ Issues", Cryst. Growth Des. **10**, pp. 3191-3202. doi: 10.1021/cg100342k.

[58] Scardi P. (2008). *Powder Diffraction: Theory and Practice*, R.E. Dinnebier and S.J.L. Billinge, eds., The Royal Society of Chemistry, Cambridge, United Kingdom, pp. 376–413

[59] Leoni M., Martinez-Garcia J. and Scardi P. (**2007**). "Dislocation effects in powder diffraction." J. Appl. Cryst. **40**, pp. 719- 724. doi:10.1107/S002188980702078X

[60] Black D. R., Windover D., Henins A., Gil D., Filliben J. and Cline J. P. (**2009**). "Standard Reference Material 640a for X-ray Metrology", Adv. X-Ray Anal. **53**, pp. 172-179

[61] Scardi P. and Leoni M. (**2001**). "Diffraction line profiles from polydisperse crystalline systems", Acta Cryst. A **57**, pp. 604–613. doi: 10.1107/S0108767301008881

Chapter 4

[62] Warren, B. E. (**1969**). *X-ray Diffraction*, pp. 251–314. New York: Addison-Wesley.

[63] Schwartz L. H. and Cohen, J. B. (**1987**). *Diffraction from Materials*. Berlin: Springer.

[64] Guinebretière R. (**2007**). *X-ray Diffraction by Polycrystalline Materials*. ISTE, London, United Kingdom.

[65] Snyder R.L., Fiala, J., Bunge H.-J. (**2000**). Editors. *Defect and Microstructure Analysis by Diffraction*. Oxford: Oxford University Press.

[66] Scardi P., Leoni M., Müller M. and Di Maggio R. (**2010**). "In situ size-strain analysis of nanocrystalline ceria growth", Mat. Sci. Eng. A **528**, pp. 77–82. doi: 10.1016/j.msea.2010.03.077

[67] Abdellatief M., Lausi A., Plaisier. J. R. and Scardi P. (**2014**). "Influence of Lattice Defects on the Grain Growth Kinetics of Nanocrystalline Fluorite", Met. Mat. Trans. A **45**, pp. 123–128. doi: 10.1007/s11661-013-1786-8

[68] Molinari A., Libardi S., Leoni M. and Scardi, P. (**2010**). "Role of lattice strain on thermal stability of a nanocrystalline FeMo alloy", Acta Mater. 58, pp. 963-966. doi: 10.1016/j.actamat.2009.10.012

[69] Abdellatief M. ,Abele M., Leoni M. and Scardi P. (**2013**). "Combined X-ray diffraction and solid-state ^{19}F magic angle spinning NMR analysis of lattice defects in nanocrystalline CaF_2", J. Appl. Cryst. **46**, pp. 1049-1057. doi:10.1107/S0021889813016944

[70] Fais A., Leoni M. and Scardi P. (**2012**). "Fast Sintering of Nanocrystalline Copper", Met. Mat. Trans A **43** [5], pp. 1517-1521. doi: 10.1007/s11661-011-0727-7

[71] Cline J. P., Leoni M., Black D., Henins, A. Bonevich J.E., Whitfield P.S., and Scardi P. (**2013**). "Crystalline domain size and faulting in the new NIST SRM 1979 zinc oxide", Powder Diffr. **11**, 28(S2):S22-S32. doi: 10.1017/S0885715613001188

[72] Balzar D., Audebrand N., Daymond M.R., Fitch A., Hewat A., Langford J.I., Le Bail A., Louer D., Masson O., McCowan C.N., Popa N.C., Stephens P.W. and Toby B.H. (**2004**). "Size-strain line-broadening analysis of the ceria round-robin sample", J. Appl. Cryst. **37**, pp. 911–924. doi:10.1107/S0021889804022551

[73] http://www.hoganas.com

[74] Brenner S.S. (**1955**). "Oxidation of Iron-Molybdenum and Nickel-Molybdenum Alloys", J. Electrochem. Soc. **102** [1], pp. 7-15. doi:10.1149/1.2429990

[75] http://www.fritsch-milling.com

[76] Troian A. (2013). “Production and characterization of a microstructure reference material for X-ray powder diffraction”. Master Degree Thesis, University of Trento.

[77] Troian A., Rebuffi L., Leoni M. and Scardi P. (**2014**). “Toward a reference material for line profile analysis”, Powder Diffr., published online. doi:10.1017/S0885715614001298

[78] D’Incau M., Leoni M. and Scardi P. (**2007**). “High-energy grinding of FeMo powders”, J. Mater. Res. **22**, pp. 1744-1753. doi: 10.1557/JMR.2007.0224

[79] Rebuffi L., Plaisier J.R., Abdellatief M., Lausi A. and Scardi P. (**2014**). “MCX: a Synchrotron Radiation Beamline form X-ray Diffraction Line Profile Analysis”, Z. Anorg. Allg. Chem. **640**, pp. 3100-3106, doi: 10.1002/zaac.201400163

[80] Amenitsch H., Rappolt M, Kriechbaum M, Mio H, Laggner P and Bernstorff S. (**1998**). “First performance assessment of the small-angle X-ray scattering beamline at ELETTRA”, J. Synchrotron. Radiat. **5** [3], pp. 506-508. doi:10.1107/S090904959800137X

[81] Maslen E. N. (**2006**). *International Tables for Crystallography* Vol. C, Chapter 6.3, pp. 599-608.

[82] Scardi P. and Leoni M. (**2002**). “Whole powder pattern modelling”, Acta Cryst. A **58**, pp. 190–200. Doi: 10.1107/S0108767301021298

[83] Krivoglaz M. A. and Ryaboshapka K. P. (**1963**). “Theory of X-ray scattering by crystals containing dislocations, screw and edge dislocations randomly distributed throughout the crystal”, Fiz. Metallov. Metalloved. **15**, pp. 18-31.

[84] Wilkens M. (**1970**). *Fundamental Aspects of Dislocation Theory*, edited by J. A. Simmons, R. de Wit & R. Bullough, Vol. II, pp. 1195-1221. National Bureau of Standards (US) Special Publication No. 317. Washington, DC: National Bureau of Standards.

[85] Wilkens M. (**1970**). “The determination of density and distribution of dislocations in deformed single crystals from broadened X-ray

diffraction profiles", Phys. Stat. Sol. **2** [2], pp. 359-370. doi: 10.1002/pssa.19700020224

[86] Langford J.I. and Wilson A.J.C. (**1978**). "Scherrer after sixty years: A survey and some new results in the determination of crystallite size", J. Appl. Cryst. **11**, pp. 102-113. doi:10.1107/S0021889878012844

[87] Warren B.E. and Averbach B.L. (**1950**). "The Effect of Cold-Work Distortion on X-Ray Patterns", J. of Applied Physics **21**, pp. 595-599. doi:10.1063/1.1699713

[88] Warren B.E. and Averbach B.L. (**1952**). "The Separation of Stacking Fault Broadening in Cold-Worked Metals", J. of Applied Physics **23**, pp. 1059. doi: 10.1063/1.1702352

[89] Hull D. and Bacon D.J. (**2007**). *Introduction to Dislocations*, Butterworth-Heinemann, 5th ed.

[90] Fitzpatrick M.E. and Lodini A., eds. (**2003**). *Analysis of Residual Stress by Diffraction using Neutron and Synchrotron Radiation*, Taylor & Francis Inc, New York, USA. (Cap. 3 and 5).

[91] Schulze V., Voehringer O. and Macherauch E. (**2010**). *Quenching Theory and Technology*, Second Edition, Edited by Bozidar Liscic , Hans M. Tensi , Lauralice C. F. Canale and George E. Totten. CRC Press. doi: 10.1201/9781420009163-c9

[92] Skrzypek J.J., Ganczarski A.W., Rustichelli F. and Egner H. (**2008**). *Advanced materials and structures for Extreme Operating Conditions*, Springer, p. 178.

[93] Leonardi A. and Scardi P. (2015). "Dislocation Effects on the Diffraction Line Profiles from Nanocrystalline Domains", Met. Mat. Trans A. Available online. doi: 10.1007/s11661-015-2863-y

[94] Vegard L. (**1921**). "Die Konstitution der Mischkristalle und die Raumfüllung der Atome", Zeitschrift für Physik **5** (1), pp. 17-26. doi:10.1007/BF01349680.

[95] Denton A.R. and Ashcroft N.W. (**1991**). "Vegard's law", Physical Review A 43, pp. 3161–3164. doi:10.1103/PhysRevA.43.3161.

[96] Liu X.D., Zhang H.Y., Lu K. and Hu Z.Q. (**1994**). "The lattice expansion in nanometre-sized Ni polycrystals", J. Phys. Condens. Matter **6**, L497. doi:10.1088/0953-8984/6/34/001

[97] Nazarov A.A., Romanov A.E. and Valiev R.Z. (**1996**). "Random disclination ensembles in ultrafine-grained materials produced by severe plastic deformation", Scripta Materialia **34**, pp. 729-734. doi: 10.1016/1359-6462(95)00573-0

[98] Leoni M., Scardi P., D'Incau M. and Luciani G. (**2012**). "Annealing Behavior of a Nanostructured Fe1.5Mo Alloy", Met. Mat. Trans A **43** [5], pp. 1522-1527. doi: 10.1007/s11661-011-0762-4

[99] Adler T. and Houska C.R. (**1979**). "Simplifications in the x-ray line-shape analysis", J. Appl. Phys. **50**, pp. 3282. doi: 10.1063/1.326368

[100] Martinez-Garcia J., Leoni M. and Scardi P. (**2008**). "A general approach for determining the diffraction contrast factor of straight-line dislocations", Acta Cryst. A **65**, pp. 109–119. doi:10.1107/S010876730804186X

Chapter 5

[101] http://www.python.org

[102] Demšar J. and Zupan B. (**2004**). "Orange: From Experimental Machine Learning to Interactive Data Mining," White Paper (http://orange.biolab.si/), Faculty of Computer and Information Science, University of Ljubljana.

[103] Azaroff L.V. (**1955**). "Polarization Correction for Crystal-Monochromatized X-radiation", Acta Cryst. **8**, pp. 701-704

[104] Lippmann T. and Schneider J.R. (**2000**). "Accurate structure-factor measurements using high-energy synchrotron radiation: a

test on Cuprite, Cu_2O", J. Appl. Cryst. **33**, pp. 156-167. doi:10.1107/S0021889899012790

[105] Von Dreele R.B. and Rodriguez-Carvajal J. (**2008**). *Powder Diffraction: Theory and Practice*, edited by R.E. Dinnebier & S.J.L. Billinge (The Royal Society of Chemistry, Cambridge, United Kingdom), ch. 3, pp. 58-88.

[106] Yinghua W. (**1987**). "Lorentz-polarization factor for correction of diffraction-line profiles", J. Appl. Cryst. **20**, pp. 258-259. doi:10.1107/S0021889887086746

[107] Schoonjans T., Brunetti A., Golosio B., Sánchez del Río M., Solé V.A., Ferrero C. and Vincze L. (**2011**). "The xraylib library for X-ray-matter interactions. Recent developments", Spectrochimica Acta Part B: Atomic Spectroscopy **66**, pp. 776-784. doi:10.1016/j.sab.2011.09.011

[108] Sánchez del Río M. and Marcelli A. (**1992**). "Waviness effects in ray-tracing of real optical surfaces", Nucl. Instr. Meth. A **319,** pp. 170-177, doi: 10.1016/0168-9002(92)90550-N

[109] Wang J., Toby B. H., Lee P. L., Ribaud L., Antao S. M., Kurtz C., Ramanathan M., Von Dreele R. B. and Beno M. A. (**2008**). "A dedicated powder diffraction beamline at the Advanced Photon Source: Commissioning and early operational results", Rev. Sci. Instrum. **79**, 085105, doi: 10.1063/1.2969260.

[110] Lee P.L., Shu D., Ramanathan M., Preissner C., Wang J., Beno M.A., Von Dreele R.B., Ribaud L., Kurtz C., Antao S.M., Jiao X. and Toby B.H. (**2008**). "A twelve-analyzer detector system for high-resolution powder diffraction", J. Synchrotron Rad. **15**, pp. 427-432. doi:10.1107/S0909049508018438

Chapter 6

[111] www.elettra.trieste.it/elettra-beamlines/xrd1.html

[112] Kraft P., Bergamaschi A., Brönnimann Ch., Dinapoli R., Eikenberry E.F., Graafsma H., Henrich B., Johnson I., Kobas M., Mozzanica A., Schlepütz C.M. and Schmitt B. (**2009**). "Characterization and Calibration of PILATUS Detectors", IEEE Trans. Nucl. Sci. **56** (3), pp. 758-764. doi:10.1109/TNS.2008.2009448

[113] Hammersley A.P., Svensson S.O., Hanfland M., Fitch A.N. and Häusermann D. (**1996**). "Two-Dimensional Detector Software: From Real Detector to Idealised Image or Two-Theta Scan", High Pressure Research **14**, pp. 235-248. doi:10.1080/08957959608201408

[114] Hammersley A.P., Brown K., Burmeister W., Claustre L., Gonzalez A., McSweeney S., Mitchell E., Moy J-P., Svensson S.O., Thompson A. (**1997**). "Monochromatic Protein Crystallography Data Collection Using an X-ray Image Intensifier/CCD Detector", J. Synchrotron Rad. **4**, pp. 67-77. doi:10.1107/S0909049596015087

[115] Sánchez del Río M., Rebuffi L., Demšar J., Canestrari N., Chubar O. (**2014**). "A proposal for an Open Source graphical environment for simulating X-ray optics", Proc. SPIE 9209, Advances in Computational Methods for X-Ray Optics III, 92090X. doi:10.1117/12. 2061834

[116] Chubar O. and Elleaume P. (**1998**). "Accurate And Efficient Computation Of Synchrotron Radiation In The Near Field Region", Proceedings of the EPAC98 Conference, 22-26 June 1998, pp. 1177-1179.

[117] Hubbard C.R. (**1982**) "Standard Reference Material 675 – Fluorophlogopite - Low 2θ (Large d-Spacing) Standard for Powder Diffraction", Certificate of the National Bureau of Standards.

[118] Ravikumar K. and Sridhar B. (**2009**). "Molecular and Crystal Structure of Efavirenz, a Potent and Specific Inhibitor of HIV-1 Reverse Transcriptase, and Its Monohydrate", Molecular Crystals

and Liquid Crystals **515** (1), pp. 190-198. doi: 10.1080/15421400903291434

[119] Melo A.C.C., Amorim I.F., Cirqueira M.L. (**2013**). "Toward Novel Solid-State Forms of the Anti-HIV Drug Efavirenz: From Low Screening Success to Cocrystals Engineering Strategies and Discovery of a New Polymorph", Cryst. Growth Des. **13**, pp. 1558–1569. doi:10.1021/cg3018002

Scientific Production

Optical Characterization of a Powder Diffraction Beamline

1. "**MCX: a synchrotron radiation beamline for X-ray diffraction Line Profile Analysis**",
   Luca Rebuffi, Jasper R. Plaisier, Mahmoud Abdellatief, Andrea Lausi, Paolo Scardi,
   Z. Anorg. Allg. Chem., 640 (2014), 3100-3106, doi: 10.1002/zaac.201400163.

Studies of nanostructured materials with large crystalline domains

2. **"Stoichiometry effect on Cu_2ZnSnS_4 thin films morphological and optical properties"**,
   Claudia Malerba, Cristy Leonor Azanza Ricardo, Matteo Valentini, Francesco Biccari, Melanie Müller, Luca Rebuffi, Emilia Esposito, Pietro Mangiapane, Paolo Scardi, Alberto Mittiga,
   J. Renew. Sustain. Energy 6 (2014), 011404, doi: 10.1063/1.4866258

3. "**Correlation between microstructure and bioequivalence in Anti-HIV Drug Efavirenz**",
   Cinira Fandaruff, Marcos Antônio Segatto Silva, Danilo Cesar Galindo Bedor, Davi Pereira de Santana, Helvécio Vinícius Antunes Rocha, Luca Rebuffi, Cristy Leonor Azanza Ricardo, Paolo Scardi, Silvia Lucia Cuffini,
   Eur. J. Pharm. Biopharm. 91 (2015), 52–5, doi: 10.1016/j.ejpb.2015.01.020

A proposed reference material for Line Profile Analysis

4. **"Toward a reference material for line profile analysis "**,
   Andrea Troian, Luca Rebuffi, Matteo Leoni, Paolo Scardi,
   Powder Diffraction (2014), *published online: dx.doi.org/10.1017/S0885715614001298*

5. **"A proposed reference material for Line Profile Analysis"**, Luca Rebuffi, Andrea Troian, Regina Ciancio, Elvio Carlino, Paolo Scardi,
submitted to Journal of Applied Crystallography

Understanding the Instrumental Profile Function: a realistic ray-tracing approach

6. **"Design and management of a powder diffraction beamline for Line Profile Analysis: a realistic ray-tracing approach"**, Luca Rebuffi, Paolo Scardi, Manuel Sánchez del Río,
accepted for publication by Powder Diffraction (2015)

7. **"Calculation of the instrumental profile function for a powder diffraction beamline used in nanocrystalline material research"**,
Luca Rebuffi, Paolo Scardi,
Proc. SPIE 9209 (2014), Advances in Computational Methods for X-Ray Optics III, 92090J, doi:10.1117/12.2063745

8. **"A proposal for an Open Source graphical environment for simulating X-ray optics"**,
Manuel Sánchez del Río, Luca Rebuffi, Janez Demšar, Niccolò Canestrari, Oleg Chubar,
Proc. SPIE 9209 (2014), Advances in Computational Methods for X-Ray Optics III, 92090X, doi:10.1117/12.2061834

Participation to Congresses, Schools and Workshops

1. **13th European Powder Diffraction Conference (EPDIC13)**

   Grenoble (France) – 28-31 October 2012

   Poster presentation**: "Evaluation of CZTS stoichiometry effects on band gap energy by Synchrotron Radiation X-ray Diffraction"**

2. **Advanced School on Synchrotron Techniques in Environmental Scientific Projects**

   Trieste (Italy) - 15-29 April 2013

3. **MEtrology, Astronomy, Diagnostics and Optics Workshop (MEADOW)**

   Trieste (Italy) - 29-30 October 2013

4. **"COherent X-ray spectroscopy: the dream" Workshop**

   Trieste (Italy) - 2-3 December 2013

5. **VISPY Code Camp**

   Grenoble (France) – 19-21 February 2014

6. **Workshop NANO**

   Trento (Italy) – 19 March 2014

   Oral presentation: **"Line Profile Analysis at SR sources: MCX @ Elettra, current state and perspectives"**

7. **14th European Powder Diffraction Conference (EPDIC14)**

   Åhrus (Denmark) – 15-18 June 2014

   Oral Presentation**: " Design and management of a powder diffraction beamline for Line Profile Analysis: a realistic ray-tracing approach"**

   Poster presentation**: "A possible new reference material for line profile analysis"**

   Poster presentation**: "On the Line Profile Analysis of**

pharmaceutical drugs"

8. **16th International Workshop on Radiation Imaging Detectors (iWoRiD)**

   Trieste (Italy) – 22-26 June 2014

9. **SPIE Optics + Photonics 2014**

   San Diego (USA) – 18-22 August 2014

   Oral Presentation: **"Calculation of the instrumental profile function for a powder diffraction beamline used in nanocrystalline material research"**

   Poster presentation**: "A proposal for an Open Source graphical environment for simulating X-ray optics"**

   Demo session: **"The new Orange-driven SHADOW gui"**

10. **TOPAS – advanced modelling of diffraction data from polycrystalline materials**

    Trento (Italy) – 28-30 October 2014

Acknowledgements

I think I am a truly lucky man. I can affirm this as I met such special people in my return to the world of research after several years spent working for private companies.

I was a risk, nothing more, nothing less, that two men were willing to take, who believed in me and continuously pushed me to become a better researcher, sharing with me not only an incredible amount of knowledge, but, mostly, a warm friendship, which is precious and dear to me. These two men are Dr. Edoardo Busetto and Professor Paolo Scardi.

Edoardo always encouraged and sustained me. Not only did he strongly support me in obtaining the necessary funding and work permission to be able to follow a doctoral school, but he also recommended me highly for the permanent position that I obtained in 2012. I will never forget this act and I choose to dedicate this PhD Thesis to our friendship and to the amazing future work we will undertake together at Elettra-Sincrotrone Trieste.

Paolo is one of the most brilliant scientists I have ever met; a fantastic teacher, an authentic point of reference. In three years I learned so much from him that I feel sincerely honoured to have been one of his students. He listened to me with patience, spending many, many hours taking care of my research work whilst always smiling reassuringly. Our friendship and scientific collaboration, which I hope will be both long and fruitful, are true gifts to me.

I warmly thank Professor Alfonso Franciosi, President and CEO of Elettra-Sincrotrone Trieste for having allowed me to enter the doctoral school and complete my studies, which were fully sustained economically and operationally.

With never-ending gratitude I want to thank the MCX staff: Dr. Andrea Lausi, Dr. Jasper Rikkert Plaisier and Dr. Mahmoud Abdellatief. I know perfectly well how outstanding and exceptional your support was to this work and I know without a doubt that it made a huge difference.
I want to sincerely thank my colleagues at Elettra-Sincrotrone Trieste for providing measurements and support with enthusiasm and great professionalism: Dr. Maurizio Polentarutti, Dr. Giorgio Bais and Dr. Nicola Demitri from XRD1 beamline, Dr. Heinz Amenitsch from SAXS beamline and Dr. Giuliana Aquilanti from EXAFS beamline. Very special thanks goes to Gianluca Bortoletto and Giulio Zerauschek, both technicians with "golden hands" and overwhelming patience.
With particular affection, I wish to honour Dr. Anna Bianco of the Optic Group, not only for providing me with many useful indications, but also for honouring me with her friendship and trust. I had the great fortune to collaborate with Dr. Regina Ciancio from TASC laboratory of CNR-IOM and she provided incredible TEM measurements, made possible due to her hard work, unwavering dedication and passion.
A sincere hug of gratitude goes to the people of the University of Trento who helped me many, many times: Dr. Cristy Leonor Azanza Ricardo, Dr. Luca Gelisio, Dr. Claudia Malerba, Dr Melanie Müller, Dr. Alberto Leonardi and, last but not least, Dr. Mirko D'Incau. Warm thanks goes to Sara di Salvo and Giovanna Carlà for their kind administrative assistance. To Marika Broseghini and Pablo Vinicius Lia Fook, a special thankyou for participating during the exhausting beamtime with such commitment.

My fortune continued to grow when I met Dr. Manuel Sánchez Del Río, a leading expert worldwide in optics and simulation tools, who spontaneously offered his help to me with an invitation to ESRF. From that first visit not only did a fantastic and promising scientific collaboration emerge, but also a warm friendship. Dearest Manolo, I am

truly unable to express how much all those dinners with your amazing, sweet family meant to me and I thank you from the depth of my heart for them. I really cannot properly express how grateful I am for your patience, your smoothness, your willingness to share your knowledge, your support and your heart-warming cheerfulness.

Another gift I received from my adventures in the optic world was to meet the amazing group of people who are developing ORANGE at the University of Ljubljana, in particular, Professor Janez Demšar, one of the kindest people I have ever met: thank you Janez for being so open-minded and for spending so many hours of your precious time customizing your tool for our needs. Warm thanks goes to Aleš Erjavec and Anže Starič for kindly and readily helping me also.

During my Thesis work, I had the unexpected fortune to be the co-tutor of the master degree Thesis work of Andrea Troian, not only a genuinely promising and talented young engineer, but a very special human being. It was a real pleasure to share in your effort and I am really grateful to have been part of your scientific growth.

To complete these acknowledgments, I want to mention people from my private life and for this I definitely need to switch to my own native language.

Non parlo facilmente dei miei sentimenti più privati e solo poche persone possono affermare di conoscermi in profondità. Ciò nonostante, per me è davvero importante lasciare qualche parola scritta a valle di questo periodo della mia vita così intenso e impegnativo.
A Federica un grazie forte e potente. So che hai attraversato e sopportato i miei travagli interiori ed esteriori in un periodo tutt'altro che facile della tua vita. So che mi hai sostenuto quanto e come meglio hai potuto, e so quanto sia stato impegnativo farlo. So quanto mi vuoi bene. So anche di

aver già detto troppo per i tuoi gusti e quindi per altre parole..."altrove e altroquando".

Cara Thea, amica, madre, sorella e medico, eri in questo paragrafo anche nella mia tesi di laurea, e ci sei nuovamente adesso. Tu sai bene perché ed io non posso che essertene ancora immensamente grato.

Agli amici più cari, Consuelo, Francesca, Luca, Barbara e i fantasmagorici Rosamarina (con annessi e connessi), un grazie di cuore per la vostra amicizia e partecipazione, nonostante il personaggio in questione.

A Lita e Roberto, meravigliosi amici e maestri, un abbraccio grande e forte per avermi sempre accolto e voluto bene esattamente come sono, con generosità e calore.

E, infine, col pensiero mi stringo ai miei "vecchi": mamma e papà, che certamente si godono questo traguardo dalle loro montagne, e mio zio Antonino, che sa regalarmi un sorriso sincero ogni volta mi vede.